

## Cohesive crack using the Symmetric Boundary Element Method

Cucco F.<sup>1</sup>, Terravecchia S.<sup>2</sup> and Zito L.<sup>3</sup>

<sup>1</sup> Via E. Tricomi 8, 90127 Palermo, Italy, filippo.cucco@tiscali.it

<sup>2</sup> Diseg Viale delle Scienze, 90128 Palermo, Italy, terravecchia@tiscali.it

<sup>3</sup> Diseg Viale delle Scienze, 90128 Palermo, Italy, zitoliborio@tiscali.it

**Keywords:** symmetric BEM, quasi brittle fracture, internal spring, substructuring.

**Abstract.** In this paper a strategy which allows to evaluate a stiffness function along the process zone has been developed. It is based on the constitutive relations  $\boldsymbol{\sigma} - \Delta \mathbf{u}$  between the normal and shearing stresses and the corresponding relative displacements. On the base of these stiffness functions, appropriately modelled on the discretized boundary of the process zone, the nodal stiffness will be evaluate for the simulation of the cohesive phenomena.

### Introduction

In this paper, the symmetric Galerkin boundary element formulation is applied to the fracture mechanics problems for quasi brittle materials. The non-linearity on the process zone of the crack will be simulate through a discrete distribution of nodal springs which generalized stiffnesses are obtainable by the tractions and the relative displacements modelling. This goal is reached coherently with the constitutive relation  $\boldsymbol{\sigma} - \Delta \mathbf{u}$  that describe the interaction between mechanical and kinematical quantities along the process zone.

The cracked body is considered as a solid having a “particular” geometry which analysis is obtainable through the displacements approach employed in [1] by some of the present authors in the ambit of the Symmetric Boundary Elements Method (SGBEM). In this approach the displacements between the crack edges nodes, evaluated on the real body, are considered distinct and the analysis is performed by evaluating all the solving system coefficients in closed form [2,4].

An example shows the goodness of the methodology proposed through a comparison with other formulations [3].

### The cohesive model using spring distributions

A strategy that describe coherently the cracked materials behaviour is that to use a couple of constitutive laws.

- a) A stress-strain relationship, which describe the elastic behaviour of the uncracked material untill the ultimate tensile stress  $\sigma_u$ .
- b) A traction-crack opening displacement relationship, that describes the softening behaviour of the cracked material, untill critical opening displacement  $\Delta u_c$  when this value exceeds the mechanical and kinematical interactions between the crack edges.

These two constitutive laws are valid for brittle materials with elasto-softening behaviour, where the energy  $G_f$  is dissipated exclusively along the crack surfaces.

For every fracture phenomena we may distinguish two different parts of the crack which relative lengths derive by the material characteristics and by the load conditions. The first part is called “real crack” and is characterized by the absence of interactions between the crack edges, due to the complete separation of the crack surface. The second part is a little zone ahead of the crack tip, called “process zone”. This part is characterized by a damage of the material and by microcracks and microvoids. The material surrounding the process zone manifests a nonlinear behaviour due by the interaction between the crack edges [5].

In the ambit of quasi-brittle materials the nonlinear phenomena may be simulate using the Barenblatt cohesive model [3]. Barenblatt introduces a limitation of the displacement discontinuities between the crack boundaries of the process zone; this interaction between the fictitious crack edges is produced by two mutual distribution of cohesive closing forces. These traction distributions along the process zone are independent by the load conditions and reach ultimate tensile stress  $\sigma_u$  at the crack tip.

Let us consider the traction-crack opening displacement relationships that describe the softening behaviour of the cracked body. These relations connect the cohesive traction to the displacement discontinuities at the process zone of the crack through the following constitutive laws:

$$\sigma = \sigma_u \left( 1 - \frac{\Delta u}{\Delta u_c} \right), \quad \tau = \tau_u \left( 1 - \frac{\Delta w}{\Delta w_c} \right) \quad (1a,b)$$

Let us introduce a shape function to model the relative displacement along the fictitious crack  $\Psi_{\Delta u}$ . The modelling of cohesive tractions  $\Psi_f$  are obtained by constitutive laws and vice versa. Therefore if the cohesive forces and the displacement discontinuities are modelled with hermitian shape functions, to better approximate the nonlinear distribution of Barenblatt forces, we set on  $\Gamma_c$ :

$$\sigma = \Psi_f \sigma_u = \left( -\frac{2x^3}{l_c^3} + \frac{3x^2}{l_c^2} \right) \sigma_u, \quad \tau = \Psi_f \tau_u = \left( -\frac{2x^3}{l_c^3} + \frac{3x^2}{l_c^2} \right) \tau_u \quad (2a,b)$$

$$\Delta u = \Psi_{\Delta u} \Delta u_c = \left( \frac{2x^3}{l_c^3} - \frac{3x^2}{l_c^2} + 1 \right) \Delta u_c, \quad \Delta w = \Psi_{\Delta w} \Delta w_c = \left( \frac{2x^3}{l_c^3} - \frac{3x^2}{l_c^2} + 1 \right) \Delta w_c \quad (2c,d)$$

where  $l_c$  is the length of the process zone.

In order to make a comparison with the Barenblatt model, a springs distribution are assume along the process zone [6], characterized by a stiffness distribution  $k(x)$ , it is:

$$\boldsymbol{\sigma} = \mathbf{k} \boldsymbol{\Delta u}, \quad \begin{vmatrix} \sigma \\ \tau \end{vmatrix} = \begin{vmatrix} k_y & 0 \\ 0 & k_x \end{vmatrix} \begin{vmatrix} \Delta u \\ \Delta w \end{vmatrix} \quad (3a,b)$$

where  $\boldsymbol{\sigma}$ ,  $\mathbf{k}$ ,  $\boldsymbol{\Delta u}$  assume the meaning of punctual quantities along the boundary  $\Gamma_c$ .

Let us use the introduced shape functions in the latter equations:

$$\Psi_f \sigma_u = k_y \Psi_{\Delta u} \Delta u_c, \quad \Psi_f \tau_u = k_x \Psi_{\Delta w} \Delta w_c \quad (4a,b)$$

by means of which it is possible to obtain the stiffness functions:

$$k_y = \frac{\sigma_u}{\Delta u_c} \frac{\Psi_f}{\Psi_{\Delta u}} = \frac{\sigma_u}{\Delta u_c} \frac{-2x^3 + 3l_c x^2}{2x^3 - 3l_c x^2 + l_c^3}, \quad k_x = \frac{\tau_u}{\Delta w_c} \frac{\Psi_f}{\Psi_{\Delta w}} = \frac{\tau_u}{\Delta w_c} \frac{-2x^3 + 3l_c x^2}{2x^3 - 3l_c x^2 + l_c^3} \quad (5a,b)$$

These functions shown a singularity of type  $1/r^3$  at the virtual crack tip where the relative displacement is null. The eqs.(5a,b) will be use to evaluate the nodal stiffnesses of the springs positioned at the nodes of the discretization to introduce subsequently.

### The equations system through coupling SGBEM-springs

The proposed model in this paper mainly regards the response in terms of nodal displacements of the process zone, discretized into boundary elements, included the displacement of the crack tip, and not the crack growth process and the definition of the stress field. For a cracked body the structural analysis is obtainable through the displacement formulation employed by some of the present authors in the ambit of SGBEM [1]. In this analysis it is possible to evaluate the absolute displacements of the crack nodes, included the displacement of the crack tip.

It is possible because the main characteristic of the program is given by the evaluation of all the system coefficients in closed form.

Let us consider a cracked body, subjected to a generic load condition, with a crack characterized by the boundary  $\Gamma_c$ . In the scheme a) of Fig.1 the solid is considered embedded in the infinite domain having the same physical and geometrical characteristics of the examining solid; in the scheme b) a discrete distribution of nodal internal springs is shown for the cohesive phenomenon simulation.

Let us consider the solid boundary  $\Gamma_c$  made up by two different frontiers; one  $\Gamma_c^s$  upper and one  $\Gamma_c^i$  lower, being  $\Gamma_c = \Gamma_c^s \cup \Gamma_c^i$ .

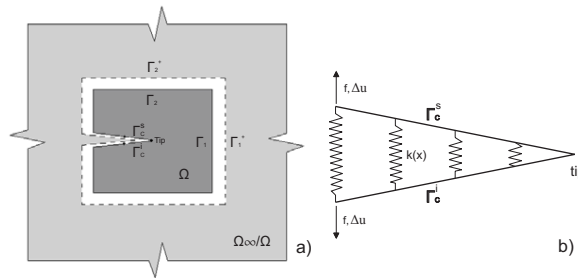


Fig. 1: a) The cracked body embedded in an infinite domain; b) The internal springs distribution.

For the scheme a) the interface relationship, called characteristic equation of the body [1], is introduced. It relates the generalized (or weighted) tractions  $\mathbf{P}_c$  defined on the elements of the boundary in the crack zone  $\Gamma_c$  to the displacements  $\mathbf{U}_c$  of the nodes of the same boundary and to the load term  $\hat{\mathbf{P}}_c$ . Moreover,  $\mathbf{D}_{cc}$  is the related stiffness matrix connected to the cracks of the examining body.

$$\mathbf{P}_c = \mathbf{D}_{cc} \mathbf{U}_c + \hat{\mathbf{P}}_c \tag{6}$$

This equation, expressed in matrix form, becomes:

$$\begin{bmatrix} \mathbf{P}_c^i \\ \mathbf{P}_c^t \\ \mathbf{P}_c^s \end{bmatrix} = \begin{bmatrix} \mathbf{D}_{cc}^{ii} & \mathbf{D}_{cc}^{it} & \mathbf{D}_{cc}^{is} \\ \mathbf{D}_{cc}^{ti} & \mathbf{D}_{cc}^{tt} & \mathbf{D}_{cc}^{ts} \\ \mathbf{D}_{cc}^{si} & \mathbf{D}_{cc}^{st} & \mathbf{D}_{cc}^{ss} \end{bmatrix} \begin{bmatrix} \mathbf{U}_c^i \\ \mathbf{U}_c^t \\ \mathbf{U}_c^s \end{bmatrix} + \begin{bmatrix} \hat{\mathbf{P}}_c^i \\ \hat{\mathbf{P}}_c^t \\ \hat{\mathbf{P}}_c^s \end{bmatrix} \tag{7}$$

where the crack tip (t) is separate from the upper (s) and lower (i) boundaries.

For the scheme b) the characteristics equation of the spring is considered

$$\mathbf{f}_c = \mathbf{k}_{cc} \Delta \mathbf{u}_c \tag{8}$$

where all these quantities have the meaning of punctual quantities along the process zone.

Let us introduce displacement discontinuities modelling

$$\Delta \mathbf{u}_c = \Psi_{\Delta u} \Delta \mathbf{U}_c \tag{9}$$

and execute the weighing of the constitutive equation (8). One obtains:

$$\int_{\Gamma_c} \tilde{\Psi}_{\Delta u} \mathbf{f}_c d\Gamma_c = \underbrace{\int_{\Gamma_c} \tilde{\Psi}_{\Delta u} \mathbf{I} \mathbf{k}_{cc} \Psi_{\Delta u} d\Gamma_c}_{\mathbf{K}_{cc}} \Delta \mathbf{U}_c \tag{10}$$

where the vector  $\mathbf{k}_{cc}$  contains the stiffness functions  $k(x)$  in both the directions  $x$  and  $y$ ,  $\mathbf{I}$  is the identity matrix, while  $\mathbf{K}_{cc}$  is a nodal stiffness diagonal matrix of the discretized springs system. The eq.(10) written in compact form takes on the following form:

$$\mathbf{P}_c = \mathbf{K}_{cc} \Delta \mathbf{U}_c. \quad (11)$$

The eqs.(6) and (11) represent the generalized interface tractions on the nodes of  $\Gamma_c$ , for both schemes a) and b), functions of the kinematical quantities only along the same boundary.

### Regularity conditions

Let us impose the regularity conditions of the nodal displacements and of the generalized tractions between the two schemes to obtain the equations system of the cohesive problem.

We must impose that:

- the nodal relative displacements of the two schemes a) and b) are equal, and besides the relative displacement of the crack tip is zero:

$$\underbrace{\mathbf{U}_c^s - \mathbf{U}_c^i}_{\text{scheme a)}} = \underbrace{\Delta \mathbf{U}_c}_{\text{scheme b)}} , \quad \underbrace{\Delta \mathbf{U}_c^t}_{\text{scheme a),b)}} = \mathbf{0}. \quad (12a,b)$$

- the generalized tractions must satisfy the equilibrium equation:

$$\underbrace{-\mathbf{P}_c^s = \mathbf{P}_c^i}_{\text{scheme a)}} = \underbrace{\mathbf{P}_c}_{\text{scheme b)}} \quad (13)$$

Let us denote that in the scheme b), the crack tip is made by a single node, consequently no spring is present, therefore  $\Delta \mathbf{U}_c^t = \mathbf{0}$ .

Therefore the equations system is the following::

$$\underbrace{\mathbf{P}_c = \mathbf{D}_{cc} \mathbf{U}_c + \hat{\mathbf{P}}_c}_{\text{scheme a)}} , \quad \underbrace{\mathbf{P}_c = \mathbf{K}_{cc} \Delta \mathbf{U}_c}_{\text{scheme b)}} \quad \text{constitutive equations} \quad (14a,b)$$

$$\underbrace{\mathbf{U}_c^s - \mathbf{U}_c^i}_{\text{scheme a)}} = \underbrace{\Delta \mathbf{U}_c}_{\text{scheme b)}} , \quad \underbrace{\Delta \mathbf{U}_c^t}_{\text{scheme b)}} = \mathbf{0} \quad \text{compatibility equations} \quad (14c,d)$$

$$\underbrace{-\mathbf{P}_c^s = \mathbf{P}_c^i}_{\text{scheme a)}} = \underbrace{\mathbf{P}_c}_{\text{scheme b)}} \quad \text{equilibrium equations} \quad (14e)$$

In order to evaluate the absolute displacements of both the upper and lower boundaries, the eqs.(14c,d) are put in the eq.(14b), so obtaining the next matrix expression:

$$\begin{bmatrix} \mathbf{P}_c \\ \mathbf{0} \\ \mathbf{P}_c \end{bmatrix} = \begin{bmatrix} -\mathbf{K}_{cc}^{ii} & \mathbf{0} & \mathbf{K}_{cc}^{is} \\ \mathbf{0} & \mathbf{0} & \mathbf{0} \\ -\mathbf{K}_{cc}^{si} & \mathbf{0} & \mathbf{K}_{cc}^{ss} \end{bmatrix} \begin{bmatrix} \mathbf{U}_c^i \\ \mathbf{0} \\ \mathbf{U}_c^s \end{bmatrix}. \quad (15)$$

In the discretized system the use of the constitutive equation (15) of the springs and of the analogous eq.(14a) of the cracked body, as well as the use of the equilibrium equation (14e) permit to obtain the coupled SGBEM-springs equations system:

$$\begin{bmatrix} \mathbf{D}_{cc}^{ii} + \mathbf{K}_{cc}^{ii} & \mathbf{D}_{cc}^{it} & \mathbf{D}_{cc}^{is} - \mathbf{K}_{cc}^{is} \\ \mathbf{D}_{cc}^{ti} & \mathbf{D}_{cc}^{tt} & \mathbf{D}_{cc}^{ts} \\ \mathbf{D}_{cc}^{si} - \mathbf{K}_{cc}^{si} & \mathbf{D}_{cc}^{st} & \mathbf{D}_{cc}^{ss} + \mathbf{K}_{cc}^{ss} \end{bmatrix} \begin{bmatrix} \mathbf{U}_c^i \\ \mathbf{U}_c^t \\ \mathbf{U}_c^s \end{bmatrix} + \begin{bmatrix} \hat{\mathbf{P}}_c^i \\ \hat{\mathbf{P}}_c^t \\ \hat{\mathbf{P}}_c^s \end{bmatrix} = \mathbf{0}, \quad (\mathbf{D}_{cc} + \mathbf{K}_{cc}^*) \mathbf{U}_c + \hat{\mathbf{P}}_c = \mathbf{0}. \quad (16a,b)$$

In this way it is possible to obtain the vector of the nodal absolute displacements  $\mathbf{U}_c$  at the nodes of the fracture boundaries and, as a consequence, also the distribution of the tractions

along the process zone. This last vector permits to evaluate all the boundary nodal quantities of the body, as shown in [1]

**A cohesive model developed using substructuring**

In this section an alternative strategy will be shown, which permits to consider the gradual development of the crack using a substructuring of the wedge at the crack  $\Gamma_c$  having a different Young modulus for each substructure which characteristic equation is given by (6).

This strategy is performed by using the karnak.sGbem program made by some of the authors of this paper. This approach is lead using symmetrical formulation through a substructuring approach which permits to simulate the strenght decay along the process zone. It is made possible since all the system coefficients were computed in closed form [2,4], and therefore no numerical instabilities may arise for the very different dimentionns between the solid and the substructures of the process zone.

Let us consider the generic process zone  $\Gamma_c$  of Fig.2, discretized by 8 boundary elements. Four substructures are introduced.

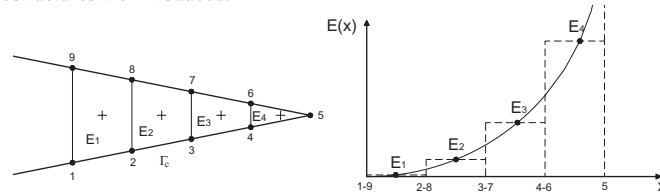


Figure 2: Cohesive phenomena simulation using substructures with different Young modulus.

The values  $E_n$  (with  $n=1,2,3,4$ ) may be evaluate by using the function  $E(x)$  as shown in Fig.2. This function is easily obtainable by eq.(5a), that is:

$$E(x) = \frac{l(x) k_y(x)}{A} \tag{17}$$

where  $l(x)$  is the function that describes the punctual gap between the crack edges,  $A$  is the base area of the each substructure, which may be consider equal for every of them in the hypothesis of costant thickness and of equal width of the substructure. If this function  $E(x)$  is used, four punctual stiffness values  $E_n$  (with  $n=1,2,3,4$ ) are evaluated at the barycentre of the every substructure..

**Example**

Let us consider the solid of Fig.3a, having the following dimensions 200x100x1 cm., in presence of a rectilinear crack. The solid is loaded by a double vertical distribution of traction  $q=1000\text{daN/m}$  that produce in the solid a deformation of Mode I. The following physical characteristics are assumed:  $E=100000 \text{ daN/cm}^2$ ,  $\nu=0.2$ . The solid is discretized by 30 boundary elements, included also the elements between the nodes 18 and 26 which define the process zone  $\Gamma_c$ . Besides the quantities  $\sigma_y = 30 \text{ daN/cm}^2$ ,  $\Delta u_c = 0.003 \text{ cm}$  are assumed to define the stiffness function  $K_y \neq 0$ , only, in order to limit the normal relative displacements.

This example has the only aim to show that, because of the presence of the springs distribution on  $\Gamma_c$ , the relative displacements of the two crack edges tends quickly to zero.

In Fig.(3d,e) are show the diagrams of the absolute nodal displacements  $U_x$  and  $U_y$  along the process zone  $\Gamma_c$ . In its the following proposed models have been used: the model by springs nodal distribution (Fig.3b) and the model by substructures having different Young modulus (Fig.3c). These comparisons show that the two strategies conduct to a solution having nearly equal horizontal and vertical absolute displacements.

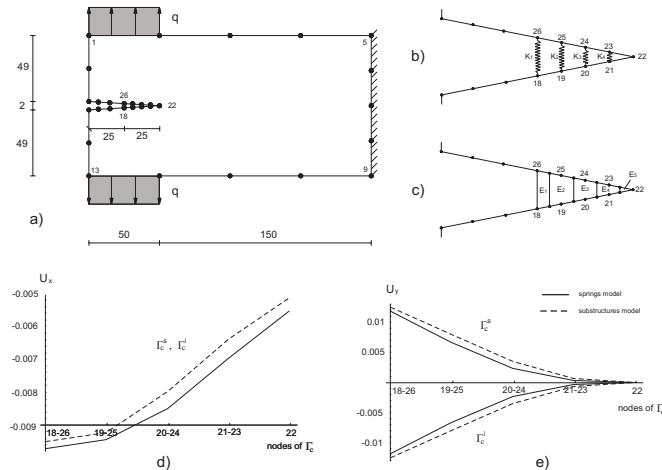


Figure 3: a) Boundary discretization; b,c) Simulation of the cohesive phenomena using spring distribution and substructures; d,e) absolute displacements in x and y direction.

### Conclusions

In this paper two strategies to simulate the non-linear behaviour at the crack process zone have been developed, and in detail:

- A distribution of internal nodal springs having different stiffness is introduced at the aim to reduce the relative displacements coherently with the constitutive relation  $\sigma - \Delta u$  that describes the interaction between mechanical and kinematical quantities in the process zone.
- A discrete number of substructures are introduced having different Young modulus at the aim to simulate the softening behaviour along the fictitious crack.

These two strategies have been activated using the potentiality of the software Karnak.sGbem.

### References

- [1] Panzeca T, Cucco F, Terravecchia S. Symmetric Boundary Element Method versus Finite Element Method. *Comp. Meth. Appl. Mech. Engng.*, **191**, 3347-3367 (2002).
- [2] Panzeca T, Fujita Yashima H and Salerno M, Direct stiffness matrices of BEs in the Galerkin BEM formulation. *Eur. J. Of Mech., A/Solids*, **20**, 277-298, (2001).
- [3] Barenblatt GI. Mathematical theory of equilibrium cracks in brittle fracture. *Adv. In Appl. Mech.*, **7**, 55-129 (1962).
- [4] Terravecchia S. Closed form in the Symmetric Boundary Element Approach. *Eng. Anal. Bound. Elem. Meth.*, **30**, 479-488 (2006).
- [5] Sladek J, Sladek V, Bazant PZ. Non-local boundary integral formulation for softening damage. *Int. J. Num. Meth. in Engng.*, **57**, 103-116 (2003).
- [6] Yang B, Ravi-Chandar K. A single-domain dual-boundary-element formulation incorporating a cohesive zone model for elastostatic cracks. *Int. J. Fract.*, **93**, 115-144 (1998).
- [7] Carini A, Diligenti M, Maranesi P, Zannella M. Analytical integrations for two-dimensional elastic analysis by the symmetric Galerkin boundary element methods. *Comp. Mech.*, **23**, 308-323 (1999).

## Convection-dominant transport simulations with the flux Green element method

Akpofure E. Taigbenu

*School of Civil and Environmental Engineering, University of the Witwatersrand.*

*P. Bag 3, Johannesburg, WITS 2050, South Africa.*

*Email: [akpofure.taigbenu@wits.ac.za](mailto:akpofure.taigbenu@wits.ac.za)*

**Keywords:** Green element method; boundary element method; convection-diffusion; contaminant transport.

### Abstract

Transport of mass, momentum, vorticity or energy, in which mechanisms of diffusion or dispersion and convection play an important role, can be described by the diffusion-convection equation. Depending on the relative importance of these two mechanisms (diffusion and convection), the governing equation behaves somewhat between a parabolic and hyperbolic equation. The latter is usually more challenging to solve. Using the logarithmic fundamental solution of the Laplacian operation and implementing the integral equations obtained from applying Green's identity in an element-by-element fashion, the concentrations and their normal directional derivatives are calculated at every node. This formulation is referred to as the flux Green element method (GEM). Because of direct calculations of the concentrations and their normal directional derivatives, high accuracy is achieved with the current formulation using coarse grids. The compatibility condition for the normal derivatives of the concentration at internal nodes is prescribed in a novel manner. Four different treatments are accorded the convective term which give different levels of accuracy. Two numerical examples are used to demonstrate the accuracy of the current formulation for convection-dominant transport problems.

### 1. Introduction

There are many transport phenomena in the fields of engineering and science that are described by the diffusion-convection equation. It is for this reason that its solution continues to receive considerable interest. It is particularly intriguing when the convective term is dominant, in which case the equation behaves like a hyperbolic equation rather than a parabolic one when diffusion is dominant. The relative importance of these two mechanisms is captured by the Peclet number, with high values denoting convective dominance. For such convective-dominant transport, numerical schemes tend to be plagued by spurious oscillations.

Along the lines of singular integral formulations, there are a variety of techniques which have been employed to solve the diffusion-convection equation. The conventional approach which attempts to achieve a strictly boundary integral formulation is plagued with the challenge of dealing with a domain integral and assuming uniform distribution of velocity and diffusion coefficient [1-3]. To eliminate the domain integrations, the dual reciprocity method (DRM) has been used. Earlier formulations were limited to small values of Peclet number and for weakly nonlinear transport. A DRM formulation, which follows the Green element philosophy, has been presented in [4, 5] and it addresses convection dominant problems. However, only steady transport examples were solved. Their work also retained the normal directional derivative of the concentration at all nodes and resolved the closure problem at internal nodes by a least square approach.

The method proposed in this paper for the diffusion-advection equation uses the fundamental solution of the Laplacian operator and Green's identity to obtain the integral equations which are implemented in an element-by-element sense so that nonlinearities and heterogeneity are readily accommodated [6-8]. The domain integrations are easy to implement in that they are exact and depend only on the geometrical features of the elements. The normal directional derivatives of the concentration is retained everywhere, including internal nodes, and the closure problem is resolved innovatively by introducing an additional compatibility equation. Because both the concentration field and its normal directional derivative are interpolated by the same order of interpolation functions, high accuracy is achieved at the expense of large number of unknowns. However this high level of accuracy is achieved with coarse discretization. Two examples of contaminant transport problems are solved with the current formulation and its demonstrated how, with few elements, high accuracy is achieved.

## 2. Transport Equation and the Flux GEM

The differential equation that describes the transport of species in a given fluid medium is given by

$$\nabla \cdot (D\nabla c) = \frac{\partial c}{\partial t} + \nabla c \cdot \mathbf{V} \quad (1)$$

where  $\nabla$  is the gradient operator and  $c$  is the concentration, and the hydrodynamic dispersion coefficient  $D$  can have spatial variation (heterogeneous medium),  $\mathbf{V} = \mathbf{i}u + \mathbf{j}v$  is the velocity vector of the transporting fluid medium. Although we restrict the discussion in this paper to the case when the hydrodynamic dispersion coefficient is uniform throughout the medium, it has been demonstrated in previous works that GEM is well suited for heterogeneous media and nonlinear equations [6,8]. A unique solution to the mathematical statement expressed as eq (1) is achieved when appropriate conditions for  $c$  and/or its normal flux  $q = -D\nabla c \cdot \mathbf{n}$  are specified on the boundary  $\Gamma$ . The Dirichlet-type condition specifies the concentration on a part of the boundary  $\Gamma_1$

$$c(x, y, t) = c_1(t) \text{ on } \Gamma_1 \quad (3a)$$

while the Neumann condition specifies the flux across another part of the boundary  $\Gamma_2$

$$-D\nabla c \cdot \mathbf{n} = q_2(t) \text{ on } \Gamma_2 \quad (3b)$$

where  $\mathbf{n}$  is the unit outward pointing normal vector on the boundary. The Cauchy-type condition prescribes a linear combination of the concentration and the normal flux on another part of the boundary  $\Gamma_3$ ,

$$\mu_1 c + \mu_2 D\nabla c \cdot \mathbf{n} = c_3(t) \text{ on } \Gamma_3 \quad (3c)$$

where  $\mu_1$  and  $\mu_2$  are known constants and the region  $\Omega$ , in which eq (1) applies, has boundary  $\Gamma = \Gamma_1 \cup \Gamma_2 \cup \Gamma_3$ . Being a time dependent problem, the initial condition is specified at the initial time  $t_0$

$$c(x, y, t = t_0) = c_0(x, y) \text{ on } \Omega \quad (3d)$$

Taking advantage of the simplicity of the logarithm fundamental solution to auxiliary differential equation  $\nabla^2 G = \delta(r - r_i)$  in the infinite space, Green's theorem is applied to the differential eq (1) to obtain its integral representation

$$D \left[ -\lambda c_i + \int_{\Gamma} (c\nabla G \cdot \mathbf{n} - G\nabla c \cdot \mathbf{n}) ds \right] - \iint_{\Omega} G \left[ \nabla c \cdot \mathbf{V} + \frac{\partial c}{\partial t} \right] dA = 0 \quad (4)$$

in which the subscript  $i$  represents the source point  $r_i = (x_i, y_i)$  and  $\lambda$  is the nodal angle at the source point that is obtained from a Cauchy integration of the Dirac delta function. Eq (4) is re-expressed as

$$D \left[ -\lambda c_i + \int_{\Gamma} c\nabla G \cdot \mathbf{n} ds \right] + \int_{\Gamma} G q ds - \iint_{\Omega} G \left[ \frac{\partial(uc)}{\partial x} + \frac{\partial(vc)}{\partial y} + \frac{\partial c}{\partial t} \right] dA = 0 \quad (5)$$

Eq (5) applies equally to the entire solution domain and a subdomain or element that is used to discretise the domain. It is for now considered for an element  $\Omega^e$  with boundary  $\Gamma^e$  over which the distribution of quantities such as  $c$  and  $q$  are approximated by appropriate Lagrange-type interpolation functions. Implementing the integrations over each element gives a set of discrete equations.

$$DR_j c_j + L_j q_j - W_j \frac{dc_j}{dt} - \iint_{\Omega^e} G \left[ \frac{\partial(uc)}{\partial x} + \frac{\partial(vc)}{\partial y} \right] dA = 0 \quad (6)$$

where the indices represent the number of nodes in the element, and

$$R_j = \int_{\Gamma^e} N_j \nabla G(r, r_i) \cdot \mathbf{n} ds - \delta_{ij} \lambda, \quad L_j = \int_{\Gamma^e} N_j G(r, r_i) ds, \quad W_j = \iint_{\Omega^e} G(r, r_i) N_j dA \quad (7)$$

where  $N_j$  is the Lagrange interpolation function with respect to node  $j$ . The domain integration of the convective term has been intentionally retained because it can be implemented in four different ways. The temporal derivative is approximated by finite differencing  $dc/dt \approx (c^{(2)} - c^{(1)})/\Delta t$ , where the superscripts denote the current time  $t_2$  and previous time  $t_1$ . To reflect the time within the time step  $\Delta t$  that the differencing is done, quantities in eq (6) at the current time are weighted by a factor  $\alpha$  which is allowed to take a value between zero and unity, and those at the previous time by  $1 - \alpha$ . The global matrix equation is obtained by aggregating the elemental discrete equations so that at each node the concentration and its normal directional derivative with respect to the sides of the elements are obtained.

**3. Numerical Approximation of the Convective Term**

**3.1 Approach 1**

In this approach, the quantity  $uc$  is taken collectively, and similarly for  $vc$ . They are then interpolated by the Lagrange interpolations functions as follows:

$$\frac{\partial(uc)}{\partial x} \approx \frac{\partial N_j}{\partial x} (uc)_j \text{ and } \frac{\partial(vc)}{\partial y} \approx \frac{\partial N_j}{\partial y} (vc)_j \tag{8}$$

and the discrete equation now becomes

$$DR_{ij}c_j + L_{ij}q_j - W_{ij} \frac{dc_j}{dt} - X_{ij}(uc)_j - Y_{ij}(vc)_j = 0 \tag{9}$$

in which

$$X_{ij} = \iint_{\Omega^e} G(r, r_i) \frac{\partial N_j}{\partial x} dA; \quad Y_{ij} = \iint_{\Omega^e} G(r, r_i) \frac{\partial N_j}{\partial y} dA \tag{10}$$

This is the simplest and least accurate way of treating the convective term, and it is the cheapest to numerically implement.

**3.2 Approach 2**

In this approach,  $\partial(uc)/\partial x$  and  $\partial(vc)/\partial y$  are expanded and then the quantities  $c$ ,  $u$  and  $v$  are individually approximated by the interpolation functions so the discrete equation becomes

$$DR_{ij}c_j + L_{ij}q_j - W_{ij} \frac{dc_j}{dt} - X_{ijk}(u_j c_k + u_k c_j) - Y_{ijk}(v_j c_k + v_k c_j) = 0 \tag{11}$$

where

$$X_{ijk} = \iint_{\Omega^e} G(r, r_i) N_j \frac{\partial N_k}{\partial x} dA; \quad Y_{ijk} = \iint_{\Omega^e} G(r, r_i) N_j \frac{\partial N_k}{\partial y} dA \tag{12}$$

**3.3 Approach 3**

This approach takes advantage of the fact that the current Green element formulation solves for the normal directional fluxes at all nodes. It approximates the convective terms as

$$\frac{\partial(uc)}{\partial x} \approx N_j u_j N_k \frac{\partial c_k}{\partial x} + N_j c_j N_k \frac{\partial u_k}{\partial x} \text{ and } \frac{\partial(vc)}{\partial y} \approx N_j v_j N_k \frac{\partial c_k}{\partial y} + N_j c_j N_k \frac{\partial v_k}{\partial y}$$

With these approximations, the discrete equation (6) becomes

$$DR_{ij}c_j + L_{ij}q_j - W_{ij} \frac{dc_j}{dt} - T_{ijk} \left( u_j \frac{\partial c_k}{\partial x} + c_j \frac{\partial u_k}{\partial x} \right) - T_{ijk} \left( v_j \frac{\partial c_k}{\partial y} + c_j \frac{\partial v_k}{\partial y} \right) = 0 \tag{13}$$

where

$$T_{ijk} = \iint_{\Omega^e} G(r, r_i) N_j N_k dA \tag{14}$$

The derivatives of the concentration in the  $x$  and  $y$  directions can be related to the normal directional flux of the concentration  $q$

$$q = q_x n_x + q_y n_y = D \left( \frac{\partial c}{\partial x} n_x + \frac{\partial c}{\partial y} n_y \right) \tag{15}$$

where  $n_x = \mathbf{n} \cdot \mathbf{i}$  and  $n_y = \mathbf{n} \cdot \mathbf{j}$  are the direction cosines of the normal vector in the  $x$  and  $y$ , and  $\mathbf{i}$  and  $\mathbf{j}$  are the unit vectors in those two directions. Although this approach enhances the accuracy of the calculations of the convective term, it can only be implemented on elements with nodes on the vertices. On other types of elements with nodes on the sides, like the 8-node quadratic rectangle, the formulation fails because at the nodes on the side, the tangential flux is not calculated to correctly represent  $q_x$  and  $q_y$ .

**3.4 Approach 4**

This fourth approach of numerically implementing the connective term is a variation of the third approach and, for the same reason as in Approach 3, can only be applied to elements with nodes on the vertices. By expanding  $\partial(uc)/\partial x$  and  $\partial(vc)/\partial y$  as

$$\frac{\partial(uc)}{\partial x} = u \frac{\partial c}{\partial x} + c \frac{\partial u}{\partial x} \quad \text{and} \quad \frac{\partial(vc)}{\partial y} = v \frac{\partial c}{\partial y} + c \frac{\partial v}{\partial y} \quad (16)$$

Each term is now approximated by interpolating functions in the following manner:

$$\frac{\partial(uc)}{\partial x} \approx N_j \left( u \frac{\partial c}{\partial x} \right)_j + N_j \left( c \frac{\partial u}{\partial x} \right)_j \quad (17)$$

And similarly for  $\partial(vc)/\partial y$ . The discrete element equation (6) now becomes

$$DR_{ij}c_j + L_{ij}q_j - W_{ij} \frac{dc_j}{dt} - W_{ij} \left[ \left( u \frac{\partial c}{\partial x} \right)_j + \left( c \frac{\partial u}{\partial x} \right)_j \right] - W_{ij} \left[ \left( v \frac{\partial c}{\partial y} \right)_j + \left( c \frac{\partial v}{\partial y} \right)_j \right] = 0 \quad (18)$$

Before discussing the performance of some of these approaches with 2 numerical examples, it is worth mentioning that the closure problem of the normal directional derivatives of the concentration (normal fluxes) at internal nodes is resolved innovatively by the introduction of an additional equation which is essentially a mathematical statement of their compatibility relations [7,8]. As indicated in those papers, though there is an escalation of the number of degrees of freedom (unknowns) because of the direct calculation of the normal directional fluxes at all nodes, this demerit is made up for by the achievement of high accuracy with a coarse grid. Furthermore, the solution at each time level after solving the global matrix equation is complete for each of the elements. Any additional solution information at a point other than the grid points is obtained using only the calculated solutions in the element

#### 4. Numerical Examples

Two numerical examples of the transport equation are solved by the current formulation. The first example is steady and the second is transient.

##### 4.1 Example 1

This is a 1-D steady transport example with variable velocity which has been used widely as a benchmark case for assessing the performance of numerical schemes. It is governed by:

$$D \frac{d^2 c}{dx^2} - \frac{d(uc)}{dx} = 0 \quad (19)$$

With boundary conditions:  $c(x=0) = C_0$  and  $c(x=1) = C_1$ . The velocity field is

$$u = \ln \frac{C_1}{C_0} + k \left( x - \frac{1}{2} \right) \quad (20)$$

The velocity in the  $y$  direction is zero. Taking the hydrodynamic dispersion coefficient to be unity, the analytical solution is

$$c = C_0 \exp \left[ \frac{kx^2}{2} + \left( \ln \frac{C_1}{C_0} - \frac{k}{2} \right) x \right] \quad (21)$$

The example is simulated with the current 2-D. GEM formulation using Approach 2 to approximate the convective term with the upper and lower boundaries in the  $y$  direction at 0.1 and -0.1. Using 10 quadratic rectangular elements, the GEM and exact solutions for the concentration and its directional derivative in the  $x$  direction are presented in Figs. 1a and 1b for  $k$  values of 10, 20 and 40. To assess the performance of the current formulation with respect to its accuracy for different levels of discretization, simulations are carried out with discretizations of 5, 10 and 20 quadratic rectangular elements. The discretization with 5 quadratic elements is nonuniform in order that the high gradient in the concentration profile in the vicinity of  $x=0$  is captured with this coarse grid. The spacings for this discretization are 0.1, 0.15, 0.25, 0.25 and 0.25. Only the results for  $k=40$  are presented. This case represents transport with convective dominance. The relative errors in percentage are presented in Figs. 2a and 2b for the concentration and the flux in the  $x$  direction. The results show that high accuracy is achieved with no more than 10 quadratic rectangular elements. The level of accuracy achieved is much higher than those presented in [4,5] which used more number of elements.

The numerical implementation of the convective term is assessed by the first and second approaches earlier presented. Using the convective dominant case ( $k=40$ ), simulations with approaches 1 and 2 are implemented. The domain is discretized uniformly with 10 quadratic rectangular elements. The results from

the simulations are presented in Figs. 3a and 3b for the concentration and the flux in the  $x$  direction. As expected, the Approach 2 gives better approximation of the convective term, hence more accurate solutions.

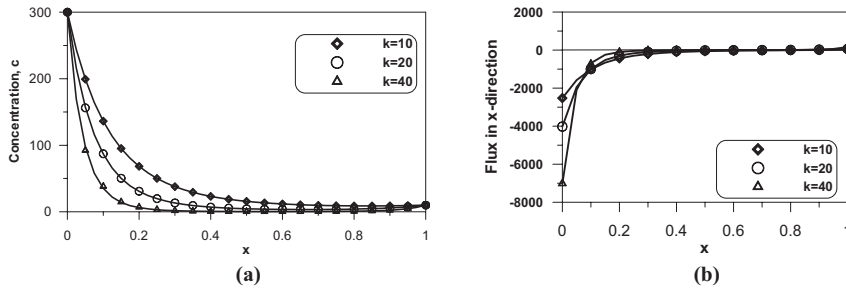


Figure 1: Flux GEM (symbols) and exact (solid line) solutions of example 1 for (a) concentration and (b) flux in the  $x$  direction.

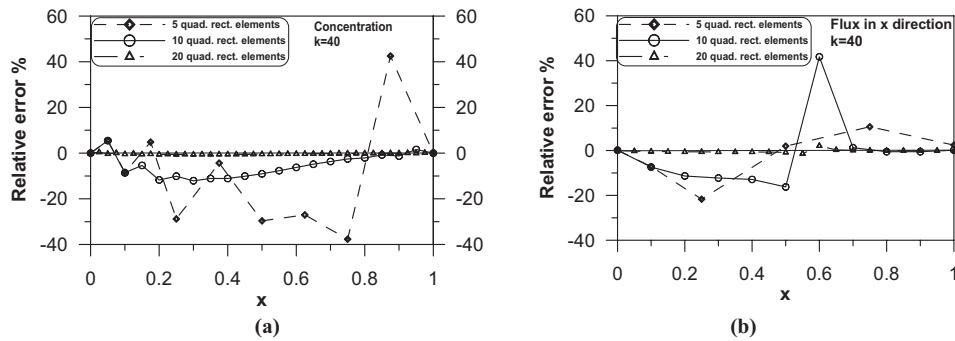


Figure 2: Error plots (a) concentration and (b) flux for example 1 with different GEM discretizations.

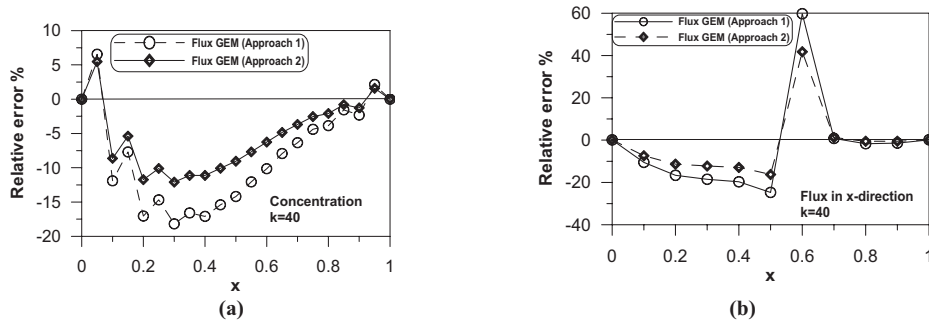


Figure 3: Error plots of example 1 from 2 approaches of approximating the convective term in GEM.

4.2 Example 2

This example is that of a 1-D. transient contaminant transport problem. The concentration profile initially is of unit value and uniform over the domain. The velocity of the flow field is uniform in the  $x$  direction and the hydrodynamic dispersion coefficient of the medium is unity. The boundary conditions are:

$$c(0, y, t) = 0 \text{ and } c(1, y, t) = 0 \tag{22}$$

The exact solution to this problem is known and can be found in [9]. Earlier simulation of this example with the Green element formulation that approximated the internal fluxes with a difference expression in terms of the concentration used 20 linear rectangular elements to discretize the domain [10]. For uniform advection velocity  $u = 5$  and  $u = 20$ , the 2-D simulation of this example with the current formulation with 5 quadratic rectangular are presented in Figs. 4a and 4d. The 5 quadratic elements used are not uniform in size; they are

smaller in the vicinity of  $x=1$  in order to capture the steep gradients of the concentration profile. From  $x=0$ , the sizes of the elements in the  $x$  direction are: 0.25, 0.25, 0.25, 0.15 and 0.1. The numerical simulations use a uniform time step of  $2.5 \times 10^{-3}$  and a weighting factor  $\alpha = 0.75$ . There is good agreement between the analytical and numerical solution with this coarse discretization. Although not presented, a comparison between the first and second approaches was carried out and it was found that the results from both approaches are virtually the same.

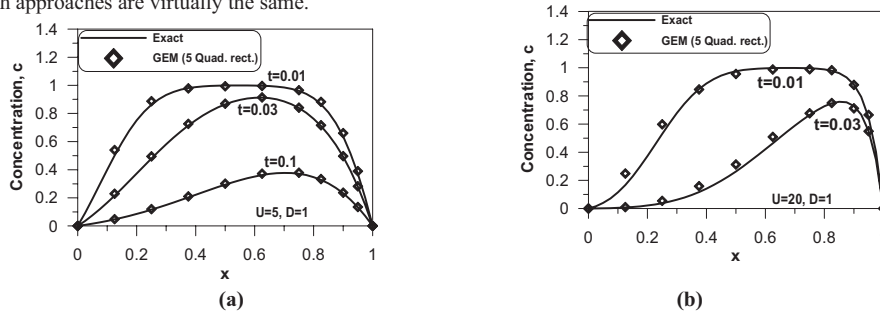


Figure 4: GEM and exact solution for (a)  $u=5$ ;  $D=1$  and (b)  $u=20$ ;  $D=1$  of example 2

## 5. Conclusion

This paper has presented Green element solutions of the transient 2-D. diffusion- convection equation which governs contaminant transport in a flow medium with variable velocity. The current formulation interpolates for the concentration and its normal directional derivative at every grid point (node). Whereas large number of degrees of unknowns is generated, it is compensated by the high accuracy that is achieved with very coarse discretization, thereby making it more attractive than the previous GEM which approximates normal directional derivatives with their difference approximations. The novelty in resolving the closure problem at internal nodes involves the introduction of a compatibility equation for all normal fluxes at an internal node. The compatibility equation is universal because it is not restricted to the current problem. The accuracy limitation of the flux GEM is dictated by how well the interpolation function approximates the primary variable and its normal directional derivatives. When these are correctly described by the interpolation function, the flux GEM produces extremely accurate solutions. Four different approximations of the convective term are presented, and with the first two implemented on two numerical examples. Although the second approach is more accurate than the first, the simplicity of numerically implementing the first makes it quite attractive.

## 6. References

- [1] M. Ikeuchi and K. Onishi, Boundary element solutions to steady convective diffusion equations. *Applied Mathematical Modelling*, **7**, 115-118 (1983).
- [2] A.E. Taigbenu and J.A. Liggett, An Integral Solution for the Diffusion-Advection Equation. *Water Resources Res.*, **22** 1237-1246 (1986).
- [3] N. Zabarar and S. Mukherjee, An analysis of solidification problems by the boundary element method. *Int. J. Numer. Math. Engng.* **24**, 1879-1900 (1987).
- [4] V. Popov and H. Power, The DRM-MD integral equation method: An efficient approach for the numerical solution of domain dominant problems. *Int. J. Numer. Math. Engng.* **44**, 327-353 (1999).
- [5] B. Natalini and R. Popov, An alternative approach for calculation of the first and higher order derivatives in the DRM-MD, *Eng. Anal. Boundary Elements*, **28**, 61-78 (2004).
- [6] A.E. Taigbenu, *The Green Element Method*, Kluwer Academic Press, Boston, USA, (1999).
- [7] A.E. Taigbenu and A. Elvin, The Green element method applied to plate bending, *Proc. of Boundary Element Techniques VII*, Paris, France, 203-209 (2006).
- [8] A.E. Taigbenu, Simulation of coupled nonlinear electromagnetic heating with the Green element method, *Proc. of Int. Conf. on Heat Transfer*, New Forest, UK, 77-86 (2006).
- [9] M.M. Aral, and Y.A. Tang, Boundary-only procedure for transient transport problems with or without first-order chemical reaction, *Applied Mathematical Modelling*, **13**, 130-137 (1989).
- [10] A.E. Taigbenu, Features of a time-dependent Fundamental solution in the Green Element Method, *Applied Mathematical Modelling*, **27**, 125-143 (2003).

# On $\mathcal{O}(n)$ algebraic preconditioners for the Fast Multipole Method

Bruno Carpentieri

Institute for Mathematics and Scientific Computing, Karl-Franzens University  
Heinrichstraße, 36 - A-8010 Graz, Austria.  
Email : `bruno.carpentieri@uni-graz.at`

## Abstract

In this paper we present the framework of preconditioners based on sparsification strategies for solving electromagnetic scattering problems expressed in an integral formulation. We review some recent results with incomplete factorization and sparse approximate inverse methods combined with the fast multipole method for large-scale surface integral equations. When computed from the near-part of the coefficient matrix, both classes of methods can maintain the algorithmic complexity of the fast multipole method.

**Keywords** : boundary integral equations, fast multipole method, Krylov subspace solvers, preconditioning.

## 1 Introduction

Nowadays integral equation methods are extensively employed for solving realistic engineering and industrial applications (see e.g. [1–3]); a lot of recent work is trying to extend their use to other classes of partial differential equations. In this paper we consider an application of integral equation methods to the solution of electromagnetic scattering problems. The Galerkin method can be used to discretize integral equations and generate a dense complex-valued linear system of equations. For solving the pertinent linear system, iterative solution strategies based on preconditioned Krylov methods may be computationally attractive because they require only matrix-vector products. In the last twenty years, fertile research efforts have led to the development of fast *hierarchical* methods for performing approximate matrix-vector products with matrices arising from the discretization of integral operators (see e.g. [4–6]) in  $\mathcal{O}(n \log n)$  arithmetic operations, where  $n$  denotes the problem size. It is known that the convergence of Krylov methods may largely depend on the eigenvalue distribution of the coefficient matrix; a fairly well clustered spectrum around point one in the complex plane leaving only few isolated eigenvalues can ensure rapid convergence of Krylov methods. For some integral formulations like the

popular Electric Field Integral Equation (EFIE), the eigenvalue distribution is far from being optimal, showing many isolated eigenvalues that are very close to zero or have large negative real part. The condition number of EFIE can grow like  $p^{1/2}$ , where  $p$  denotes the size of the scatterer in terms of wavelength, and linearly with the number of points per wavelength. As a result, on EFIE Krylov methods scale as  $\mathcal{O}(n^{0.5})$  so that preconditioning is crucial to speed up the convergence. For closed targets, the Combined Field Integral Equation (CFIE) is mandatory to use because it solves the problem of nonuniqueness of the solution. CFIE gives rise to well conditioned systems, and the number of iterations scales as  $\mathcal{O}(n^{0.25})$ . In this case Jacobi or block Jacobi preconditioners are generally effective; more sophisticated preconditioners can further reduce the number of iterations but increase the overall solution cost. In this paper we consider preconditioning methods especially suited for solving the EFIE formulation, although the described techniques are applicable to CFIE as well.

## 2 Preconditioning based on sparsification strategies

In order to maintain the algorithmic complexity of the fast multipole method in the iterative solution, we consider preconditioners based on sparsification strategies, *i.e.* the preconditioner  $M$  is computed from a sparse approximation of the dense coefficient matrix  $A$ . Given a splitting

$$A = B + S,$$

where  $B$  is a dense matrix and  $S$  is a sparse matrix, we construct  $M$  from  $S$ . The choice of  $S$  is obviously crucial for performance. One can use either information relative to the magnitude of the entries of  $A$  or information extracted from the underlying physical mesh. Because we work in an integral equation context, two types of information are available from the mesh, *i.e.* the connectivity graph describing the topological neighbourhood among the edges, and the coordinates of the nodes in the mesh describing geometric neighbourhoods among the edges. In [7], Carpentieri et al. propose three different strategies to compute  $S$ :

1. *algebraic*:  $S$  is computed dropping entries of  $A$  that have relative magnitude smaller than a given threshold.
2. *topological*: the sparsity pattern for any row of  $S$  can be defined according to the concept of level  $k$  neighbours. Level 1 neighbours of a node (or edge) are the node itself plus the four nodes belonging to the two triangles that share the edge. Level 2 neighbours are all level 1 neighbours plus the nodes in the triangles that are neighbours of the two triangles considered at level 1, and so forth. Three levels can generally provide a good pattern.
3. *geometric*: for each edge we select all those edges within a sufficiently large sphere that defines our geometric neighbourhood. When the surface of the object is non-smooth, large entries in the matrix may come from the interaction of far-away or non-connected edges in a topological sense, which are neighbours in a geometric sense. Thus they can be detected only using information related to the spatial distance.

For large problems, accessing all the entries of  $A$  becomes too expensive or even not possible and the algebraic strategy cannot be used. This is the case in the fast multipole framework. Fast methods partition the mesh of the object by recursive subdivision into disjoint aggregates or boxes of small size compared to the wavelength, each roughly formed by an equal number of separate triangles. Interactions of degrees of freedom within neighbouring boxes (they are 26 in 3D) are computed exactly and are available for the construction of the preconditioner, while interactions between far-away cubes are approximated using multipole techniques. With the help of the addition theorem, we may write

$$A = A_{diag} + A_{near} + A_{far},$$

where  $A_{diag}$  is the block diagonal part of  $A$ ,  $A_{near}$  is the block near-diagonal part of  $A$  and  $A_{far} = U\Lambda V$  is the far part of  $A$  (here  $U, \Lambda, V$  are sparse matrices). In this case, we take  $S = A_{diag} + A_{near}$ .

Much research work for preconditioning dense linear systems arising from the discretization of integral equations has been based on algebraic considerations, i.e. the preconditioner  $M$  is computed only looking at the entries of  $S$ ; it is a close approximation to either  $S$  or  $S^{-1}$ . In [8] Carpentieri et al. report on experiments with incomplete Cholesky factorizations with dropping strategy based on level of fill for solving symmetric indefinite systems arising from the discretization of EFIE. The preconditioning matrix  $M \approx S$  is written in the form

$$M = \mathcal{L}\mathcal{D}\mathcal{L}^T, \quad (1)$$

where  $\mathcal{D}$  and  $\mathcal{L}$  stand for, respectively, a diagonal and a unit lower triangular matrix. Owing to indefiniteness of the coefficient matrix, it is observed that the numerical behaviour of incomplete Cholesky can be fairly chaotic. The factorization of a very sparse approximation of the coefficient matrix can be stable and deliver a good rate of convergence, especially if at least one level of fill-in is retained. For higher values of density for the approximation of  $A$ , the factors may become very ill-conditioned and consequently the preconditioner is very poor. A complex diagonal perturbation can help to compute a more stable factorization, and in some cases the performance of the preconditioner can significantly improve. However, tuning the shifting parameter is not easy and its effect is difficult to predict. On the other hand, successful experiments with incomplete factorizations with dropping strategies based on threshold are reported on surface integral equations in [9] and on hybrid surface/volume integral equations in [10]. In [9], numerical difficulties due to indefiniteness of the system are successfully circumvented by using pivoting; it is shown that the resulting preconditioner can be numerically stable and maintain the memory and algorithmic complexity of the fast multipole algorithm.

A natural way to compute an approximation to  $S^{-1}$  is based on Frobenius-norm minimization. The approximate inverse is computed as the matrix  $M$  which minimizes  $\|I - MS\|_F$  (or  $\|I - SM\|_F$  for right preconditioning) subject to certain sparsity constraints. The Frobenius norm allows to decouple the constrained minimization problem into  $n$  independent linear least-squares problems, one for each column of  $M$  (when preconditioning from the right) or row of  $M$  (when preconditioning from the left). The independence of these

least-squares problems follows immediately from the identity:

$$\|I - MS\|_F^2 = \|I - SM^T\|_F^2 = \sum_{j=1}^n \|e_j - Sm_{j\bullet}\|_2^2 \quad (2)$$

where  $e_j$  is the  $j$ th canonical unit vector and  $m_{j\bullet}$  is the column vector representing the  $j$ th row of  $M$ . An analogous relation holds for right preconditioning. In the multipole framework, the box-wise decomposition of the object naturally leads to an *a priori* pattern selection strategy for the approximate inverse using geometric information, that is on the spatial distribution of the degrees of freedom. In the context of fast methods we will adopt the following criterion: the nonzero structure of the column of the preconditioner associated with a given edge in the mesh is defined by retaining all the edges within the box itself and one level of neighboring boxes. Thus the approximate inverse has a sparse block structure; each block is a dense matrix associated with one box. Indeed the least-squares problems corresponding to edges within the same box are identical because they are defined using the same nonzero structure and the same set of entries. It means that we only have to compute one  $QR$  factorization per box. In Table 1-2 we report on some results extracted from [11] on the numerical and parallel scalability of the preconditioner for solving large surface integral equations in electromagnetism. It can be seen that the preconditioner is perfectly parallelizable and maintain the same complexity of the fast multipole algorithm. Finally, we mention that Lee et al. have successfully used approximate inverses in [12] for solving hybrid surface/volume integral equations as well.

On large-scale problems, iterative solvers may exhibit a lack of scalability because information associated with the far-field are completely lost in the preconditioner based on sparsification strategies. Some global behavior of the discrete Green's function can be recovered introducing multilevel mechanisms. In the two-grid scheme proposed in [13], the first-level preconditioner  $M$  defines a weighted stationary method that implements the smoother, and the coarse space is defined using a Galerkin formula  $A_c = R^H A P$ , where  $R$  and  $P$  are the restriction and the prolongation operator, respectively. After  $\mu$  smoothing steps, the residual is projected by means of the operator  $R$  into the coarse subspace, and the coarse space error equation involving  $A_c = R^H A P$  is solved. Finally, the error is prolonged back in the original space using the operator  $P$  and the new approximation is smoothed again. These two contributions are summed together for the solution update. The grid-transfer operators are defined algebraically:  $P$  is the set of right eigenvectors associated with the set of eigenvalues  $\lambda_i$  of  $MA$  with  $|\lambda_i| \leq \varepsilon$  and  $R$  is chosen to be orthogonal to  $P$ .

In [11], Carpentieri et al. describe an inner-outer iterative schemes based on the FGMRES algorithm [14] with different levels of accuracy for the inner and outer matrix-vector products. The intent is to try to balance the locality of the preconditioner with the use of the multipole matrix. A sparse approximate inverse is used as local preconditioner for the inner solver. The numerical results of Table 3, extracted from [11], show that the two-level mechanism can enhance the robustness of the preconditioner significantly.

Numerical scalability results						
Size	Density $M$	Time $M$	GMRES( $\infty$ )		GMRES(120)	
			Iter	Time	Iter	Time
94704	0.28	11m	746	2h 9m	1956	3h 13m
213084	0.13	31m	973	7h 19m	+2000	7h 56m
591900	0.09	1h 30m	1461	16h 42m <sup>(64)</sup>	+2000	1d 57m
1160124	0.02	3h 24m	M.L.E. <sup>(64)</sup>	N.A.	+2000	> 4d

Table 1: Number of matrix-vector products and elapsed time required to converge on an aircraft problem on eight processors of the Compaq machine, except those marked with <sup>(k)</sup>, that were run on  $k$  processors. Tolerance for the iterative solution is  $10^{-3}$ . Acronyms: N.A.  $\equiv$  not available. M.L.E.  $\equiv$  memory limits exceeded.

Parallel scalability results				
Problem size	Nb procs	Construction time (sec)	Elapsed time precondition (sec)	Elapsed time mat-vec (sec)
112908	8	513	0.39	1.77
221952	16	497	0.43	2.15
342732	24	523	0.47	3.10
451632	32	509	0.48	2.80
900912	64	514	0.60	3.80

Table 2: Parallel scalability of the iterative solver on the aircraft problem.

Inner-outer iterative scheme				
Size	Density $M$	Time $M$	FGMRES(30)/GMRES(60)	
			Iter	Time
94704	0.28	11m	27+1560	2h 14m
213084	0.13	31m	34+1920	5h
591900	0.09	1h 30m	57+3300	1d 9h 45m
1160124	0.02	3h 24m	51+2940	16h 41m <sup>(64)</sup>

Table 3: Number of inner/outer matrix-vector products and elapsed time required to converge on the aircraft problem on 8 processors of the Compaq machine. The tests were run on 8 processors of the Compaq machine, except those marked with <sup>(k)</sup>, that were run on  $k$  processors.

### 3 Conclusions

In this paper we have presented the framework of preconditioners based on sparsification strategies for solving large-scale dense linear systems of equations arising from the boundary integral formulation of electromagnetic scattering problems. We have reviewed some recent results obtained with incomplete factorization and sparse approximate inverse preconditioners combined with the fast multipole method. Sparse approximate inverse are computationally attractive for their inherent parallelism and show remarkable numerical stability on indefinite formulations such as EFIE. Although not naturally suited for parallel implementation, incomplete factorization can be cheaper to compute but they have to be enhanced with pivoting strategies to overcome instabilities that may lead to ill-conditioned triangular factors. When computed from the near-part of the coefficient matrix, both classes of methods can maintain the algorithmic complexity of the fast multipole method.

## References

- [1] J. Rahola and S. Tissari. Iterative solution of dense linear systems arising from the electrostatic integral equation in MEG. *Physics in Medicine and Biology*, 47(6):961–975, 2002.
- [2] K. Forsman, W. Gropp, L. Kettunen, and D. Levine. Volume integral equations in nonlinear 3-d magnetostatics. *International Journal of Numerical Methods in Engineering*, 38:2655–2675, 1995.
- [3] W. C. Chew, J. M. Jin, C. C. Lu, E. Michielssen, and J. M. Song. Fast solution methods in electromagnetics. *IEEE Transactions on Antennas and Propagation*, 45(3):533–543, 1997.
- [4] M. Bebendorf. Approximation of boundary element matrices. *Numerische Mathematik*, 86(4):565–589, 2000.
- [5] L. Greengard and V. Rokhlin. A fast algorithm for particle simulations. *Journal of Computational Physics*, 73:325–348, 1987.
- [6] W. Hackbush. A sparse matrix arithmetic based on  $\mathcal{H}$ -matrices. *Computing*, 62(2):89–108, 1999.
- [7] B. Carpentieri, I. S. Duff, and L. Giraud. Sparse pattern selection strategies for robust Frobenius-norm minimization preconditioners in electromagnetism. *Numerical Linear Algebra with Applications*, 7(7-8):667–685, 2000.
- [8] B. Carpentieri, I. S. Duff, L. Giraud, and M. Magolu monga Made. Sparse symmetric preconditioners for dense linear systems in electromagnetism. *Numerical Linear Algebra with Applications*, 11(8-9):753–771, 2004.
- [9] T. Malas and L. Gürel. Incomplete LU preconditioning with multilevel fast multipole algorithm for electromagnetic scattering. *SIAM J. Scientific Computing*, 2007. Accepted for publication.
- [10] J. Lee, C.-C. Lu, and J. Zhang. Incomplete LU preconditioning for large scale dense complex linear systems from electromagnetic wave scattering problems. *J. Comp. Phys.*, 185:158–175, 2003.
- [11] B. Carpentieri, I. S. Duff, L. Giraud, and G. Sylvand. Combining fast multipole techniques and an approximate inverse preconditioner for large electromagnetism calculations. *SIAM J. Scientific Computing*, 27(3):774–792, 2005.
- [12] J. Lee, C.-C. Lu, and J. Zhang. Sparse inverse preconditioning of multilevel fast multipole algorithm for hybrid integral equations in electromagnetics. *IEEE Transactions on Antennas and Propagation*, 52(9):2277–2287, 2004.
- [13] B. Carpentieri. A matrix-free two-grid preconditioner for boundary integral equations in electromagnetism. *Computing*, 77(3):275–296, 2006.
- [14] Y. Saad. A flexible inner-outer preconditioned GMRES algorithm. *SIAM J. Scientific and Statistical Computing*, 14:461–469, 1993.

## BEM formulation for reinforced plates

Leandro Waidemam & Wilson S. Venturini

São Carlos School of Engineering – University of São Paulo  
Av. Trabalhador São-Carlense, 400, 13566-970 – São Carlos, Brazil.  
[waidemam@sc.usp.br](mailto:waidemam@sc.usp.br) & [venturin@sc.usp.br](mailto:venturin@sc.usp.br)

Keywords: plate bending, reinforcements

### Astract.

In this article a BEM formulation developed to analyse reinforced plate bending. The reinforcements are formulated using a simplified scheme based on applying an initial moment field to correct locally the stiffness of the reinforcement region. The domain integrals due to the presence of the reinforcements are transformed to the reinforcement boundaries. The stiffness increase can be independently considered for each component. Thus, one may conveniently reduce the number of degree of freedom required to consider the reinforcement. Examples are presented to confirm the accuracy of the formulation.

### Introduction

The boundary element method (BEM) has experienced an enormous growth in the last two decades and became a reliable numerical method alternative to solve many problems in Engineering. Analysis of plate bending problems is among the applications the method has demonstrated to be accurate and very efficient. For this problem the method is appropriate to deal with internal force concentration and with the presence of small loaded regions. Moreover, all boundary values are approximated by using polynomial shape function of the same order leading to more accurate results for bending and shear forces in comparison with other numerical techniques.

The direct formulation of the method was proposed in the end of seventies by Bézine [1], Tottenham [2] and Stern [3] among others. So far many other works have been published demonstrating that the BEM reliability for applications in engineering [4-8].

Analysis of reinforced plates is a kind of problem very often found in structural engineering design. The combination of BEM applied to the plate domain with FEM used to approximate the linear elements (beams) is an interesting scheme; the advantages of each method are taken into consideration [9-12]. For this combination the simplifications and the approximations are assumed for each individual element before the coupling procedure, which is performed by using displacement compatibility and interactive force equilibrium along the interfaces. Although these approximations and simplifications are acceptable in terms of final results the number of degrees of freedom can increase too much for problems with many reinforcement elements leading to large computer time and less accurate numerical solutions.

The senior author of this work has already published several papers showing BEM formulation that take into account the presence of reinforcement or regions with different rigidity [13-15]. In those formulations we have adopted the sub-region technique, but the equilibrium conditions are enforced before the interface approximations resulting to a system containing only displacements unknowns along the interface. In this work the reinforcements is introduced by correction the rigidity over the thin-region using an initial moment field as used to take into account temperature changes or to computer the correction term in BEM non-linear formulations. The beam hypothesis are then considered reducing the required number of degrees of freedom to one per each node adopted to discretize the reinforcement line. Examples are then solved to show the applicability of the formulation.

### Basic Equations

Consider an isotropic defined by the domain  $\Omega$  and boundary  $\Gamma$  with an internal reinforcement as shown in Fig 1. The load  $g$  perpendicular to the plate surface is applied over a sub-region  $\Omega_g$ . Figures

1a and 1b describe two different way to introduce the reinforcements: reinforcement with different material but preserving the thickness; using the same material but using a different height sub-region.

For the plate bending problem one can write the equilibrium equations:

$$M_{ij,i} - Q_j = 0 \text{ and } Q_{i,i} + g = 0 \tag{1}$$

where  $M_{ij}$  is the bending and twisting moments and  $Q_j$  are the shear forces.

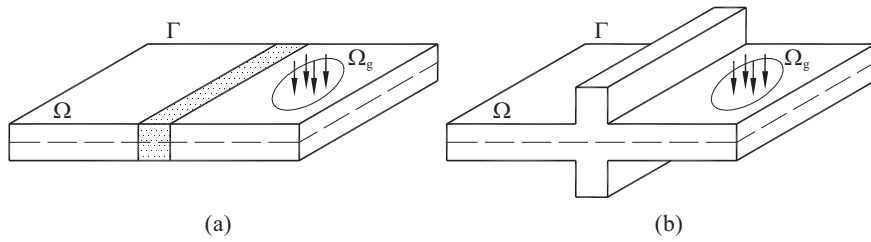


Figure 1. Reinforced plate: a) different materials; b) different heights.

The differential equation written in terms of deflections is:

$$Dw_{,ijij} = g \tag{2}$$

where  $D = Et^3/12(1-\nu^2)$  gives the flexural rigidity,  $t$  is the plate thickness and  $E$  and  $\nu$  are the Young's modulus and the Poisson's ratio, respectively.

The internal forces given in terms of deflection derivatives are:

$$M_{ij} = -D[\nu\delta_{ij}w_{,kk} + (1-\nu)w_{,ij}] \text{ and } Q_i = -Dw_{,jji} \tag{3}$$

**Integral equations**

For a domain exhibiting regions with different rigidity one may write the Betti's reciprocity as follows:

$$\int_{\Omega} M_{ij}^* w_{,ij} d\Omega = \int_{\Omega} M_{ij} w_{,ij}^* d\Omega + \int_{\Omega_e} M_{ij}^D w_{,ij}^* d\Omega_e \tag{4}$$

where  $\Omega_e$  is the reinforced domain and  $M_{ij}^D$  is a initial moment field that is assumed to correct the plate stiffened.

Integrating by parts equation (4) one obtains the integral representation of deflections, as follows:

$$Cw + \int_{\Gamma} (V_n^* w - M_n^* \partial w / \partial n) d\Gamma + \sum_{i=1}^{N_c} R_{ci}^* w_{ci} = \int_{\Gamma} (V_n w^* - M_n \partial w^* / \partial n) d\Gamma + \sum_{i=1}^{N_c} R_{ci} w_{ci}^* + \int_{\Omega_g} g w^* d\Omega - \int_{\Omega_e} M_{ij}^D w_{,ij}^* \Omega \tag{5}$$

where  $V_n$ ,  $M_n$ ,  $w$  and  $\partial w / \partial n$  are equivalent shear force, normal bending moment, deflection, and normal rotation boundary values, respectively;  $R_c$  and  $w_c$  are corner reactions and deflections;  $V_n^*$ ,  $M_n^*$ ,  $R_{ci}^*$  e  $w_{,ij}^*$  are plate bending fundamental values obtained from  $w^*$ , while  $C$  is the well-known free terms.

As for damage mechanics the corrector moment field  $M_{ij}^D$  can be given by the relations of the plate and reinforced rigidities,  $D_r$  and  $D_p$ , respectively:

$$M_{ij}^D = (1 - D_r / D_p) M_{ij}^r \quad (6)$$

Using the definition, eq. (3) the moment equation for internal points can be derived:

$$M_{ss}^r = - \int_{\Gamma} (V_{nss}^* w - M_{nss}^* \partial w / \partial n) d\Gamma - \sum_{i=1}^{N_c} R_{ci}^* w_{ci} + \int_{\Gamma} (V_n w_{ss}^* - M_n \partial w^* / \partial n_{ss}) d\Gamma + \sum_{i=1}^{N_c} R_{ci} w_{ci}^* + \int_{\Omega_g} g w_{ss}^* d\Omega + \int_{\Omega_e} M_{ss}^D w_{ssss}^* d\Omega \quad (7)$$

where the new kernels are obtained by applying the moment definition (eq 3) on the kernels of eq (5).

**Algebraic equations**

We have adopted linear continuous and discontinuous elements to approximate the boundary values. The collocations points are placed on the boundary nodes for the continuous elements case and inside the element for the discontinuous elements. Collocations are also defined outside the domain to allow writing the second equation for each node. The initial moment field is assumed constant across the beam and varying linearly along the beam skeleton line (fig. 2).

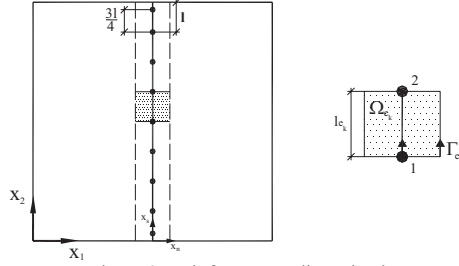


Figure 2. Reinforcement discretization.

The domain integral over the reinforcement area can be partially transformed to the boundary as follows:

$$\int_{\Omega_{ek}} w_{ss}^* M_{ss}^D d\Omega = \int_{\Gamma_{ek}} w_{ss}^* M_{ss}^D \eta_s d\Gamma - \int_{\Omega_{ek}} w_{ss}^* M_{ss,s}^D d\Omega \quad (8)$$

Assuming linear approximation the derivative of the correcting moments with respect to the beam axis

$$\partial M_{ss}^D / \partial x_s = \varphi_n^n M_{ss}^D = (-^1 M_{ss}^D + ^2 M_{ss}^D) / l_{ek} \quad (9)$$

with  $l_{ek}$  being the beam axis elements size.

Then the last integral in eq (8) can also transformed to the boundary after considering the approximations in eq (9) and performing analytically the integral over one dimension:

$$\int_{\Omega_{ek}} w_{ss}^* M_{ss,s}^D d\Omega_{ek} = [\varphi_n^n M_{ss}^D] \left[ -\frac{r_{2s}}{4\pi D} \right] \int_{\Gamma_{ek}} \frac{r^2}{3} \left[ \ln(r) - \frac{1}{3} \right] \frac{\partial r}{\partial n} d\Gamma \quad (10)$$

Thus, the integrals due the presence of  $M_{ij}^D$  will be performed along the domain/reinforcement interfaces. The collocations points (nodes defined to approximate the corrector moments) are placed along the beam axis. After the approximations (boundary domain values), the algebraic equations for deflections and internal moments are found:

$$H_p^u U_p = G_p^u P_p + T_p^u + E_p^u M_{ss}^r \quad (11)$$

$$M_{ss}^r = -H_p^M U_p + G_p^M P_p + T_p^M + E_p^M M_{ss}^r \quad (12)$$

where the matrices  $H_x^y$ ,  $G_x^y$  and  $E_x^y$  are the same ones obtained for the non-linear BEM formulations,  $T_x^y$  are the independent term due to the applied load, and  $M_{ss}^r$  is the reinforcement region moment for the nodes defined along the beam axis.

Equations (11) and (12) can be rearranged leading to the final algebraic system of equations:

$$\begin{bmatrix} A_p^u & -E_p^u \\ -A_p^M & (I - E_p^M) \end{bmatrix} \begin{bmatrix} X_p \\ M_{ss}^r \end{bmatrix} = \begin{bmatrix} B_p^u \\ B_p^M \end{bmatrix} \quad (13)$$

where  $I$  is the identity matrix.

### Example

**Reinforced Plate subject to a applied moment.** The reinforced plate of fig. 3 will be analyzed. The geometric data and applied load are given in the same figure. Two reinforced beams along the free plate side are considered. The two other plate side were assumed simply supported ( $w = M_n = 0$ ). The assumed Plate Young's modulus is  $E = 2.7 \times 10^5 \text{ MPa}$ , while the Poisson's ratio is zero. The plate and reinforcement thicknesses are  $t_p = 100\text{mm}$  and  $t_r = 250\text{mm}$ , respectively. The reinforcement factor (eq 3)  $\psi_p = -14.625$ .

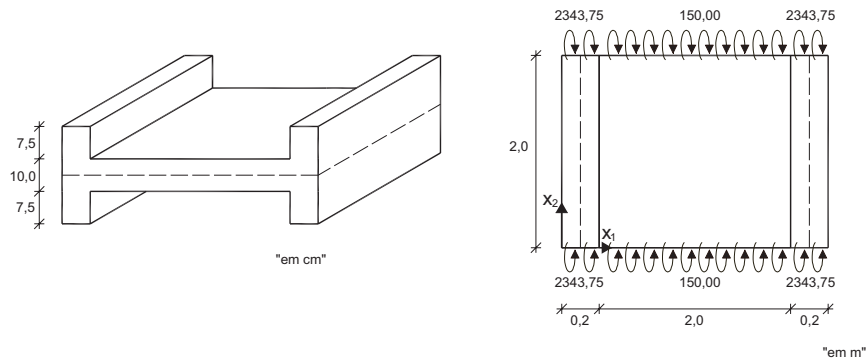


Figure 3. Reinforced plate.

We have applied moments along the plate ends to lead to the same curvatures over the plate and reinforcement regions. The combination adopted was:  $M_n^{(p)} = 150.00 \text{ kN}$  applied to the plate boundary, and  $M_n^{(r)} = (D_r/D_p) M_n^{(p)} = 2343.75 \text{ kN}$  applied to the reinforcement region boundary. For these boundary conditions the obtained solutions for the plate and the beams will be independent. The analytical values are:  $w = M(I^2/4 - x^2)/2EI$  and  $\theta = -Mx/EI$ . The plate boundary and reinforcements interface were discretized by 92 and 20 elements respectively. The numerical results given by the implemented code, shown in fig. 4 are practically the theoretical ones. We have also computed  $V_n = 0$  and  $w_n = -0.00667$  along the simple supported sides and  $w_n = 0$  along the free sides.

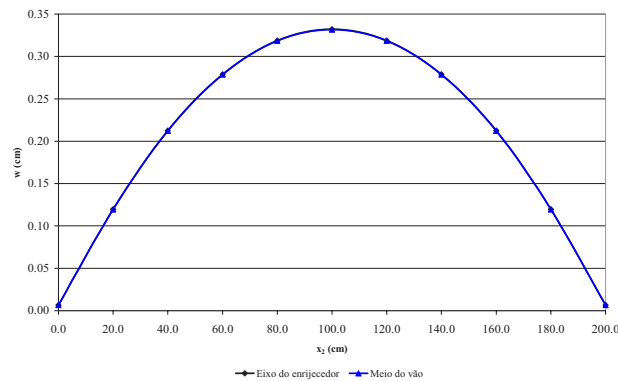


Figure 4. Deflections  $w$  along the reinforcement and the plate middle axes.

### Conclusions

We have developed a BEM formulation to analyze reinforced plate bending problems, in which a reduced number of degrees of freedom is required to take into account the beam effects. To increase only the flexural rigidity due to the beam effects, only one degree of freedom per each internal node defined along the beam axis is required. Besides the degree of freedom reduction in comparison with other BEM formulation to analyze this problem (BEM/FEM coupling, Sub-region techniques, etc.) this approach has show to be very accurate for several examples already tested.

### References

- [1] G. Bézine. Boundary integral formulation for plate flexure with arbitrary boundary conditions. *Mechanics Research Communications*, Vol. **5**, pp. 197-206, (1978).
- [2] H. Tottenham. The boundary element method for plates and shells. In: P. K. Banerjee e R. Butterfield. *Boundary element methods*. London, App. Sc. Publ., (1979).
- [3] M. Stern. A general boundary integral formulation for the numerical solution of plate bending problems. *International Journal of Solids and Structures*, Vol. **15**, pp. 769-782, (1979).
- [4] G. Bézine. A mixed boundary integral – Finite element approach to plate vibration problems. *Mechanics Research Communications*, Vol. **7**, pp. 141-150, (1980).
- [5] N. Kamiya, Y. Sawaki, Y. Nakamura e A. Fukui. An approximate finite deflection analysis of heated elastic plate by boundary element method. *Applied Mathematical Modelling*, Vol. **6**, pp. 1-72, (1982).
- [6] N. Kamiya, Y. Sawaki e Y. Nakamura Non-linear bending analyses of heated sandwich plates and shells by the boundary element method. *Res Mechanica*, Vol. **8**, pp. 29-83, (1983).
- [7] F. Van Der Weeën. Application of the direct boundary element method to Reissner's plate model. In: C. A. Brebbia. *Boundary element methods in engineering*. Berlin, Springer-Verlag, (1982).
- [8] J. T. Katsikadelis e A. E. Armenakas. Analysis of clamped plates on elastic foundation by the boundary integral method. *Journal of Applied Mechanics*, Vol. **110**, pp. 1085-1104, (1984).
- [9] C. Hu e G. A. Hartley. Elastic analysis of thin plates with beam supports. *Engineering Analysis with Boundary Elements*, Vol. **13**, pp. 229-238, (1994).
- [10] G. A. Hartley. Development of plate bending elements for frame analysis *Engineering Analysis with Boundary Elements*, Vol. **17**, pp. 93-104, (1996).

- [11] M. Tanaka e A. N. Bercin. Static bending analysis of stiffened using the boundary element method. *Engineering Analysis with Boundary Elements*, Vol. **21**, pp. 147-154, (1998).
- [12] E. J. Sapountzakis e J. K. Katsikadelis. Dynamic analysis of elastic plates reinforced with beams of doubly-symmetrical cross section. *Computational Mechanics*, Vol. **23**, pp 430-439, (1999).
- [13] G. R. Fernandes e W. S. Venturini. Stiffened plate bending analysis by the boundary element method. *Computational Mechanics*, Vol. **28**, pp. 275-281, (2002).
- [14] G. R. Fernandes e W. S. Venturini. Building floor analysis by the boundary element method. *Computational Mechanics*, Vol. **35**, pp 277-291, (2005).
- [15] G. R. Fernandes e W. S. Venturini, Non-linear boundary element analysis of floor slabs reinforced with rectangular beams. *Engineering Analysis with Boundary Elements*, Available online 23 March 2007.

## Development of cohesive boundary element for damage analysis in brittle matrix composites

D. E. Heo<sup>1</sup>, D. E. Kim<sup>1</sup>, S. S. Lee<sup>1</sup>, J. K. Lee<sup>2</sup>

<sup>1</sup>Department of Mechanical & Aerospace Engineering, Gyeongsang National University  
Jinju, 660-701, Republic of Korea, leess@gsnu.ac.kr

<sup>2</sup>Department of Mechanical Engineering, The Ohio State University, Columbus, Ohio,  
43201, U.S.A., lee.71@osu.edu

**Keywords:** cohesive model, boundary element, multiple domains, composite

### Abstract

Cohesive models are widely used for simulating fracture and fragmentation process in various materials with an increasing application. The multiple domain boundary element method (MDBEM) may be more suitable than the finite element method (FEM) since the de-bonding is also the boundary surface problem. In this study, the boundary cohesive element is implemented by modifying the cohesive model with the linear relation with the MDBEM. Numerical examples are shown to demonstrate the validity of the present procedure.

### 1. Introduction

The fiber reinforced composites have superior mechanical properties such as high strength or stiffness to weight ratio compared with conventional materials. Therefore, the commercial application of fiber reinforced composites has been increasing, especially in the aerospace industry. However, the fibers in composites matrix have adverse effects on their failure properties such as de-bonding at the fiber and matrix interface and crack in matrix [1].

Accurate interface de-bonding analysis is difficult task due to the fact that morphological and constitutive complexities govern its initiation and growth. The effects of de-bonded interfaces have been studied by several investigators by using the finite element method (FEM) [1-3]. The boundary element method (BEM) can be successfully applied to this problem. The BEM is particularly suited for the de-bonded interface problem since the unknowns of the problem are all boundary values, namely interface traction and displacement. The de-bonding problem is a multi-domain problem since the mechanical properties of fiber and matrix are different in general.

In this paper, interfacial de-bonding is accommodated by a cohesive boundary element model.

Model simulation of single fiber polymer-matrix composites is compared with the result from ABAQUS.

## 2. Boundary element method for multi-domain

### 2.1 Single domain boundary element

The boundary equation can be expressed as follows.

$$c_{ij}u(x') + \int_{\Gamma} T_{ij}(x', x)u_j(x)d\Gamma(x) = \int_{\Gamma} U_{ij}(x', x)t_j(x)d\Gamma(x), \quad (1)$$

where  $c_{ij}(x') = \frac{1}{2}$  on the boundary surface. Here  $U_{ij}(x', x)$  and  $T_{ij}(x', x)$  are the fundamental solutions to the well-known Kelvin problem and  $u_j(x)$  and  $t_j(x)$  are the displacement and traction on the boundary. The two dimensional equation can be expressed as follows.

$$U_{ij}(x', x) = \frac{1}{8\pi\mu(1-\nu)} \left\{ (3-4\nu) \ln\left(\frac{1}{r}\right) \delta_{ij} + r_{,i} r_{,j} \right\} \quad (2)$$

$$T_{ij}(x', x) = \frac{1}{4\pi(1-\nu)r} \left\{ \frac{\partial r}{\partial n} [(1-2\nu)\delta_{ij} + 2r_{,i} r_{,j}] - (1-2\nu)(r_{,i} n_j - r_{,j} n_i) \right\} \quad (3)$$

For numerical implementation, the boundary equation can be written in the following matrix form by dividing the boundary surface into continuous element:

$$HU = GT \quad (4)$$

where U is the displacement vector and T is the traction vector on the surface of the region.

The fundamental solutions for plane stress can be obtained by changing material properties with the following relations.

$$\nu' = \frac{\nu}{1+\nu}, \quad E' = E \left[ 1 - \left( \frac{\nu}{1+\nu} \right)^2 \right] \quad (5)$$

2.2 Multi-domain boundary element analysis

In the multi-domain boundary element, displacement and traction at the interfacial surface between two domains are unknown. We use the notion that ‘stiffness matrix  $K$ ’ of each region is the traction due to unit displacement, according to the finite element method. Then the matrices  $K$  for all regions are then assembled in the same way as with the FEM [4].

The multi-domain boundary element has two different domains  $V_1$  and  $V_2$ , which have interface surface  $S_1$  and outer boundary surfaces  $S_1$  and  $S_2$ , as shown in Fig.1. Domain  $V_1$  and  $V_2$  may have different mechanical properties

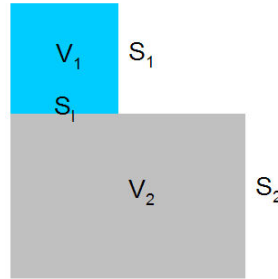


Fig. 1: Concept of multi-domain boundary element

For the computation of Dirichlet problem, we use the equation (4) with modified right hand side vector  $U_i$

$$HU_i = GT_i \tag{6}$$

where,  $U_1$  is a vector with a unit value in the first row, i.e.

$$U_1 = \begin{Bmatrix} 1 \\ 0 \\ 0 \\ \cdot \\ \cdot \\ \cdot \end{Bmatrix}, \quad U_2 = \begin{Bmatrix} 0 \\ 1 \\ 0 \\ \cdot \\ \cdot \\ \cdot \end{Bmatrix} \tag{7}$$

If we solve the eq. (6) for  $T_1$ , since  $U_1$  is known, then  $T_1$  is the first column of the stiffness matrix  $K$  and each solution vector  $T_i$  represents a column in  $K$ , i.e.

$$K = [T_1 \quad T_2 \quad \dots] \quad (8)$$

For domain-k, we can write the following relation between the traction  $T^k$  and the displacement  $U^k$ .

$$K^k U^k = T^k \quad (9)$$

In the interfacial surface between two domains, the tractions and displacements can be written as

$$T^1 + T^2 = T \quad ; \quad U^1 = U^2 = U \quad (10)$$

Where,  $T$  is the applied traction vector at the interfacial surface.

By applying eq. (10) into eq. (9), the assembled system of equation for the interfacial surface between two domains is simply written as

$$(K^1 + K^2)U = T \quad (11)$$

If the displacement in the interfacial surface is solved from eq. (11), then the displacement and traction for each domain can be obtained by a single domain equation.

### 3. Development of cohesive boundary element

A cohesive element based on the FEM was developed for modeling adhesive and bonded interface behavior, which can be connected to the adjacent element by sharing nodes. In the cohesive element, the traction and displacement is modeled as shown in Fig.2. The basic idea of the cohesive element is that the element has some stiffness before the traction reaches the maximum stress and applies the traction boundary condition after the maximum stress, which means the material separation occurs within the cohesive element.

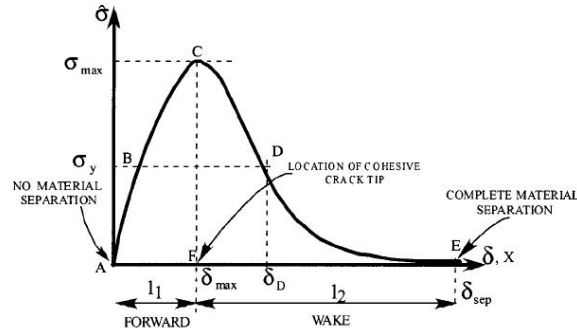


Fig. 2: Traction and displacement law in cohesive model in FEM

In the multi-domain boundary element method, the basic concept of the cohesive boundary element is shown in Fig. 3. We separate the traction and displacement relation into two part, forward and wake part and assume that the material separation occurs at location of cohesive crack tip point C as shown in Fig. 3. Since the forward part from point A to point C as shown in Fig.3 (a) has no material separation in interface surface, this part can be treated by the interfacial boundary element between point A and C as shown in Fig.3 (b). The wake part from point C to E as shown in Fig.3 (a), which is modeled with the separated boundary element between point C and E as shown in Fig.3 (b) and applied with the traction and displacement relation as shown in Fig. 4.

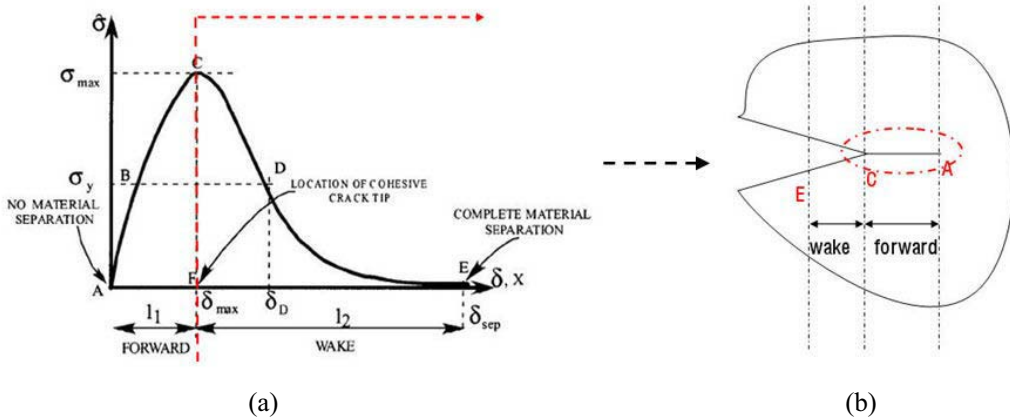


Fig. 3: Concept of the cohesive model in MDBEM

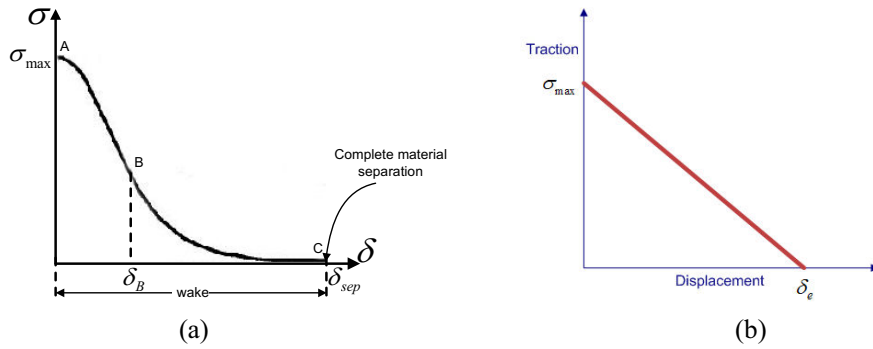


Fig. 4: Modified traction and displacement law in MDBEM ((a): exponential, (b): linear)

We apply the cohesive boundary element along the interfacial surface between two domains as shown in Fig.5 (a) and the normal and tangential direction are shown in Fig.5 (b), which are defined along the interfacial surface line.

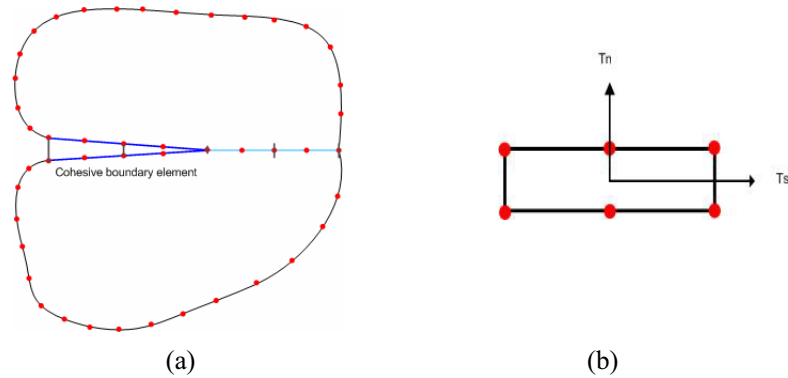


Fig. 5: Cohesive boundary element (a) cohesive element along the interface surface, (b) normal and tangential direction of the cohesive boundary element

For numerical convenience, we apply the linear traction and displacement relation as shown in Fig.4 (b), proposed by Camacho and Ortiz [5]. The relation of the traction and displacement in the cohesive boundary element is given as follows. When the traction reaches the maximum stress, the traction  $t$  and displacement  $\delta$  relation is express as follows

$$t = \sigma_{\max} (1 - \delta / \delta_e) \quad 0 \leq \delta \leq \delta_e \quad (14)$$

where  $\sigma_{\max}$  is the maximum stress and  $\delta_e$  is the maximum displacement.

The normal and tangential traction-separation behavior for linear cohesive model are shown in Fig.6 and the relations are expressed as;

$$T_n = \sigma_{\max} \left(1 - \frac{\delta}{\delta_e}\right) \frac{\delta_n}{\delta} \quad 0 \leq \delta \leq \delta_e \quad (15)$$

$$T_t = \sigma_{\max} \left(1 - \frac{\delta}{\delta_e}\right) \beta^2 \frac{\delta_t}{\delta} \quad 0 \leq \delta \leq \delta_e \quad (16)$$

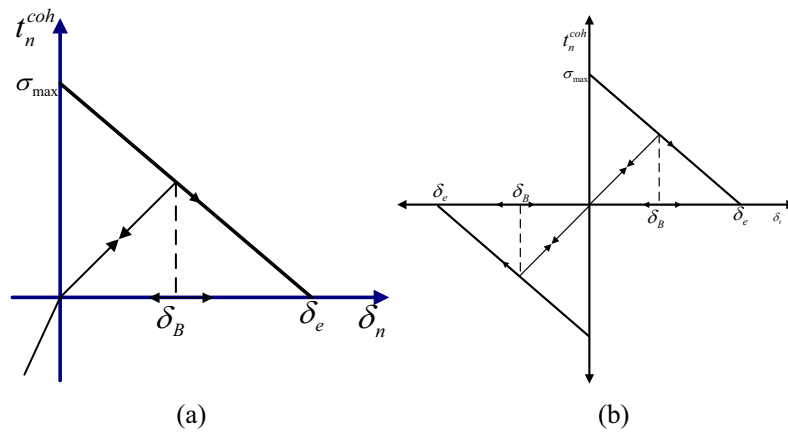


Fig. 6: Normal (a) and tangential (b) traction-separation behavior for the linear cohesive model

When the load is unloaded, the traction and displacement relation is expressed as follows.

$$t = \frac{\sigma_{\max}}{\delta_B} \left(1 - \frac{\delta_B}{\delta_e}\right) \delta \quad (17)$$

where  $\delta_B$  is the displacement at the previous equilibrium state.

The cohesive boundary element is easily applied when the multi-domain boundary element method is used even if the materials are different or not.

#### 4. Numerical application

We have simulated the de-bonding problem of the composite with a steel fiber as so shown in Fig.7. The geometric properties of the composite include a  $6mm \times 6.82mm$  epoxy domain with a circular steel of radius  $2.36mm$ .

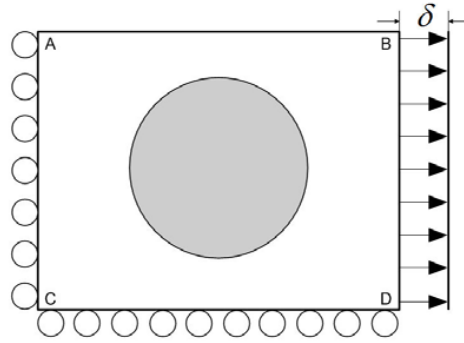


Fig. 7: The boundary condition of composite model

The material properties are:  $E_{steel} = 210GPa$ ,  $\nu_{steel} = 0.3$ ,  $E_{epoxy} = 4.7GPa$ ,  $\nu_{steel} = 0.4$ . We applied boundary conditions as shown in Fig.7. The displacement boundary condition is applied along the line BD. For the linear model the cohesive element parameters are:  $\sigma_{max} = 0.0037GPa$ ,  $\delta_e = 0.0007$  and  $\beta = 0.707$ . The boundary element model and finite element model for the problem are shown in Fig.8.

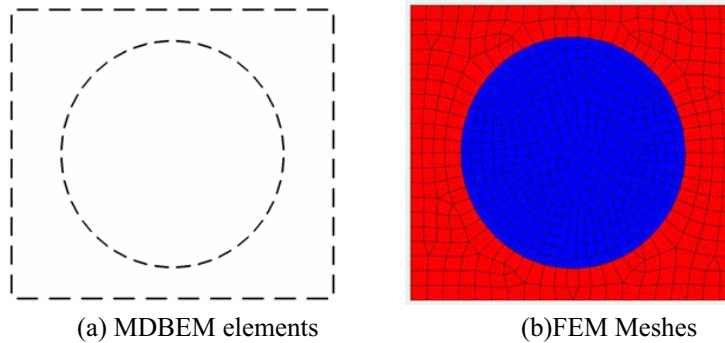


Fig. 8: Boundary elements and Finite elements configuration of the composite model

The macroscopic stress-strain are defined as follows,

$$\sigma_m = \frac{\int_c^A \sigma_x ds}{\text{Length between point A and C}} \quad (18)$$

$$\varepsilon_m = \frac{\delta}{\text{Length between point C and D}} \quad (19)$$

The macroscopic stress-strain response is shown in Fig. 9, which shows that the MDBEM results match the ABAQUS [6] simulation results very well. In Fig.8, the de-bonding occurs near  $1.8 \times 10^{-4}$  macroscopic strain. Before the de-bonding, the macroscopic

stiffness of the composite is larger than the epoxy material since the elastic modulus of the steel in the composite is about 44 times larger than that of the epoxy.

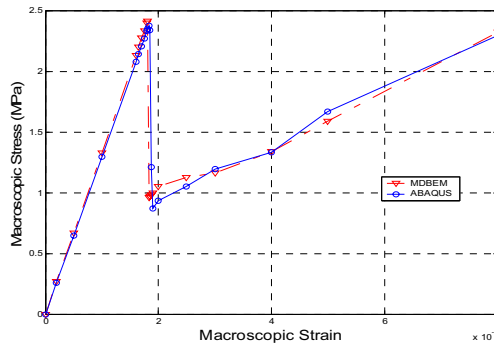
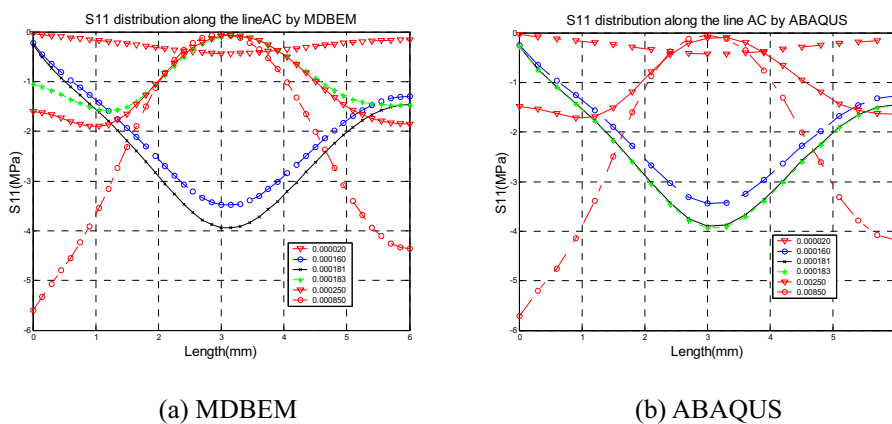


Fig. 9: Comparison of macroscopic stress-strain response

The traction distributions of each the macroscopic strains along the line AC are shown in Fig.10. The traction distributions show that the MDBEM simulation results are almost the same as those of the ABAQUS except the macroscopic strain is 0.000183 as shown in Fig. 9. At this macroscopic strain, the de-bonding occurs in MDBEM simulation but does not occur in ABAQUS simulation due to the difference of the numerical method. Before the de-bonding, the tractions in middle part is higher than those in end parts but after de-bonding, the traction distribution is reverse since the de-bonding occurs in the middle of the composite and changes the load path into the end parts. These results are a good agreement with the physical phenomena.



(a) MDBEM

(b) ABAQUS

Fig. 10: Traction distribution along the line AC

## 5. Conclusion

We developed the cohesive boundary element for the de-bonding problem using MDBEM. The simulation result matches well that of the ABAQUS. The MDBEM can be used for cohesive element in de-bonding problems of composite model. We will develop the 2-D boundary element method for orthotropic materials and application for MEMS reliability analysis.

## Acknowledgment

The authors wish to acknowledge financial supports from 2005 GSNU sabbatical leave program, BK21 and NURI support during the research.

## Reference

- [1] S. Li and S. Ghosh, 2004, “ Debonding in composite microstructures with morphological variations”, *International Journal of computational methods*,1(1):121-149.
- [2] D. Xie and A. M. Waas, 2006,” Discrete cohesive zone model for mixed-mode fracture using finite element analysis”, *Engineering Fracture Mechanics* 73:1783-1796.
- [3] C. Shet, N. Chandra, 2002, “Analysis of Energy Balance When Using Cohesive Zone Models to Simulate Fracture Processes”, *Transaction of the ASME*, vol. 124:440-450.
- [4] G. Beer, *Programming the Boundary Element Method*, John Wiley & Sons, LTD, 2001.
- [5] G. T. Camacho and M. Ortiz , 1996, “Computational Modeling of Impact Damage in Brittle Materials”, *Int. J. Solids Struct.*, 33:2899-2938.
- [6] ABAQUS user’s manual-version 6.5, Hibitt, Karlsson and Sorenson, Pawtucket, R.I. 2005.

## Analysis of composite laminates with imperfect bonding conditions

A. Alaimo<sup>1</sup>, I. Benedetti<sup>2</sup> and A. Milazzo<sup>1</sup>

<sup>1</sup>Dipartimento di Tecnologie ed Infrastrutture Aeronautiche, Università di Palermo, Viale delle Scienze, Edificio 8, 90128, Palermo, Italy.

<sup>2</sup>Dipartimento di Ingegneria Aerospaziale, Università di Pisa, Via Caruso, 56126, Pisa, Italy.

**Keywords:** Boundary Element Method, Imperfect interface, Laminates, Interlaminar Stresses.

**Abstract.** A multidomain boundary integral formulation for the analysis of composite laminates with imperfect interlaminar interfaces is presented. An imperfect interface refers to a zero-thickness interfacial layer across which displacement discontinuity may occur while interlaminar tractions must remain continuous. The displacement discontinuity is considered through a spring model in order to model the adhesive layer among two adjacent laminae. No auxiliary elements are needed to implement the imperfect interface since the spring coefficients, characterizing the different bonding interface conditions, are taken into account inside the assembled influence matrices. To assess the reliability and the effectiveness of the model some numerical analyses have been carried out on the bending response of composite laminates with different interface bonding conditions. A symmetric cross ply laminate has also been analyzed and the effects of a weak interface on the peel stresses have been pointed out.

**Introduction.** The increased demand of laminated composite structures in many engineering applications is a direct result of the requirements for higher strength-to-weight and stiffness-to-weight ratios, better corrosion resistance, longer fatigue life, greater stealth characteristic over metals as well as directionality properties [1]. A comprehensive understanding of the mechanical behavior of these structures leads to an accurate determination of their load carrying capability, contributing to the enhancement, without weight penalties, of their performance.

The inherent anisotropy and mismatch in the material properties of these materials induce a generally complex three-dimensional stress state characterized by high interlaminar stresses [2]. The accurate prediction of interlaminar stresses is of capital importance to effectively prevent composite laminate failure. On the other hand interlaminar stresses and the overall behavior of composite laminates are significantly affected by the nature of the bonding between two adjacent laminae. For this reason, in many practical cases, the assumption of perfect interface, which implies the continuity of displacement across the interface, reveals itself inadequate [3,4,5]. To achieve a more accurate prediction of the displacement fields and of the complex interlaminar stress state, many imperfect interlaminar interface models have been developed for the analysis of composite laminates [3,4,6,7].

In this paper the characterization of the imperfect bonding conditions at the interface has been approached by using a spring model [8,9,10], which is based on the assumption that the displacement jump at the interface is proportional to the traction. This interface model has been implemented into a multidomain boundary element approach avoiding auxiliary interfacial nodes. Additionally, to avoid the inconsistency of overlapping at the interface between nodes belonging to different domains, unilateral interface conditions have been considered by using an iterative solution procedure.

Bending response of composite laminates has been first analyzed to compare the results of the present method with benchmark problems whose results are available in the literature. Emphasis has then been placed on the effects of a weak interface on the peel stress at the interface of a laminate.

**Basic Equations.** The formulation is developed for two-dimensional anisotropic domain  $\Omega$  with boundary  $\partial\Omega$  lying in the  $x_1, x_2$  plane under the hypothesis of linear elasticity and generalized plain strain. The governing equations of the problem, completed by the boundary conditions, are

$$\mathcal{D}^T \mathbf{E} \mathcal{D} \mathbf{U} + \mathbf{f} = \mathbf{0} \quad \text{with} \quad \begin{cases} \mathbf{u} = \bar{\mathbf{u}} & \text{on } \partial\Omega_u \\ \mathbf{t} = \mathcal{D}_n^T \mathbf{E} \mathcal{D} \mathbf{U} = \bar{\mathbf{t}} & \text{on } \partial\Omega_t \end{cases} \quad (1)$$

where the operators  $\mathfrak{D}$  and  $\mathfrak{D}_n$  are defined as [11,12]. Applying the reciprocity theorem and considering a particular displacement field corresponding to a concentrated force acting in an infinite domain and applied at the point  $P_0$ , the well known Somigliana identity is obtained

$$\mathbf{c}^* \mathbf{u}(P_0) + \int_{\partial\Omega} (\mathbf{t}^* \mathbf{u} - \mathbf{u}^* \mathbf{t}) d\partial\Omega = \int_{\Omega} \mathbf{u}^* \mathbf{f} d\Omega \tag{2}$$

where  $\mathbf{u}^*$  and  $\mathbf{t}^*$  are the problem fundamental solutions and the matrix  $\mathbf{c}^*$  can be calculated according to [12]. The boundary integral formulation is numerically implemented by using the boundary element method [13] which provides a linear algebraic resolving system expressed in terms of displacements and tractions nodal values  $\boldsymbol{\delta}$  and  $\mathbf{P}$ , respectively

$$\mathbf{H}\boldsymbol{\delta} + \mathbf{G}\mathbf{P} = \mathbf{0} \tag{3}$$

This coupled with the applied boundary conditions determines the solution of the problem for a single domain.

**Multidomain BEM and interface model.** The multidomain boundary element technique [11,13] consists of the partition of the original domain into homogeneous subregions so that Eq. (3) still hold for each single subdomain and the following equations can be written

$$\sum_{j=1}^M \mathbf{H}_{ij}^i \boldsymbol{\delta}_{ij}^i = \sum_{j=1}^M \mathbf{G}_{ij}^i \mathbf{P}_{ij}^i \quad i = 1, 2, \dots, M \tag{4}$$

where  $M$  is the number of subregions considered, the superscript  $i$  indicates quantities associated with the  $i$ -th subdomain, while the subscript  $ij$  relate quantities to the nodes belonging to the interface between the  $i$ -th and  $j$ -th subdomains (Fig.1), provided that for  $i=j$  the nodes belong to the external boundary of the  $i$ -th subdomain. In the Eq. (4)  $\mathbf{H}_{ij}^i$  and  $\mathbf{G}_{ij}^i$  denote the matrices of influence coefficients pertaining to the quantities  $\boldsymbol{\delta}_{ij}^i$  and  $\mathbf{P}_{ij}^i$ , respectively. To obtain the solution of the problem, the “domain integrity” needs to be restored by enforcing the displacement continuity and traction equilibrium conditions along the interfaces between contiguous subdomains. If perfect bonding is prescribed, the interface compatibility and equilibrium conditions can be written as

$$\boldsymbol{\delta}_{ij}^i = \boldsymbol{\delta}_{ji}^j \text{ and } \mathbf{P}_{ij}^i = -\mathbf{P}_{ji}^j \quad i = 1, \dots, M-1; \quad j = i+1, \dots, M \tag{5}$$

On the other hand, if imperfect interface is considered, the traction equilibrium conditions remain the same as in Eq. (5) while the displacements of the coincident nodes belonging to the interface are non longer equal. Indicating with  $\Delta\boldsymbol{\delta}^{ij}$  the vector of displacement jumps across the interface between the  $i$ -th and  $j$ -th subdomains, the imperfect bonding compatibility conditions can be written as

$$\boldsymbol{\delta}_{ji}^j = \boldsymbol{\delta}_{ij}^i + \Delta\boldsymbol{\delta}^{ij} \quad i = 1, \dots, M-1; \quad j = i+1, \dots, M \tag{6}$$

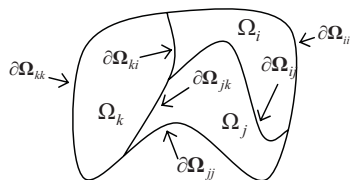


Fig.1 Multidomain configuration.

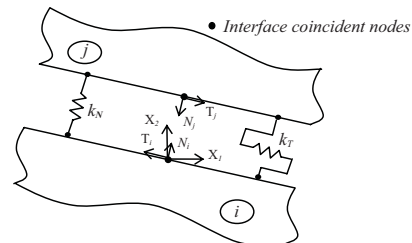


Fig.2 Spring model at interface.

The normal and tangential components of the interface displacement jumps,  $\Delta\delta_N^j$  and  $\Delta\delta_T^j$ , are expressed as a function of the normal and tangential components of the nodal tractions. Referring to local coordinate systems centered at each node belonging to the interface boundary of the domain  $i$ , as shown in Fig. 2, one writes

$$\begin{aligned} \delta_N^j &= \delta_N^i + \Delta\delta_N^j \quad \text{with} \quad \Delta\delta_N^j = k_N \mathbf{P}_N^j \\ \delta_T^j &= \delta_T^i + \Delta\delta_T^j \quad \text{with} \quad \Delta\delta_T^j = k_T \mathbf{P}_T^j \end{aligned} \quad (7)$$

where  $k_N$  and  $k_T$  denote the interface compliance coefficients along normal and tangential directions. Consequently in the global coordinate system one has

$$\delta_{ji}^j = \delta_{ij}^i + \mathbf{K}_{ij} \mathbf{P}_{ij}^i \quad i=1, \dots, M-1; \quad j=i+1, \dots, M \quad (8)$$

In the Eq. (8)  $\mathbf{K}_{ij}$  is a square matrix defined as

$$\mathbf{K}_{ij} = \begin{bmatrix} \cdot & & & \\ & \cdot & & \\ & & \alpha^T \mathbf{k} \alpha & \\ & & & \cdot & \\ & & & & \cdot & \\ & & & & & \cdot & \\ & & & & & & \cdot & \end{bmatrix} \quad (9)$$

where  $\mathbf{k}$  is the 2x2 diagonal matrix containing the interface compliance coefficients  $k_N$  and  $k_T$  and  $\alpha$  is the transformation matrix from local to global reference at the considered interface node. The modeling of the displacement jump at the interface does not require auxiliary interface elements since the elastic constants, characterizing the elastic behavior of the adhesive between two different layers, enter the definition of matrices  $\mathbf{H}$  and  $\mathbf{G}$ . In fact, for imperfect bonding Eq. (4) still holds with the following convention used for  $j < i$

$$\begin{aligned} \delta_{ij}^i &= \delta_{ji}^j & \mathbf{P}_{ij}^i &= \mathbf{P}_{ji}^j \\ \mathbf{H}_{ij}^i &= \mathbf{H}_{ji}^j & \mathbf{G}_{ij}^i &= -\mathbf{G}_{ji}^j + \mathbf{K}_{ij} \mathbf{H}_{ji}^j \end{aligned} \quad (10)$$

while in the case of perfect bonding

$$\begin{aligned} \delta_{ij}^i &= \delta_{ji}^j & \mathbf{P}_{ij}^i &= \mathbf{P}_{ji}^j \\ \mathbf{H}_{ij}^i &= \mathbf{H}_{ji}^j & \mathbf{G}_{ij}^i &= -\mathbf{G}_{ji}^j \end{aligned} \quad (11)$$

The system of Eq. (4) and the interface conditions provides a set of relationships, which, together with the external boundary conditions on the external boundaries, allows to obtain the mechanical response of each subdomain. An iterative procedure need to be used to avoid overlap between interface coincident nodes. The algorithm employed in the present work detects the contact conditions by checking the sign of the normal component of the displacement jump at the interface. In the case of detected contact the compliance constant  $k_N$  is set to zero.

**Numerical Results.** The first application refers to a three ply laminate subjected to cylindrical bending. The geometry, the boundary conditions as well the load imposed refer to the Pagano's problem [14], solved through three-dimensional elasticity analysis. The stacking sequence of the laminate is  $[0^\circ/90^\circ/0^\circ]$  while each ply has a thickness  $h/3$ , as shown in Fig.3. The plate is simply supported at both ends and a sinusoid load  $q=q_0 \sin(\pi x/l)$  is applied on the top surface. The material constants employed are listed in Table 1. The case of interface perfect bonding conditions, obtained by setting to zero the compliance interface coefficients  $k_N$  and  $k_T$ , was analyzed to compare the present results with those of reference [14]. The imperfect bonding conditions are also considered by setting  $k_N = 10^{-11} \text{ in/psi}$  and  $k_T = Rh/E_2$ , with a relaxation parameter  $R$  fixed to 0.6 in order to compare the results with those obtained by Bui et al. [5]. The vertical displacements, computed at the point of coordinate  $x_1=l/2$  and  $x_2=0$  and normalized according to  $w_n = 100E_2 h^3 w(l/2,0)/q_0 l^4$ , are plotted in Fig.4. The comparison shows good agreement for both perfect and weak bonding conditions. The two ply laminate shown in Fig. 5 was analyzed and the resulting through-

thickness  $\sigma_{22}$  stress distributions along the middle line of the laminate have been compared with those obtained from Liu et al. [3]. Two stacking sequences and different bonding conditions have been considered and the obtained results show good agreement with those found in the literature (Fig.6).

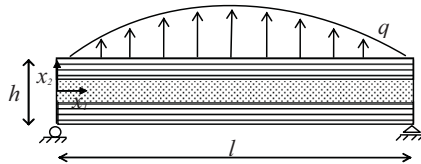


Fig.3 Three plies laminate under cylindrical bending.

Young modulus	Shear modulus	Poisson ratio
$E_1=25 \times 10^6$ psi	$G_{12}=0.5 \times 10^6$ psi	$\nu_{12}=0.25$
$E_2=1 \times 10^6$ psi	$G_{23}=0.2 \times 10^6$ psi	$\nu_{23}=0.25$

Table 1 Material constants.

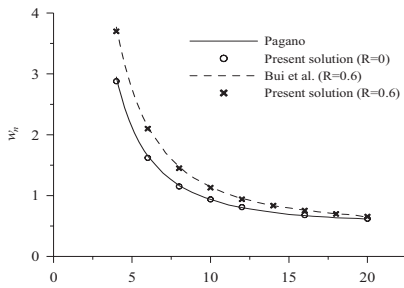


Fig. 4 Vertical displacements vs. slender ratio.

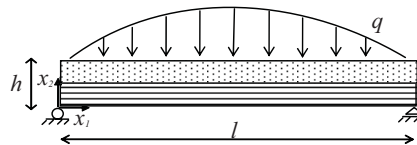


Fig. 5 Two plies laminate in cylindrical bending.

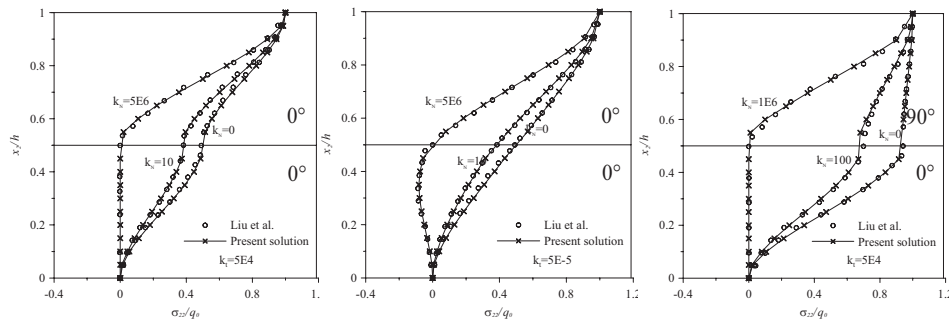


Fig. 6 Through thickness  $\sigma_{22}$  stress distribution.

Finally results for the peel stresses arising in the symmetric cross-ply laminate shown in Fig. 7 are presented. Analyses were performed for both perfect bonded interface ( $k_N=k_T=0$ ) and weak interface obtained by setting  $k_N=1.86 \times 10^7$  in/psi and  $k_T=1.6 \times 10^6$  in/psi. The results are compared to those obtained by a multidomain boundary element analysis in which the interface layer is modeled as an auxiliary isotropic domain with  $E=2.4 \times 10^5$  psi and  $\nu=0.33$ . The peel stresses plotted in Fig. 8 evidence good agreement between the results obtained with the present spring model and the multidomain BEM analysis. It is worth noting that the interface bonding condition strongly affect the peel stresses in laminates. Comparing the maximum peel stresses obtained with perfect and weak interface a reduction of 35% is evidenced.

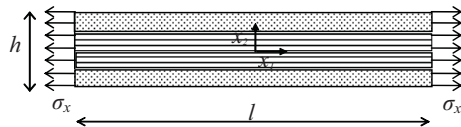


Fig. 7 Four plies laminate under traction.

Young modulus	Shear modulus	Poisson ratio
$E_1=25 \times 10^6$ psi	$G_{12}=0.5 \times 10^6$ psi	$\nu_{12}=0.25$
$E_2=1 \times 10^6$ psi	$G_{23}=0.2 \times 10^6$ psi	$\nu_{23}=0.25$

Table 2 Material constants.

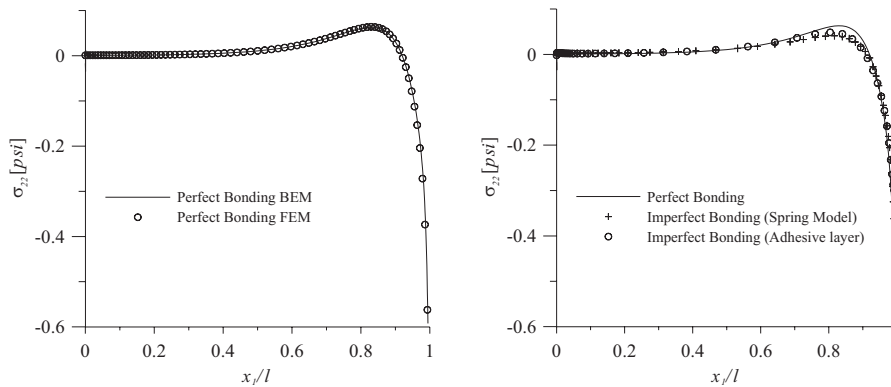


Fig. 8 Peel stress distributions

**Conclusions.** A multidomain boundary integral formulation for the analysis of composite laminates with imperfect interlaminar interfaces has been presented. The displacement discontinuity has been considered through a spring model and no auxiliary elements are needed to model the imperfect interface since the spring coefficients, characterizing the different bonding interface conditions, are directly taken into account inside the assembled influence matrices. The analysis of some typical configurations has been carried out and the results have shown the effectiveness of the model as well as the effects of a weak interface on the behavior of the interlaminar stresses. Future developments are related to the use of nonlinear interface models within the implemented approach in order to exploit the method features in describing laminate interface behavior.

**References**

- [1] A.K. Noor *Structure Technology for Future Aerospace Systems*, American Institute of Aeronautics and Astronautics (2000).
- [2] R.M. Jones *Mechanics of Composite Materials*, Hemisphere New York, (1975).
- [3] D. Liu, L. Xu and X. Lu *International Journal for Numerical Methods in Engineering*, **37**, 2819-2839 (1994).
- [4] Z. Cheng, A.K. Jemak and F.W. Williams *Journal of Applied Mechanics*, **63**, 1019-1026 (1996).
- [5] V.Q. Bui, E. Marechal and H. Nguyen-Dang *Composites Science and Technology*, **59**, 2269-2277 (1999).
- [6] N.M. Newmark, C.P. Seiss and I.M. Viest *Proc. Society for Experimental Stress Analysis*, **9** (1), 73-79 (1951).
- [7] X. Lu and D. Liu *AIAA Journal*, **30**, 1063-1073 (1992).
- [8] J. Aboudi and M. Paley *Composite Science and Technology*, **28**, 103-128 (1987).
- [9] J.D. Achenbach and H. Zhu *Journal of the Mechanics and Physics of Solids*, **37**, 381-393 (1989).

- [10] I. Jasiuk and Y. Tong *Mechanics of Composite Materials and Structures (Proceedings of the third Joint ASCE/ASME Conference)*, ASME, AMD-Vol. 100, 49-54 (1989).
- [11] G. Davi and A. Milazzo *International Journal of Solids and Structures*, **38**, 7065-7078 (2001).
- [12] G. Davi and A. Milazzo *Journal of Applied Mechanics* 64 (4) (1997), 877-884.
- [13] P.K. Banerjee and R. Butterfield *Boundary Element Methods in Engineering Science*, McGraw-Hill, Maidenhead, (1981).
- [14] N.J. Pagano *Journal of Composite Material*, **3**, 398-411 (1969).

## A coupled DRM-GA algorithm for the localization of skin tumours

P W Partridge<sup>1</sup> and L C Wrobel<sup>2</sup>

<sup>1</sup> Dept. Eng. Civil e Ambiental, Universidade de Brasilia, 70910-900 Brasilia DF, Brazil.

Email: paulp@unb.br.

<sup>2</sup> School of Engineering and Design, Brunel University, Uxbridge, Middlesex UB8 3PH, UK.

Email: luiz.wrobel@brunel.ac.uk

**Keywords** Dual Reciprocity, Boundary Elements, Genetic Algorithm, Bioheat Equation, Inverse Analysis, Thermal Analysis, Tumours

**Abstract** In this paper, the Dual Reciprocity Method (DRM) is coupled to a Genetic Algorithm (GA) in an inverse procedure through which the size and location of a skin tumour may be obtained from temperature measurements at the skin surface. The GA is an evolutionary process which does not require the calculation of sensitivities, search directions or the definition of initial guesses. The DRM in this case requires no internal nodes. Results are presented for tumours of different sizes and positions in relation to the skin surface.

### Introduction

It is well known that the body surface temperature is controlled by blood circulation, local metabolism and heat transfer between the skin and the environment [1]. It is also known that several types of tumours, *e.g.* skin or breast, can lead to an increase in local blood flow, and thus to an increase in the local temperature [2]. On the other hand, thrombosis or vascular sclerosis decreases the blood flowing to the skin, resulting in lower skin temperatures [2].

Amongst various types of non-invasive techniques for tumour detection, such as ultra-sound or MRI, thermal methods appear to be economic and safe. Non-invasive diagnostics can be performed from skin surface temperature measurements using inverse analysis techniques based on Pennes' bioheat equation, which has a known fundamental solution previously implemented in the BEM context by Chan [3]. However, herein a numerical technique is proposed based on the Dual Reciprocity Method (DRM), which has already been used for the direct solution of the bioheat equation by Liu and co-authors [1-2, 4-7]. In the present work the tumour, the location and size of which are initially unknown, is modelled as a subregion, and in addition to the nodes used to model the boundary of the tumour, no other internal points are required.

Previous work on inverse bioheat analysis has been carried out by Ren *et al.* [8], who applied the BEM to identify heat sources in biological bodies based on the simultaneous measurement of temperature and heat flux at the skin surface, and by Majchrzak and Paruch [9], who estimated the thermophysical parameters of the tumour using a least-squares algorithm based on sensitivity coefficients.

This paper makes use of a Genetic Algorithm (GA) [10,11] in an inverse BEM formulation for determining the position and size of a tumour from skin temperature measurements. The method is of an evolutionary type, requiring no initial guess about the position of the tumour and no calculations of sensitivities or search directions. The method starts from a series of binary strings, each of which contains a possible solution to the problem (position of centre and size of tumour, considered to be rectangular in shape). The initial population of strings (the chromosomes) is improved upon iteratively using a process of crossover and mutation, which numerically imitate the natural selection procedure. It should be noted that the use of domain methods such as finite elements for the solution of the bioheat equation in this way would require the generation of a mesh for each chromosome considered in the solution. The DRM, on the other hand, does not require any remeshing, the information on the size and position of the centre of the tumour contained in each chromosome being sufficient to determine the position of the elements of the subregion in each case. A simple GA as described in the literature [12] is generally adequate.

Early applications of the DRM for general engineering problems mainly used the simple linear radial basis approximation function  $r$ , but later many other alternative functions were introduced. Here, the cubic radial basis function  $r^3$  is employed with linear augmentation [13,14].

The DRM formulation for the bioheat equation is considered in the next section. This is followed by some results of direct analyses which illustrate the use of the DRM and show the relationship between tumour position and size and temperature distribution on the skin surface. Then, the inverse geometric problem is described and the results of some inverse analyses obtained with GA are presented, for several tumour sizes and positions. The advantages and limitations of the proposed technique are also discussed.

#### Application of the Dual Reciprocity Method to the bioheat equation

The bioheat or Pennes equation can be written in the following form [1-7],

$$\rho c \frac{\partial T}{\partial t} = \nabla^2 T + \frac{\omega_b \rho_b c_b}{k} (T_a - T) + \frac{Q}{k} \quad (1)$$

where  $\rho$ ,  $c$  and  $k$  denote density, specific heat and thermal conductivity of tissue;  $\rho_b$ ,  $c_b$  are density and specific heat of blood,  $\omega_b$  is the blood perfusion rate,  $T_a$  is the arterial blood temperature and  $Q$  is the spatial heating. Eq. (1) is subject to the usual boundary conditions for thermal problems, (i) temperature prescribed  $T = \bar{T}$ ; (ii) heat flux prescribed,  $q = \bar{q}$ ; Eq. (1) can be written, in steady state form, as

$$\nabla^2 T = -\frac{\omega_b \rho_b c_b}{k} (T_a - T) - \frac{Q}{k} = b \quad (2)$$

Eq. (2) is a Poisson-type equation with two inhomogeneous terms, the first of which is dependent on the problem variable  $T$ , the other term being a function of space only. This equation is solved using the DRM [15] in which the fundamental solution to the Laplace equation,  $u^* = 1/2\pi \log(1/r)$ , is employed to treat the term on the left-hand side of (2) and the inhomogeneous terms are taken to the boundary, leading to the system of equations:

$$HT - Gq = (H\hat{U} - G\hat{Q})\alpha, \quad (3)$$

where the symbols have their usual meaning [15]. As the term  $b$  is a function of the problem unknowns, Eq. (3) is written as

$$HT - Gq = (H\hat{U} - G\hat{Q})F^{-1}b \quad (4)$$

where matrix  $F$  is calculated from the definition of the approximating functions. Calling  $S = (H\hat{U} - G\hat{Q})F^{-1}$ , and defining  $c_1 = \omega_b \rho_b c_b / k$  and  $c_2 = -(\omega_b \rho_b c_b T_a - Q)/k$ , then Eq. (4) can be written

$$HT - Gq = c_1 ST + c_2 S \quad (5)$$

The previous equation may be rewritten as

$$(H - c_1 S)T - Gq = c_2 S \quad (6)$$

For a direct, well-posed problem for which the entire boundary  $\Gamma$  is properly defined, and one boundary condition is defined for each point on the boundary, one may apply boundary conditions to Eq. (6) in the usual way to produce

$$Ax = y + d \quad (7)$$

Eq. (7) may be solved for unknown values at boundary and internal points, if these are defined.

### Direct results for different positions and sizes of tumours

Considering Fig. 1, the external boundary, ABCD or  $\Gamma_2$ , is a vertical section through the skin tissue, the part AD being at the skin surface while the opposite boundary BC is considered to be an internal boundary maintained at body temperature,  $T = 37^\circ\text{C}$ . The boundaries AB and CD are truncation boundaries, due to considering a section; at these boundaries, the condition  $q = 0$  is considered. If the boundary AD is assumed to have a zero flux boundary condition, this is equivalent to thermal insulation, for instance a bandage. The internal boundary or  $\Gamma_1$  is considered to divide the domain into two parts,  $\Omega_2$  the healthy tissue and  $\Omega_1$  which represents the tumour. On the boundary  $\Gamma_1$  the usual compatibility and equilibrium conditions apply, *i.e.*  $T_1 = T_2$  and  $q_1 = -q_2$ . The parameters  $c_1$  and  $c_2$  in Eq. (5) will be different for each subregion.

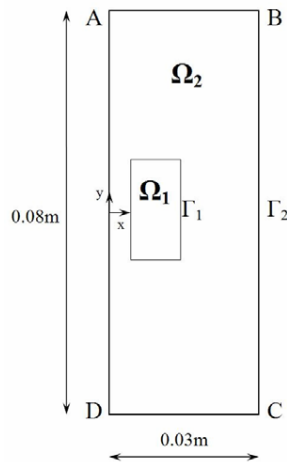


Fig. 1. Tumour within a matrix of healthy tissue

The values of the parameters necessary to calculate  $c_1$  and  $c_2$  are taken from [2]:  $\rho_b = 1000\text{kg/m}^3$ ,  $c_b = 4000\text{J/(kg }^\circ\text{C)}$ ,  $k = 0.5\text{ W/(m }^\circ\text{C)}$ . In addition,  $\omega_b = 0.0005\text{ ml}_b/\text{ml}_t/\text{s}$  and  $Q = 420\text{ J/(m}^3\text{ s)}$  for healthy tissue, while the respective values for the tumour are  $\omega_b = 0.002\text{ ml}_b/\text{ml}_t/\text{s}$  and  $Q = 4200\text{ J/(m}^3\text{ s)}$  [2], with the subscripts  $b$  and  $t$  indicating blood and tissue, respectively. The arterial blood temperature  $T_a$  is  $37^\circ\text{C}$ .

Considering the geometry given in Fig. 1, in which the skin depth is considered to be  $0.03\text{m}$  and the length of the cross-section considered is  $0.08\text{m}$ , a discretisation is adopted with 56 linear boundary elements for  $\Gamma_2$  and 16 linear elements for  $\Gamma_1$ . Taking both  $\Omega_1$  and  $\Omega_2$  to be healthy tissue, and assuming the boundary condition along AD to be  $q = 0$ , then one obtains a constant temperature of  $37.14^\circ\text{C}$  at the skin surface. This result was checked using the BEM with internal cells instead of DRM and also using finite elements (384 triangular elements), no internal nodes were necessary with the DRM other than those defining  $\Gamma_1$ .

In addition to considering different positions of the tumour, different sizes may also be considered. In what follows the tumour denoted A is of size  $0.005\text{m} \times 0.01\text{m}$ , *i.e.* one half the size considered in the previous case. The centre is at position  $(0.005, 0.020)$ . The tumour denoted B is of the same size as A, but centred at position  $(0.02, 0.02)$ . The tumour denoted C is of size  $0.0175\text{m} \times 0.035\text{m}$  ( $1\frac{3}{4}$  the size of the original tumour) and is centred at position  $(0.01625, 0)$ . Results for the surface temperature variation for all of these cases are given in Fig. 2.

Note that tumours A and B are of the same size, but as A is near the surface, a significant peak appears in the curve. Curve B is nearly flat while tumour C, whilst far from the surface, has a bigger size, thus also giving rise to a significant peak in the temperature distribution.

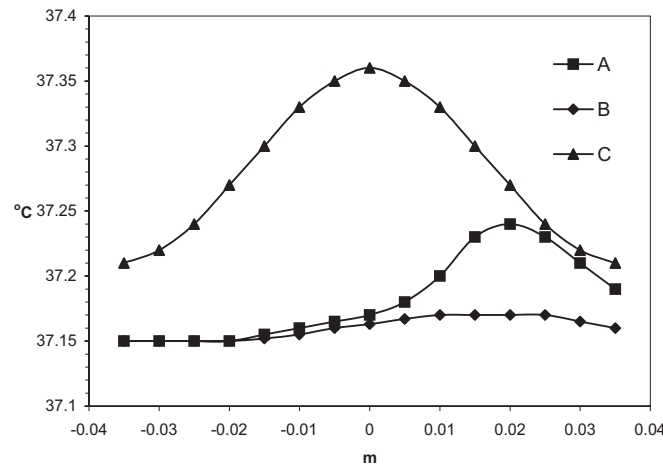


Fig. 2. Variation of skin surface temperatures for the tumours A-C

#### Procedure for the determination of the size and position of tumours from skin surface temperatures using Genetic Algorithm

Considering a tumour of size  $0.01 \times 0.02\text{m}$ , given the finite size, this can only be located with its center  $0.005\text{m}$  from the edges AD or BC and  $0.01\text{m}$  from the edges AB and DC. Thus the area in which the center may be located is smaller than ABCD and is of size  $0.02 \times 0.06\text{m}$  (see fig. 1). Each chromosome has three alleles. The first one contains the  $x$  coordinate of the center of the tumour. Considering 5 binary digits as used here, 00000 corresponds to the left margin AD and 11111 to the right margin BC. Given  $2^5 - 1 = 31$  and dividing  $0.02/31$  one obtains  $0.00064516$  which is the distance between two successive values of the allele. If the allele is for instance 01011=11 in decimal, the position of the  $x$  coordinate of the center is thus  $0.00064516 \times 11 = 0.00709676 + 0.005$  due to the finite size mentioned above, giving  $0.01209676$ . Using a similar reasoning in the  $y$  direction and considering 7 binary digits for this allele one obtains  $0.00047244$  as the distance between two successive positions, where the value  $0.04$  was added due to the finite size effect. In the general case, the position of the centre is given by the formulas

$$\begin{aligned} x_c &= a_x \times A_1 + b_x \\ y_c &= a_y \times A_2 + b_y \end{aligned} \quad (8)$$

where  $A_1$  and  $A_2$  are the values of the first two alleles in base 10. Since the values of  $a_x, a_y, b_x, b_y$  are given above for a tumour of size 1, the values for tumours of other sizes are easily calculated. The third allele refers to the size of the tumour from  $1/4$  of the size of the basic tumour shown in fig. 1 to twice that size in steps of  $0.25$ . 3 binary digits are used for this allele. 000 is a tumour of size  $1/4$ , 111 is one of size 2. The basic tumour is thus represented by the binary digits 011. Summing the sizes of the three alleles one gets 15 bits as the size of the chromosome. The population size was fixed at 20 following guidelines given in [17].

After establishing an initial population, the position and size of the tumour for each chromosome is obtained as considered above from (8), and results for the temperature distribution at nodes along the part AD of the  $\Gamma_2$  boundary (Fig. 1) are calculated using the DRM algorithm. For the DRM discretisation, the elements on the boundary  $\Gamma_2$  (Fig. 1) are fixed and those on  $\Gamma_1$  are given for a size 1 tumour centred at position (0.01, 0). Therefore, it is only necessary to multiply by the size and sum to the coordinates the values due to finite size effect as explained above to produce the geometry of the tumour for each chromosome.

The objective of the algorithm is to minimise the value of the sum of the squares of the differences between the temperatures calculated at nodes on side AD (Fig. 1) and the measured values. The chromosomes are ordered according to the value of the sum of the squares, with the smallest value first, the position in this new order being referred to as the fitness. Individuals are selected for crossover using the roulette wheel method described by Goldberg [10], the fitter individuals having the greater probability of selection. Two point crossover and mutation with a probability of 1% is carried out in the GA. A process of elitism is employed by which the best individual from one generation passes automatically to the next, in order to ensure that the best solution is not lost [10]. The stopping criterion considered is that 80% of individuals must converge to the same value.

#### **Some results for the identification of the position and size of tumours**

Considering the same geometry as in the previous examples of direct analyses, shown in Fig 1 in which a section of tissue of dimensions  $0.03\text{m} \times 0.08\text{m}$  was considered, and using their results as input data for the inverse analysis, the temperature values for part AD of  $\Gamma_2$  can be calculated. These values are compared with the values calculated for each size and position of tumour indicated by the chromosomes in the GA, and the sum of the squares of the differences minimised. The boundaries  $\Gamma_1$  and  $\Gamma_2$  are discretised with 16 and 56 linear boundary elements, respectively.

Considering as input data for the temperature distribution at the skin surface the values given in Fig. 2A, the results produced by the program were tumour centre at position (0.00653, 0.01957) and size 0.5. Results converged in 75 generations. The data used to generate the results given in Fig. 2A were centre (0.005, 0.02) and size 0.5. Considering Fig. 2C, the results obtained by the inverse analysis were tumour centre at position (0.01681, -0.00088) and size 1.75. The data used to generate curve 2C were centre (0.016, 0) and size 1.75.

The inverse analysis did not converge for the data in Fig. 2B. The skin surface temperature variation produced by this tumour (curve 2B) was nearly flat. The physical interpretation of this temperature variation is that the tumour is too small and too far from the skin surface to produce any significant skin temperature variation, therefore it cannot be detected by using the current GA algorithm.

#### **Conclusions**

In the above, a numerical technique based on the dual reciprocity boundary element method coupled with a genetic algorithm was used in an inverse procedure for obtaining the position and size of tumours from temperature data on the skin surface. The procedure has the advantage of not needing to calculate derivatives or sensitivities, and does not require an initial estimate of the position of the tumour. It is seen, however, that tumours that are very small or deeply located produce only a small perturbation of the skin temperature variation, and thus cannot be detected in this way. In the case of the DRM, it is seen that internal nodes are not necessary.

The proposed technique can be directly extended to more realistic three-dimensional inverse analysis estimations, at an increased computational cost. It can also be extended to deal with temperature-dependent blood perfusion coefficients, which are particularly relevant when considering hyperthermia cancer therapy [18,19].

### Acknowledgement

The first author gratefully acknowledges the support of the Brazilian agency CAPES in funding this work.

### References

- [1] Z-S. Deng and J. Liu, *Computers in Biology and Medicine*, **34**, 495-521 (2004).
- [2] J. Liu and L. S. Xu, *International Journal of Heat and Mass Transfer*, **43**, 2827-2839 (2000).
- [3] C. L. Chan, *Transactions of the ASME, Journal of Biomechanical Engineering*, **114**, 358-365 (1992).
- [4] Z-S. Deng and J. Liu, *Medical Engineering & Physics*, **22**, 693-702 (2000).
- [5] J. Liu and L. X. Xu, *IEEE Transactions on Biomedical Engineering*, **46**, 1037-1043 (1999).
- [6] W-Q. Lu, J. Liu and Y Zeng, *Engineering Analysis with Boundary Elements*, **22**, 167-174 (1998).
- [7] Z-S. Deng and J. Liu, *Engineering Analysis with Boundary Elements*, **28**, 97-108 (2004).
- [8] Z. P. Ren, J. Liu and C. C. Wang, *Journal of Thermal Science*, **4**, 117-124 (1995).
- [9] E. Majchrzak and M.Paruch, *Proceedings ECCOMAS 2004*, (Eds) P. Neittaanmaki, T. Rossi, K. Majava and O. Pironneau, 1-14 (2004).
- [10] D.E. Goldberg, *Genetic Algorithms in Search, Optimization and Machine Learning*, Addison Wesley, (1989).
- [11] D. E. Goldberg, K Zakrewsky, B. Sutton, R. Gadiant, C. Chong, P. Galego, B. Miller, and E. Cantu-Paz E, *Genetic Algorithms: A bibliography* (1999).
- [12] L. C. L Castro and P. W. Partridge, *Latin American Journal of Solids and Structures*, **3**, 107-123 (2006).
- [13] M. A. Golberg and C. S. Chen, *Boundary Element Communications*, **5**, 57-61 (1994).
- [14] T. R. Bridges and L. C. Wrobel, *Communications in Numerical Methods in Engineering*, **12**, 209-220 (1996).
- [15] P. W. Partridge, L. C. Wrobel and C. A. Brebbia, *The Dual Reciprocity Boundary Element Method*, Elsevier (1992).
- [16] D. Nardini D and C. A. Brebbia, *Applied Mathematical Modelling*, **7**, 157-162 (1983).
- [17] N. Kahn *Population sizing in genetic and evolutionary algorithms*, University of Illinois at Urbana Champaign (2002).
- [18] D. T. Tompkins, R. Vanderby, S. A. Klein, W. A. Beckman, R. A. Steeves, D. M. Frye, and B. R. Paliwal, *International Journal of Hyperthermia*, **10**, 517-536 (1994).
- [19] J. Lang, B. Erdmann and M. Seebass, *IEEE Transactions on Biomedical Engineering*, **46**, 1129-1138 (1999).

## Direct and Iterative Strategies to Incorporate Rigid Body Restrictions into a Direct and Indirect Version of the Boundary Element Method

L H Thomazo<sup>1)</sup>, E Mesquita<sup>1\*)</sup>, E Romanini<sup>2)</sup>

1) Department of Computational Mechanics – DMC/FEM,  
State University at Campinas - UNICAMP  
C.P. 6122  
CEP 13083-970 Campinas, Brazil

\*) Corresponding author e-mail: [euclides@fem.unicamp.br](mailto:euclides@fem.unicamp.br)

2) Department of Exact Sciences, CEUL- UFMS, Brazil

**Keywords:** Direct and Indirect Boundary Element Methods, Rigid Body restrictions, Direct and iterative procedures

**Abstract.** In this article five strategies to incorporate rigid body restrictions into Direct (DBEM) and Indirect (IBEM) Boundary Element formulations are described. Four direct strategies and one iterative scheme to impose rigid body kinematic compatibility conditions and equilibrium equations on the BE mesh are addressed. The direct methods include a) the simple expansion of the DBEM system to include the rigid body restrictions, b) the condensation of the system degrees of freedom at the DBEM-rigid body interface by means of a set of matrices transformations, c) the use of the pseudo-inverse of the equilibrium relations in order to reduce the manipulation of the DBEM system matrices and d) a direct scheme to introduce rigid bodies into the IBEM. Alternatively, an iterative scheme to fulfill the required equilibrium and kinematic restrictions within the IBEM is presented. Each formulation has advantages and drawbacks, regarding the size of the final equation system, number of required operations as well as resulting accuracy. The aim of the article is to describe and compare the mentioned strategies based on a dynamic soil structure interaction example. The soil is modeled by the BEM as an unbounded half-space interacting with a rigid structure. Computational effort and results accuracy will be addressed.

### Introduction

The problem to be addressed is the incorporation of the rigid body kinematic compatibility relation and equilibrium conditions within both the direct (DBEM) and the indirect (IBEM) version of the Boundary Element Method. Four direct and one iterative strategies are presented.

### The Boundary Element Method

Consider a boundary  $\Gamma = \Gamma_s \cup \Gamma_f$ , as shown in Fig.1. The matrix equations for the Direct version of the BEM (DBEM) may be written as [1]:

$$\begin{bmatrix} [H_{ss}] & [H_{sf}] \\ [H_{fs}] & [H_{ff}] \end{bmatrix} \begin{Bmatrix} u_s \\ u_f \end{Bmatrix} = \begin{bmatrix} [G_{ss}] & [G_{sf}] \\ [G_{fs}] & [G_{ff}] \end{bmatrix} \begin{Bmatrix} t_s \\ t_f \end{Bmatrix} \quad (1)$$

On the first boundary region  $\Gamma_s$  displacements and tractions, respectively,  $u_s$  and  $t_s$  are prescribed. The second boundary region  $\Gamma_f$  is the interface between the BE mesh and the rigid body. On this interface  $\Gamma_f$  the rigid body kinematic compatibility and equilibrium equations are prescribed, involving the displacements  $u_f$  and tractions  $t_f$ , respectively (see figure 1).

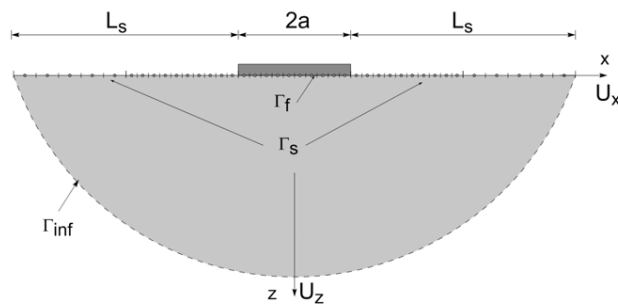


Figure 1: Rigid surface foundation interacting with a half-space.

#### The Indirect Boundary Element Method.

The indirect version of the BEM (IBEM) leads, analogously, to the following set of system matrices [2]:

$$\begin{bmatrix} H_{ss}^I & H_{sf}^I \\ H_{fs}^I & H_{ff}^I \end{bmatrix} \begin{Bmatrix} q_s \\ q_f \end{Bmatrix} = \begin{Bmatrix} u_s \\ u_f \end{Bmatrix} \quad (2)$$

$$\begin{bmatrix} G_{ss}^I & G_{sf}^I \\ G_{fs}^I & G_{ff}^I \end{bmatrix} \begin{Bmatrix} q_s \\ q_f \end{Bmatrix} = \begin{Bmatrix} t_s \\ t_f \end{Bmatrix} \quad (3)$$

In equations (2) and (3) the fictitious tractions on the boundary  $\Gamma = \Gamma_s \cup \Gamma_f$ , are designated by  $\{q\}$ . These equations may be given the format of the DBEM at the cost of two matrix inversions:

$$\begin{bmatrix} H_{ss}^I & H_{sf}^I \\ H_{fs}^I & H_{ff}^I \end{bmatrix}^{-1} \begin{Bmatrix} u_s \\ u_f \end{Bmatrix} = \begin{bmatrix} G_{ss}^I & G_{sf}^I \\ G_{fs}^I & G_{ff}^I \end{bmatrix}^{-1} \begin{Bmatrix} t_s \\ t_f \end{Bmatrix} \quad (4)$$

#### Rigid body restrictions.

At the interface  $\Gamma_f$ , placed between the BE mesh and the rigid body (RB), kinematic restrictions relating displacements at the BE nodes  $u_j(x, z)$  ( $j=x, z$ ) and the RB degrees of freedom (DOF)  $\{u_{ref}\}$ :

$$\{u_f\} = [CC]\{u_{ref}\} \quad (5)$$

Equilibrium must also be imposed between the vector of external forces applied at the rigid body  $\{F_{ext}\}$  and the actual tractions  $\{t_f\}$  at the interface  $\Gamma_f$ :

$$\{F_{ext}\} = [EQ]\{t_f\} \quad (6)$$

**Strategies for inclusion of Rigid Bodies**

The inclusion of the rigid body within the realm of the BEM may be summarized as the task of incorporating the kinematic restriction relation (5) and the equilibrium condition (6) into the BE matrices (1) or (2) and (3). It is assumed, for simplicity, that the prescribed boundary conditions on  $\Gamma_s$  are the external load vector  $\{F_{ext}\}$  and the traction vector  $\{t_s\}$ . The unknown quantities are the interface tractions  $\{t_f\}$ , the rigid body degrees of freedom  $\{u_{ref}\}$  and the displacements  $\{u_s\}$ .

**I) The traditional expansion method (DBEM\_EXP).** The first methodology consists of incorporating the rigid body restrictions in the DBEM-like relations (1) or (4). The inclusion of other boundary conditions is rather straight forward, resulting [3,4]:

$$\begin{bmatrix} [H_{ss}] & -[G_{sf}] & [H_{sf}][CC] \\ [H_{fs}] & -[G_{ff}] & [H_{ff}][CC] \\ [0] & [EQ] & [0] \end{bmatrix} \begin{Bmatrix} u_s \\ t_f \\ u_{ref} \end{Bmatrix} = \begin{Bmatrix} [G_{sf}] \\ [G_{ff}] \\ \{F_{ext}\} \end{Bmatrix} \begin{Bmatrix} t_s \end{Bmatrix} \quad (7)$$

In this formulation the original BE system is expanded by the number of the rigid body degrees of freedom. The original dimension of the original BE system is  $(2 \times 2n) \times (2 \times 2n)$  with  $n$  being the BE mesh degrees of freedom. The dimension of the matrices in (7) are  $(2 \times 2n + 3) \times (2 \times 2n + 3)$ . In the present case the plane rigid body motion with 3DOFs is considered. One advantage of this formulation, for the DBEM, is that it requires no matrix inversion. This formulation may also be applied to the IBEM, provided the two matrix inversions indicated in equation (4) are performed.

**II) The traditional reduction method (DBEM\_RED).** This strategy reduces the size of the final equation system. The starting point is to define a stiffness-like matrix  $[K]$ :

$$\begin{bmatrix} [G_{ss}] & [G_{sf}] \\ [G_{fs}] & [G_{ff}] \end{bmatrix}^{-1} \begin{bmatrix} [H_{ss}] & [H_{sf}] \\ [H_{fs}] & [H_{ff}] \end{bmatrix} \begin{Bmatrix} u_s \\ u_f \end{Bmatrix} = \begin{bmatrix} [K_{ss}] & [K_{sf}] \\ [K_{fs}] & [K_{ff}] \end{bmatrix} \begin{Bmatrix} u_s \\ u_f \end{Bmatrix} = \begin{Bmatrix} t_s \\ t_f \end{Bmatrix} \quad (8)$$

The incorporation of the RB condition leads to [4]:

$$\begin{bmatrix} [K_{ss}] & [K_{sf}][CC] \\ [EQ][K_{fs}] & [EQ][K_{ff}][CC] \end{bmatrix} \begin{Bmatrix} u_s \\ u_{ref} \end{Bmatrix} = \begin{Bmatrix} t_s \\ \{F_{ext}\} \end{Bmatrix} \quad (9)$$

In equation (9) the dimension of the system is  $(2n+3) \times (2n+3)$ , which is almost half of the size of the previous formulation shown in (7). The price to be paid is the inversion of the  $[G]$  matrix.

**III) Pseudo inverse of the equilibrium relations (DBEM\_PSD).** The equilibrium and kinematic restrictions may be incorporated directly on the vectors of the displacements and tractions, using a formal inversion for an expanded matrix of containing the equilibrium relations [4]:

$$\begin{bmatrix} [H_{ss}] & [H_{sf}] \\ [H_{fs}] & [H_{ff}] \end{bmatrix} \begin{bmatrix} [1] & [0] \\ [0] & [CC] \end{bmatrix} \begin{Bmatrix} \{u_s\} \\ \{u_{ref}\} \end{Bmatrix} = \begin{bmatrix} [G_{ss}] & [G_{sf}] \\ [G_{fs}] & [G_{ff}] \end{bmatrix} \begin{bmatrix} [1] & [0] \\ [0] & [EQ] \end{bmatrix}^{-1} \begin{Bmatrix} \{t_s\} \\ \{F_{ext}\} \end{Bmatrix} \quad (10)$$

In this expression (10) no inversion of the system matrices  $[G]$  or  $[H]$  is necessary. Also, the resulting system is not square and a solution in the least square sense must be seek. The key issue is to determine a generalized inverse of the expanded equilibrium condition matrix shown in (10).

**IV) Direct incorporation of the rigid body conditions in the IBEM (IBEM\_RB).** The IBEM formulation is expanded to accommodate the solution of general mixed boundary value problems. The boundary  $\Gamma$  is divided into  $\Gamma = \Gamma_r \cup \Gamma_{su} \cup \Gamma_{st}$ . On  $\Gamma_{su}$  and  $\Gamma_{st}$  the displacements  $u_o$  and tractions  $t_o$  are prescribed, respectively. The inclusion of the RB conditions leads to the system [4]:

$$\begin{bmatrix} [A1] & [A2] \\ [B1] & [B2] \\ [C1] & [C2] \end{bmatrix} \begin{Bmatrix} \{q_{su}\} \\ \{q_{st}\} \\ \{u_{ref}\} \end{Bmatrix} = \begin{Bmatrix} \{t_o\} \\ \{u_o\} \\ \{F_{ext}\} \end{Bmatrix} \quad (11)$$

with

$$[A1] = \left[ \begin{bmatrix} [G'_{ssu}] & [G'_{sst}] \end{bmatrix} - [G'_{sf}] [H'_{ff}]^{-1} \begin{bmatrix} [H'_{fsu}] & [H'_{fst}] \end{bmatrix} \right] \quad (12)$$

$$[A2] = [G'_{sf}] [H'_{ff}]^{-1} [CC] \quad (13)$$

$$[B1] = \left[ \begin{bmatrix} [H'_{ssu}] & [H'_{sst}] \end{bmatrix} - [H'_{sf}] [H'_{ff}]^{-1} \begin{bmatrix} [H'_{fsu}] & [H'_{fst}] \end{bmatrix} \right] \quad (14)$$

$$[B2] = [H'_{sf}] [H'_{ff}]^{-1} [CC] \quad (15)$$

$$[C1] = [EQ] \left[ \begin{bmatrix} [G'_{fsu}] & [G'_{fst}] \end{bmatrix} - [G'_{ff}] [H'_{ff}]^{-1} \begin{bmatrix} [H'_{fsu}] & [H'_{fst}] \end{bmatrix} \right] \quad (16)$$

$$[C2] = [EQ] [G'_{ff}] [H'_{ff}]^{-1} [CC] \quad (17)$$

In this equation system the only necessary matrix inversion is related to the sub-matrix  $[H'_{ff}]$ , which presents the size of the BE interface degrees of freedom (DOF). It should also be noticed that there is a number of matrix operations to be performed to build the equation system (11). An account of the necessary operations will be provided at the end of this article. The size of the global system (11) is the same of the size presented in equation (7).

**V) An iterative scheme to incorporate the rigid body within the IBEM (IBEM\_IT).** It is also possible to write an iterative scheme to introduce the rigid body restrictions in the IBEM. The tractions  $\{t_s\}$  and the vector of external forces  $\{F_{ext}\}$  are given. The displacements  $\{u_f\}$  at the

interface  $\Gamma_f$  may be arbitrarily chosen at an initial iteration step ( $it=0$ ), for instance,  $\{u_f(it=0)\} = \{u_{f0}\} = \{0\}$ . Equations (2) and (3) can be rearranged to yield:

$$\begin{bmatrix} G_{ss}^I & G_{sf}^I \\ H_{fs}^I & H_{ff}^I \end{bmatrix} \begin{Bmatrix} q_s \\ q_f \end{Bmatrix} = \begin{Bmatrix} t_s \\ u_{f0} \end{Bmatrix} \quad (18)$$

The solution of equation (18) will furnish the fictitious tractions for the initial iteration

$$\begin{Bmatrix} q_s(it=0) \\ q_f(it=0) \end{Bmatrix} = \begin{Bmatrix} q_{s0} \\ q_{f0} \end{Bmatrix} \quad (19)$$

The fictitious tractions of the initial iteration  $\{q_{s0}\}$  in equation (19) may be substituted in equation in the third line of equation (11):

$$[EQ][G_{ff}^I][H_{ff}^I]^{-1}[CC]\{u_{ref}\} = \{F_{ext}\} - [EQ]\left[\left[G_{fs}^I\right] - \left[G_{ff}^I\right]\left[H_{ff}^I\right]^{-1}\left[H_{fs}^I\right]\right]\{q_{s0}\} \quad (20)$$

The solution of equation (20) will deliver the rigid body displacement  $\{u_{ref}\}$  for the initial iteration ( $it=0$ ):

$$\{u_{ref}(it=0)\} = \{u_{ref0}\} \quad (21)$$

Once  $\{u_{ref0}\}$  is known, the kinematic equation (5) allows the determination of the interface displacement vector:

$$\{u_{f0^*}\} = [CC]\{u_{ref0}\} \quad (22)$$

The calculated interface nodes displacement vector  $\{u_{f0^*}\}$  may be compared to the initial guess  $\{u_f(it=0)\} = \{u_{f0}\}$  and a displacement error  $\{u_{err0}\}$  can be computed:

$$\{u_{f0^*}\} - \{u_{f0}\} = \{u_{err0}\} \quad (23)$$

If the displacement error is smaller than a prescribed tolerance  $\{u_{tol}\}$ ,

$$\{u_{err0}\} \leq \{u_{tol}\} \quad (24)$$

the problem is solved. Otherwise a new start value for the interface displacement node vector is determined by the relation:

$$\{u_{f1}\} = (\beta)\{u_{f0^*}\} + (1-\beta)\{u_{f0}\} \quad (25)$$

and substituted back in equation (18) for the next iteration ( $it=1$ ). The process may iterate until condition (24) is fulfilled. The interesting point about this procedure is that the matrix elements

shown in equation (20) will only be built once. The remaining cost of the iterative process is related to solving the linear system (20) repeatedly. In this article  $\beta=0.5$ .

### Numerical Results

The strategies outlined above will be tested in a typical dynamic soil-structure interaction system of a rigid and massless surface foundation interacting with a half-space, figure 1. The foundation width, which corresponds to the boundary  $\Gamma_f$ , is  $2a=2\text{m}$  and the length of the discretized soil free surface is  $L_s=6a=6\text{m}$ . The soil-foundation interface ( $\Gamma_f$ ) is discretized with 12 constant elements. The remaining boundary  $\Gamma_s$  is discretized with 48 elements, distributed according to the rule furnished in table 1.

Surface segment	Number of elements
$0 \leq x \leq 1$ or $-1 \leq x \leq 0$	12
$1 \leq x \leq 3$ or $-3 \leq x \leq -1$	12
$3 \leq x \leq 5$ or $-5 \leq x \leq -3$	8
$5 \leq x \leq 7$ or $-7 \leq x \leq -5$	4

Table 1: Discretization data for the half-space surface

For this example, the total number of degrees of freedom is  $n=120$ . The number of DOFs at the soil free surface  $n_s=96$  and the soil foundation interface DOFs is given by  $n_f=24$ , with  $n=n_s+n_f$ .

**Quasi-static results.** Figure 2 shows the absolute value of the soil vertical displacement component  $u_z$  due to a unit external vertical load  $F_z=1[\text{N}]$ , applied at the rigid foundation for a very low value of the dimensionless frequency,  $A_0=0.005$ . The dimensionless frequency is  $A_0=\omega a/c_s$ , with  $\omega$  [rads/s] being the circular frequency,  $a$  [m] the foundation half-width and  $c_s$  [m/s] the shear velocity of the elastic continuum. The other parameters are the Poisson ration  $\nu=0.25$  and the shear modulus  $G=1$  [N/m<sup>2</sup>]. The rigid body kinematic restriction is clearly visible at the soil-rigid foundation interface. The results from the pseudo-inverse methodology presents a small deviation from all other results, which, in turn, coincide precisely.

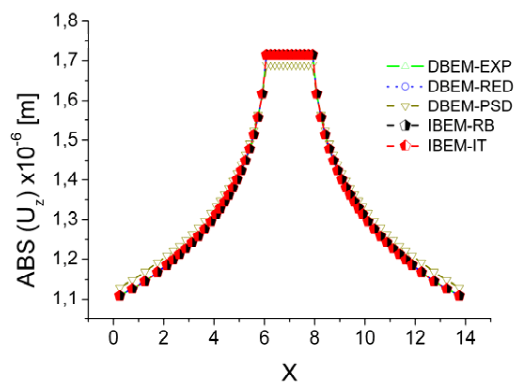


Figure 2: Vertical displacement  $u_z$  of the soil surface due to a vertical external load  $F_z$

**Dynamic results.** The absolute value of the vertical displacement of the rigid foundation  $u_v$ , as a function of the frequency  $A_0$  for the same vertical excitation  $F_z=1[N]$  is shown in figure 3. All methods deliver precisely the same solution. The only exception is the methodology based on the pseudo inverse (DBEM-PSD) which presents some deviations from the values determined by all others methods.

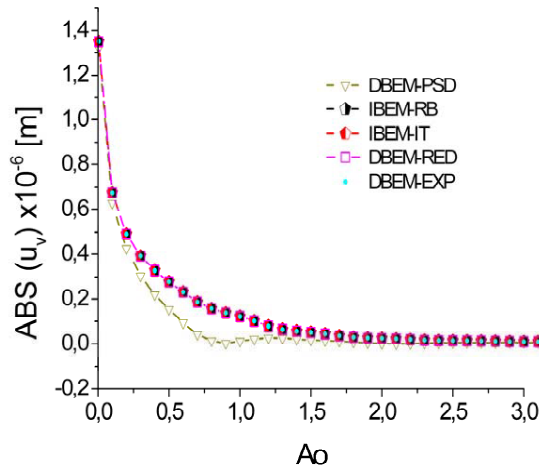


Figure 3: Rigid foundation dynamic vertical displacement  $u_v(A_0)$

**Computational effort.** Table 2 shows the computational effort in millions of floating point operations (MFlop) required to solve the numerical example according to each strategy rule described in the previous paragraphs. The numerical effort for the IBEM\_IT was calculated considering the number of 30 iterations. Table 3 shows the number of iteration required for the IBEM\_IT to achieve distinct precision levels  $\{u_{tol}\}$  according to the dimensionless frequency  $A_0$ . It can be seen that for higher frequencies  $A_0 > 1.0$  and tolerances in the range  $u_{tol} = 10^{-6}$ , the IBEM\_IT seems to be a competitive solution strategy.

Strategy	DBEM_EXP	DBEM_RED	DBEM_PSD	IBEM_RB	IBEM_IT(30)
MFlop	0.675	5.548	0.421	1.532	2.445

Table 2: Number of Floating operations  $\times 10^6$  for each strategy

Tol. $\{u_{tol}\}$ / Dim. Freq	$10^{-12}$	$10^{-10}$	$10^{-08}$	$10^{-06}$
$A_0=0.005$	45	38	31	24
$A_0=1.0$	39	33	26	20
$A_0=10.0$	36	30	23	16

Table 3: Iterations for the IBEM\_IT strategy for distinct frequencies and required precision

### Concluding Remarks

Five distinct solution strategies to incorporate rigid body restrictions on a BE mesh are briefly described. For a typical dynamic soil-structure interaction example, the size of the system matrix and the number of floating point operations for each strategy are addressed. An iterative scheme to incorporate the rigid body conditions within the indirect version of the BEM is devised.

Numerical results based on a soil-structure example indicate that for the DBEM based on pseudo inverse solution (PSD) strategy is the computationally most efficient alternative. But, as formulated, the DBEM\_PSD is not as accurate as the remaining strategies. For the IBEM the direct incorporation of the rigid body with inversion of a sub-system matrix  $[H_{ff}^I]$  seem to be the most efficient scheme. On the other hand, the iterative method seems to be a competitive strategy for relative higher frequencies and lower accuracy requirements. In the numerical example reported in this article, all solution strategies delivered the same numerical results for quasi-static and dynamic solutions.

### Acknowledgements

The research leading to this article has received support for Fapesp, Capes, Faepex and FUNDECT-UFMS. This is gratefully acknowledged.

### References

- [1] F. Aliabadi, *The Boundary Element Method: Applications in Solids and Structures*, Wiley (2001)
- [2] S.L. Crouch, A. Starfield, *Boundary Element Methods in Solid Mechanics*, HarperCollins (1983)
- [3] W. S. Hall, G. Olivetto, *Boundary Element Methods for Soil-Structure Interaction*, Kluwer Academic Publishers, 2003.
- [4] L. H. Thomazo,, "*Direct and iterative techniques for the Boundary Element Method*". PhD Thesis (in portuguese) FEM/UNICAMP (work in progress).

## Mesh Free Galerkin Method for Dynamic Fracture Mechanics with Enriched Radial Base Functions

P.H. Wen<sup>1</sup> and M.H. Aliabadi<sup>2</sup>

<sup>1</sup> Department of Engineering, Queen Mary, University of London, London, UK, E1 4NS

<sup>2</sup> Department of Aeronautics, Imperial College, London, UK, SW7 2BY

**Key words:** Element-free Galerkin method, Laplace transformation method, Enriched radial base function.

**Abstract:** Based on the variation of potential energy, the element-free Galerkin method is developed on the basis of finite element method by the use of radial base function interpolation for dynamic fracture mechanics in this paper. An enriched radial base function is introduced to capture the singularity of stress at the crack tip. Comparisons have been made with benchmark analytical solutions and boundary element method.

### 1. Introduction

Remarkable successes of meshless local Petrov-Galerkin method have been reported in solving convection-diffusion problems by Liu and Atluri [1] and dynamic fracture problem by Liu *et al* [2] respectively. In this paper, the basic concepts and numerical implementation of mesh free Galerkin method for solving dynamic fracture problems are presented. An element free Galerkin method is presented in the Laplace transformation domain with compactly supported enriched radial basis function (RBF) interpolation. Following the same technique to derive system equations for finite element method, the stiffness matrix is established by the variation of potential energy using enriched RBF interpolations. Therefore, the stiffness matrix is still symmetric and has a diagonal strip distribution and also this method can be combined with FEM directly. The stress intensity factor is obtained by crack opening displacement and the time dependent values are evaluated by Durbin inversion method. The accuracy of proposed method has been demonstrated through benchmark examples.

### 2. Variation of potential energy

For a linear two dimensional elasticity, governing equations are written as follows

$$\sigma_{ij,j} + f_i = \rho \ddot{u}_i \quad (1)$$

where  $\sigma_{ij}$  denotes the stress tensor,  $f_i$  the body force,  $\rho$  is the mass density. Consider the domain  $\Omega$  enclosed by boundary  $\Gamma$ , we have the total potential energy for the plane stress by

$$\Pi = U - W \quad (2)$$

where the initial elastic strain energy

$$U = \frac{1}{2} \int_{\Omega} \boldsymbol{\sigma}^T(\mathbf{y}) \boldsymbol{\varepsilon}(\mathbf{y}) d\Omega(\mathbf{y}) = \frac{1}{2} \int_{\Omega} \boldsymbol{\varepsilon}^T(\mathbf{y}) \mathbf{D} \boldsymbol{\varepsilon}(\mathbf{y}) d\Omega(\mathbf{y}) \quad (3)$$

and the external energy, the sum of contributions from known interior and boundary forces, is

$$W = \int_{\Omega} \mathbf{u}^T(\mathbf{y}) \mathbf{b}(\mathbf{y}) d\Omega(\mathbf{y}) - \rho \int_{\Omega} \mathbf{u}^T(\mathbf{y}) \ddot{\mathbf{u}}(\mathbf{y}) d\Omega(\mathbf{y}) + \int_{\Gamma} \mathbf{u}^T(\mathbf{y}) \mathbf{t}(\mathbf{y}) d\Gamma(\mathbf{y}) \quad (4)$$

where  $\mathbf{b} = \{b_1, b_2\}^T$  is the body force vector,  $\mathbf{t} = \{t_1, t_2\}^T$  in which  $t_i = \sigma_{ij} n_j$ . We assume that the displacements  $\mathbf{u}(\mathbf{y})$  at the point  $\mathbf{y}$  can be approximated in terms of the nodal values in a local domain as

$$u_i(\mathbf{y}) = \sum_{k=1}^{n(\mathbf{y})} \phi_k(\mathbf{y}, \mathbf{x}_k) \hat{u}_i^k = \bar{\Phi}(\mathbf{y}, \mathbf{x}) \hat{\mathbf{u}}_i \quad (5)$$

where

$$\overline{\Phi}(\mathbf{y}, \mathbf{x}) = \{\phi_1(\mathbf{y}, \mathbf{x}_1), \phi_2(\mathbf{y}, \mathbf{x}_2), \dots, \phi_{n(\mathbf{y})}(\mathbf{y}, \mathbf{x}_{n(\mathbf{y})})\} \quad (6)$$

$\hat{u}_i(\mathbf{x})$  is the nodal values at point  $\mathbf{x}_k = \{x_1^{(k)}, x_2^{(k)}\}$ ,  $k = 1, 2, \dots, n(\mathbf{y})$ ,  $\phi_k$  the shape function and  $n(\mathbf{y})$  the total number of node in the local domain named as the supported domain. For the two dimensional plane stress case, we can rearrange the above relation as follows

$$\mathbf{u}(\mathbf{y}) = \{u_1, u_2\}^T = \Phi(\mathbf{y}, \mathbf{x}) \hat{\mathbf{u}} \quad (7)$$

$$\Phi(\mathbf{y}, \mathbf{x}) = \begin{bmatrix} \overline{\Phi} & 0 \\ 0 & \overline{\Phi} \end{bmatrix} = \begin{bmatrix} \phi_1 & 0 & \phi_2 & 0 & \dots & \phi_{n(\mathbf{y})} & 0 \\ 0 & \phi_1 & 0 & \phi_2 & \dots & 0 & \phi_{n(\mathbf{y})} \end{bmatrix}$$

To arrive at the system equations in terms of nodal displacement, consider the variation of the total potential energy, with respect to each nodal displacements, to give

$$\delta \Pi = \delta U - \delta W = 0 \quad (8)$$

Inserting the relations  $\mathbf{u} = \Phi \hat{\mathbf{u}}$ ,  $\boldsymbol{\varepsilon} = \mathbf{B} \hat{\mathbf{u}}$  and  $\boldsymbol{\sigma} = \mathbf{D} \boldsymbol{\varepsilon}$  into Eq.(8) yields  $2 \times N$  linear algebraic equations in the global coordinate system:

$$[\mathbf{K}]_{2N \times 2N} \hat{\mathbf{u}}_{2N} + \rho [\mathbf{C}]_{2N \times 2N} \hat{\mathbf{u}} = \mathbf{f}_{2N} \quad (9)$$

where  $N$  is the total number of node in the domain  $\Omega$ . The stiffness and mass matrices become:

$$\mathbf{K} = \int_{\Omega} \mathbf{B}^T(\mathbf{x}, \mathbf{y}) \mathbf{D}(\mathbf{y}) \mathbf{B}(\mathbf{x}, \mathbf{y}) d\Omega(\mathbf{y}) \quad (10)$$

$$\mathbf{C} = \int_{\Omega} \Phi^T(\mathbf{x}, \mathbf{y}) \Phi(\mathbf{x}, \mathbf{y}) d\Omega(\mathbf{y})$$

for nodes  $\mathbf{x} = \mathbf{x}_i$   $i = 1, 2, \dots, N$ , and nodal force vector is

$$\mathbf{f} = \int_{\Omega} \Phi^T(\mathbf{x}, \mathbf{y}) \mathbf{b}(\mathbf{y}) d\Omega(\mathbf{y}) + \int_{\Gamma_{\sigma}} \Phi^T(\mathbf{x}, \mathbf{y}) \mathbf{t}(\mathbf{y}) d\Gamma(\mathbf{y}) \quad (11)$$

where  $\Gamma_{\sigma}$  denotes the boundary on which the traction is given.

### 3. The approximation scheme

A sub-domain  $\Omega_y$  is the neighbourhood of a point  $\mathbf{y}$  and is also called support domain to an arbitrary point  $\mathbf{y}$ . The distribution of function  $u$  in the sub-domain  $\Omega_y$  over a number of randomly distributed nodes  $\{\mathbf{x}_i\}$ ,  $i = 1, 2, \dots, n(\mathbf{y})$  can be interpolated, at the point  $\mathbf{y}$ , by

$$u(\mathbf{y}) = \sum_{i=1}^{n(\mathbf{y})} R_i(\mathbf{y}, \mathbf{x}_i) a_i = \mathbf{R}^T(\mathbf{y}, \mathbf{x}) \mathbf{a}(\mathbf{y}) \quad (12)$$

where  $\mathbf{R}^T(\mathbf{y}, \mathbf{x}) = \{R_1(\mathbf{y}, \mathbf{x}), R_2(\mathbf{y}, \mathbf{x}), \dots, R_{n(\mathbf{y})}(\mathbf{y}, \mathbf{x})\}$  is the set of radial basis functions centred at the point  $\mathbf{y}$ ,  $\{a_k\}_{k=1}^{n(\mathbf{y})}$  are the unknown coefficients to be determined. To capture the singular stresses in front of the crack tip, the enriched radial basis function has been selected to be the following

$$R_k(\mathbf{y}, \mathbf{x}) = R(\mathbf{y} - \mathbf{x}_k) + Q(\mathbf{y}) = \sqrt{c^2 + |\mathbf{y} - \mathbf{x}_k|^2} + (\beta + \sqrt{r} e^{-\alpha r}) \quad (13)$$

where  $r = |\mathbf{y} - \mathbf{y}_c|$ ;  $\alpha$ ,  $\beta$  and  $c$  are three free parameters;  $\mathbf{y}_c = (y_1^{(c)}, y_2^{(c)})$  denotes the crack tip. Also we select  $c=b$  ( $b$  is specified length, such as the width of the rectangular plate) in this paper. From the interpolation strategy in Eq.(13) for RBF, a linear system for the unknowns coefficients  $\mathbf{a}$  is obtained by

$$\mathbf{R}_0 \mathbf{a} = \hat{\mathbf{u}} \quad (14)$$

where coefficient matrix

$$\mathbf{R}_0 = \begin{bmatrix} R_1(\mathbf{x}_1, \mathbf{x}_1) & R_2(\mathbf{x}_1, \mathbf{x}_2) & \dots & R_{n(y)}(\mathbf{x}_1, \mathbf{x}_{n(y)}) \\ R_1(\mathbf{x}_2, \mathbf{x}_1) & R_2(\mathbf{x}_2, \mathbf{x}_2) & \dots & R_{n(y)}(\mathbf{x}_2, \mathbf{x}_{n(y)}) \\ \vdots & \vdots & \dots & \vdots \\ R_1(\mathbf{x}_{n(y)}, \mathbf{x}_1) & R_2(\mathbf{x}_{n(y)}, \mathbf{x}_2) & \dots & R_{n(y)}(\mathbf{x}_{n(y)}, \mathbf{x}_{n(y)}) \end{bmatrix} \quad (15)$$

As the RBFs are positive definite, the matrix  $\mathbf{R}_0$  is assured to be invertible. Therefore, we can obtain the vector of unknowns from Eq.(14)

$$\mathbf{a} = \mathbf{R}_0^{-1}(\mathbf{x})\hat{\mathbf{u}}(\mathbf{x}) \quad (16)$$

So that the approximation  $u(\mathbf{y})$  can be represented, at domain point  $\mathbf{y}$ , as

$$u(\mathbf{y}) = \mathbf{R}^T(\mathbf{y}, \mathbf{x})\mathbf{R}_0^{-1}(\mathbf{x})\hat{\mathbf{u}}(\mathbf{x}) = \overline{\Phi}(\mathbf{y}, \mathbf{x})\hat{\mathbf{u}} = \sum_{k=1}^{n(y)} \phi_k \hat{u}_k \quad (17)$$

where the nodal shape function are defined by

$$\overline{\Phi}(\mathbf{y}, \mathbf{x}) = \mathbf{R}^T(\mathbf{y}, \mathbf{x})\mathbf{R}_0^{-1}(\mathbf{x}) \quad (18)$$

It is worth noticing that the shape function depends uniquely on the distribution of scattered nodes within the support domain and has the property of Kronecker Delta. As the inverse matrix of coefficient  $\mathbf{R}_0^{-1}(\mathbf{x})$  is a function only of distributed node  $\mathbf{x}_i$  in the support domain, it is much simpler to evaluate the partial derivatives of shape function. From Eq.(12), we have

$$u_{,k}(\mathbf{y}) = \overline{\Phi}_{,k}(\mathbf{y}, \mathbf{x})\hat{\mathbf{u}} = \sum_{i=1}^{n(y)} \phi_{i,k} \hat{u}_i \quad (19)$$

where

$$\begin{aligned} \overline{\Phi}_{,k}(\mathbf{y}, \mathbf{x}) &= \mathbf{R}_{,k}^T(\mathbf{y}, \mathbf{x})\mathbf{R}_0^{-1}(\mathbf{x}) \\ &= [R_{1,k}(\mathbf{y}, \mathbf{x}), R_{2,k}(\mathbf{y}, \mathbf{x}), \dots, R_{n(y),k}(\mathbf{y}, \mathbf{x})]\mathbf{R}_0^{-1}(\mathbf{x}) \end{aligned} \quad (20)$$

From Eq. (13), we have

$$R_{i,k}(\mathbf{y}, \mathbf{x}_i) = \frac{y_k - x_k^{(i)}}{\sqrt{c^2 + |\mathbf{y} - \mathbf{x}_i|^2}} + \frac{y_k - y_k^{(c)}}{r} \left( \frac{1}{2\sqrt{r}} - \alpha \right) e^{-\alpha r}. \quad (21)$$

Therefore, the displacement derivatives have  $1/\sqrt{r}$  singularity near the crack tip.

#### 4. Numerical process to evaluate stiffness matrix

To determine the stiffness matrix  $\mathbf{K}$  in Eq.(10), a domain integral over the domain  $\Omega$  should be carried out. For convenience of analysis, we assume that the domain can be divided into  $M$  rectangular sub-regions. The 2D domain integral over a rectangular of area  $A$  is approximated by the Gaussian integration formula as

$$\iint_A f(x_1, x_2) dx_1 dx_2 \approx A \sum_{l=1}^L w_l f(x_1^{(l)}, x_2^{(l)}) \quad (22)$$

where  $w_l$  denotes the weight of integral,  $L$  the number of Gaussian points and  $(x_1^{(l)}, x_2^{(l)})$  is the coordinate of Gaussian points. If domain  $\Omega$  is divided into  $M$  sub-domain, then the matrix of stiffness can be written, using four Gaussian points scheme, as the following

$$\mathbf{K}(\mathbf{x}) = \int_{\Omega} \mathbf{B}^T(\mathbf{x}, \mathbf{y}) \mathbf{D}(\mathbf{y}) \mathbf{B}(\mathbf{x}, \mathbf{y}) d\Omega(\mathbf{y}) = \sum_{m=1}^M \sum_{l=1}^4 \frac{A_m}{4} \mathbf{B}^T(\mathbf{x}, \mathbf{y}_m^{(l)}) \mathbf{D}(\mathbf{y}_m^{(l)}) \mathbf{B}(\mathbf{x}, \mathbf{y}_m^{(l)}) = \sum_{m=1}^M \sum_{l=1}^4 \Delta \mathbf{K}_l^m \tag{23}$$

$$\mathbf{C}(\mathbf{x}) = \int_{\Omega} \Phi^T(\mathbf{x}, \mathbf{y}) \Phi(\mathbf{x}, \mathbf{y}) d\Omega(\mathbf{y}) = \sum_{m=1}^M \sum_{l=1}^4 \frac{A_m}{4} \Phi^T(\mathbf{x}, \mathbf{y}_m^{(l)}) \Phi(\mathbf{x}, \mathbf{y}_m^{(l)}) = \sum_{m=1}^M \sum_{l=1}^4 \Delta \mathbf{C}_l^m$$

where the integration points  $\mathbf{y}_m^{(l)}(y_1^{(ml)}, y_2^{(ml)})$  and coefficients  $w_l$  are given by

$$\mathbf{y}_m^{(1,2,3,4)} = \left( y_1^m \pm \sqrt{\frac{1}{3}} h_1, y_2^m \pm \sqrt{\frac{1}{3}} h_2 \right), \quad w_{1,2,3,4} = \frac{1}{4}, \tag{24}$$

in which  $\mathbf{y}_m(y_1^m, y_2^m)$  presents the centre of sub integral domain with area  $A_m$  (rectangular),  $h_1$  and  $h_2$  are half of the width and height of the rectangular region respectively and  $A_m = 4h_1h_2$ . For each Gaussian point  $\mathbf{y}_l$ , the elements in the stiffness sub-matrix  $\Delta \mathbf{K}_l^m$  can be simplified to

$$\Delta \mathbf{K}_l^m = \frac{A_m E(1-\nu)}{4(1+\nu)(1-2\nu)} \begin{bmatrix} \frac{\partial \phi_i}{\partial y_1} \frac{\partial \phi_j}{\partial y_1} + \frac{1-2\nu}{2(1-\nu)} \frac{\partial \phi_i}{\partial y_2} \frac{\partial \phi_j}{\partial y_2} & \frac{\nu}{1-\nu} \frac{\partial \phi_i}{\partial y_1} \frac{\partial \phi_j}{\partial y_2} + \frac{1-2\nu}{2(1-\nu)} \frac{\partial \phi_i}{\partial y_2} \frac{\partial \phi_j}{\partial y_1} \\ \frac{\nu}{1-\nu} \frac{\partial \phi_i}{\partial y_2} \frac{\partial \phi_j}{\partial y_1} + \frac{1-2\nu}{2(1-\nu)} \frac{\partial \phi_i}{\partial y_1} \frac{\partial \phi_j}{\partial y_2} & \frac{\partial \phi_i}{\partial y_2} \frac{\partial \phi_j}{\partial y_2} + \frac{1-2\nu}{2(1-\nu)} \frac{\partial \phi_i}{\partial y_1} \frac{\partial \phi_j}{\partial y_1} \end{bmatrix}_{ij}$$

$$= \begin{bmatrix} k_{11}^l & k_{12}^l \\ k_{21}^l & k_{22}^l \end{bmatrix}_{ij} \tag{25}$$

$$\Delta \mathbf{C}_l^m = \begin{bmatrix} \phi_i \phi_j & 0 \\ 0 & \phi_i \phi_j \end{bmatrix}_{ij} \tag{26}$$

where  $i$  and  $j$  denote the number of nodes in the local support domain centred at  $\mathbf{y}_l$ ,  $\phi_i = \phi_i(\mathbf{y}_l, \mathbf{x})$ ,  $i, j=1,2,\dots,n(\mathbf{y}_l)$ . These four values in Eq. (25) should be added to the global system stiffness matrix  $\mathbf{K}$ , i.e. to the elements  $k_{2I-1,2J-1}, k_{2I-1,2J}, k_{2I,2J-1}$  and  $k_{2I,2J}$  respectively, where  $I$  and  $J$  denote the numbers in the global system for the node  $i$  and  $j$  in the local support domain centred at  $\mathbf{y}_l$ . For each Gaussian point  $\mathbf{y}_l$ , the number of node  $i$  varies due to the change of centre of the support domain.

For convenience of analysis, the hat of variables (^) is removed in the following. Applying the Laplace transform to the Eq. (9) will give

$$([\mathbf{K}] + \rho s^2 [\mathbf{C}]) \tilde{\mathbf{u}} = \tilde{\mathbf{f}} \tag{27}$$

The Laplace transform of function  $f(\mathbf{x}, t)$  is defined as

$$\tilde{f}(\mathbf{x}, s) = \int_0^{\infty} f(\mathbf{x}, t) e^{-st} dt \tag{28}$$

where  $s$  is a Laplace parameter. In the system stiffness matrix  $\mathbf{K}$  in Eq. (23), the integral function has strong singularity of  $O(1/r)$ . Therefore, we need to use coordinate transformation technique to cancel that singularity for the integral sub region at the crack tip. For example, the sub region (two squares) is divided into four triangular sub domains and each triangular domain is transformed to a square. The transformations are

- Triangular I:  $y_1 = \xi_1$  and  $y_2 = \frac{1}{2}[(1 + \xi_1)\xi_2 - (1 - \xi_1)]$ ;  $J_c = \frac{1}{2}(1 + \xi_1)$
- Triangular II:  $y_1 = \frac{1}{2}[(1 + \xi_1)\xi_2 - (1 - \xi_1)]$  and  $y_2 = \xi_1$ ;  $J_c = \frac{1}{2}(1 + \xi_1)$

- Triangular III:  $y_1 = \frac{1}{2}[(1 + \xi_2)\xi_1 + (1 - \xi_2)]$  and  $y_2 = \xi_2$ ;  $J_c = \frac{1}{2}(1 + \xi_2)$
- Triangular IV:  $y_1 = -\xi_2$  and  $y_2 = -\frac{1}{2}[(1 + \xi_2)\xi_1 + (1 - \xi_2)]$ ;  $J_c = \frac{1}{4}(1 + \xi_2)$

Thus, the integral with a strong singularity at  $\mathbf{y}_c$  (-1,-1) can be written as

$$\int_{-1}^1 \int_{-1}^1 \frac{F(y_1, y_2)}{r} dy_1 dy_2 = \int_{-1}^1 \int_{-1}^1 \frac{F(y_1, y_2)}{r} J_c'(\xi_1) d\xi_1 d\xi_2 + \int_{-1}^1 \int_{-1}^1 \frac{F(y_1, y_2)}{r} J_c''(\xi_2) d\xi_1 d\xi_2 + \int_{-1}^1 \int_{-1}^1 \frac{F(y_1, y_2)}{r} J_c'''(\xi_1) d\xi_1 d\xi_2 + \int_{-1}^1 \int_{-1}^1 \frac{F(y_1, y_2)}{r} J_c''''(\xi_2) d\xi_1 d\xi_2 \quad (29)$$

where the Jacobian of transformation cancel out the  $1/r$  singularity.

#### *A Single central crack in rectangular plate under tension*

Consider a rectangular plate of width  $2b$  and length  $2h$  with a centrally located crack of length  $2a$ . It is loaded dynamically in the direction perpendicular to the crack by a uniform tension  $\sigma_0 H(t)$  on the top and the bottom. Due to the symmetry, a quarter of plate is considered as shown in Figure 1. Here Poisson's ratio  $\nu=0.3$  and Young's modulus is unit. A set of  $11 \times 11$  ( $N_{\text{total}} = 121$ ) uniformly distributed nodes is used and the integration is performed by dividing the square into  $10 \times 10$  cells with  $4 \times 4$  Gauss points in each cell. Two cells near the crack tip need to be divided into four triangles for the strong singularity of integration at crack tip and  $9 \times 9$  Gauss points for these triangular cells. However, we found that for large number of support nodes in the sub-domain, the interpolation will become unstable due to the computational precision of FORTRAN. By the investigation of free parameters for enriched radial base function for elastostatic crack problems, optimized free parameters  $\alpha$  and  $\beta$  are chosen as units and the distance between collocation point and crack tip to evaluate stress intensity factor  $r_0 / \Delta = 1$ , where  $\Delta$  is the gap between two nodes. The analytical static solution for a square plate ( $b=h$ ) containing a central crack, if  $a/b=0.5$ ,  $K_I = 1.325\sigma_0\sqrt{\pi a}$  [4] and the result by this method  $K_I = 1.306\sigma_0\sqrt{\pi a}$ .

Three geometries of rectangular plate are considered in this example, i.e.  $h=0.5b$ ,  $h=b$  and  $h=2b$  while  $a=0.5b$ . The total numbers of nodes for each case are selected as 66, 121 and 231 respectively. Figures 2, 3 and 4 show normalized stress intensity factors against normalized time  $c_1 t / b$ . To demonstrate the accuracy of mesh free method, the results given by Wen *et al* [5] using the indirect boundary element method are presented for comparison.

#### **References**

- [1] H. Liu and S.N. Atluri, The meshless local Petrov-Galerkin method for solving incompressible Navier-Stokes equations, *Comput. Model Eng. Sci.*, **1**(2), 45-60, 2000.
- [2] K. Liu, S. Long and G. Li, A simple less-costly meshless local Petro-Galerkin (MLPG) method for the dynamic fracture problem, *Engng Analy with Boundary Elements*, **30**, 72-76, 2006.
- [3] P. Fedelinski, M.H. Aliabadi and D. P. Rook, The dual boundary element method: J-integral for dynamic stress intensity factors, *Int. J. Fracture*, **65**, 369-381, 1994.
- [4] D.P. Rooke, D.J. Cartwright, *Compendium of Stress Intensity Factors*, London, Her Majesty's Stationery Office, 1976.
- [5] P.H. Wen, *Dynamic Fracture Mechanics: Displacement Discontinuity Method*, Computational Mechanics Publications, Southampton UK and Boston USA, 1996.

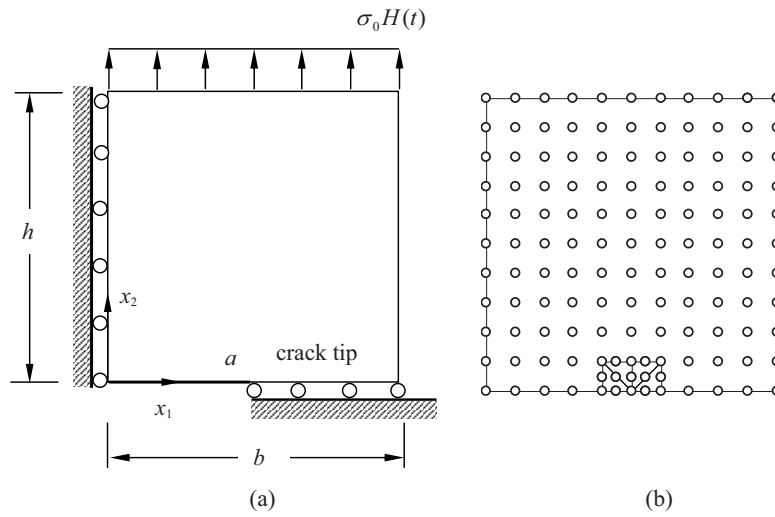


Figure 1. Rectangular plate with a central crack of length  $2a$  under tension  $\sigma_0 H(t)$ : (a) a quarter of the plate; (b) uniformly distributed nodes.

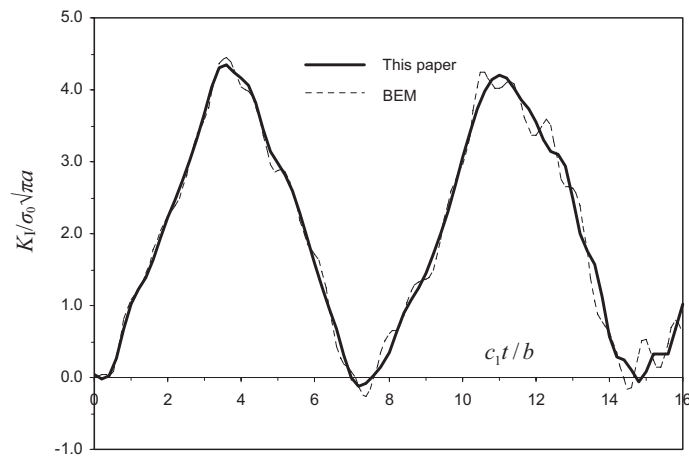


Figure 2. Normalized stress intensity factors vs. normalized time when  $h/b=0.5$ .

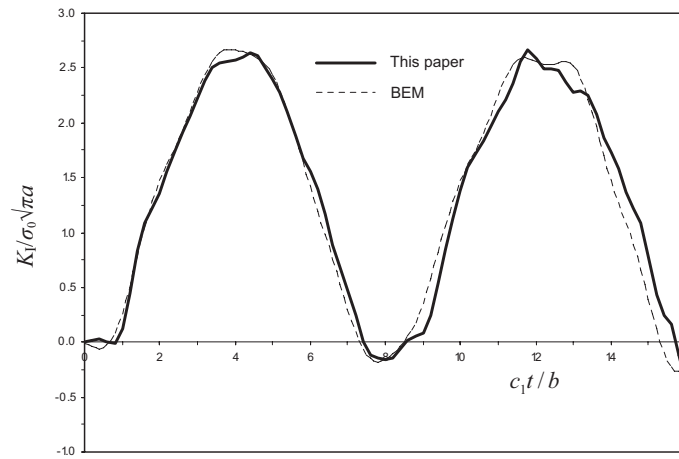


Figure 3. Normalized stress intensity factors vs. normalized time when  $h/b=1$ .

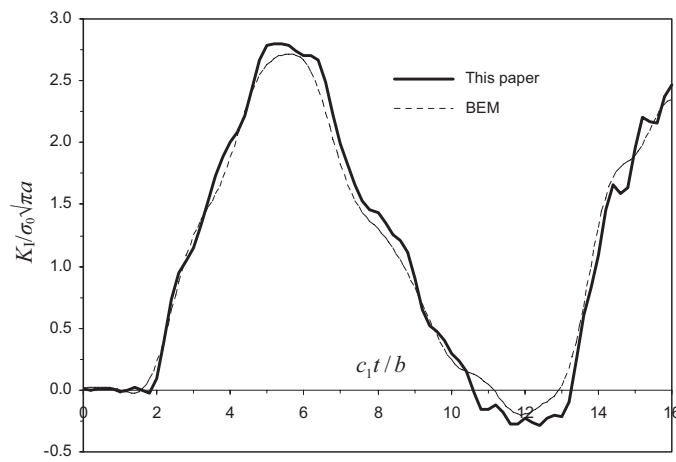


Figure 4. Normalized stress intensity factors vs. normalized time when  $h/b=2$ .



## A New BEM for Sensitivity Analysis of Acoustic Fields with the Fictitious Eigenvalue Issue

Masataka Tanaka<sup>1</sup>, Yuri Arai<sup>2</sup> and Toshiro Matsumoto<sup>3</sup>

<sup>1</sup>Department of Mechanical Systems Engineering, Shinshu University, Nagano, 380-8553 Japan  
E-mail: dtanaka@gipwc.shinshu-u.ac.jp

<sup>2</sup>Department of Mechanical Systems Engineering, Shinshu University, Nagano, 380-8553 Japan  
E-mail: youri@artist.shinshu-u.ac.jp

<sup>3</sup>Department of Mechanical Science and Engineering, Nagoya University, Nagoya, 464-8603 Japan  
E-mail: t.matsumoto@nuem.nagoya-u.ac.jp

**Keywords:** Computational Mechanics, Boundary Element Method, Sensitivity Analysis, Acoustics, Helmholtz Equation, Fictitious Eigenfrequency Problem

**Abstract.** This paper presents a new sensitivity analysis based on BEM avoiding the fictitious eigenfrequency issue for the three - dimensional external acoustic field. In solving without any care the external acoustic field problem governed by the Helmholtz equation by means of a boundary integral equation, accuracy of the numerical solution is disturbed at eigenfrequencies of the interior problem. The present approach uses higher-order boundary elements, and two boundary integral equations obtained by differentiation with respect to design parameters. One equation is the combined boundary integral equation proposed by Burton - Miller and the other is the normal derivative boundary integral equation multiplied by the same coupling parameter as in the Burton - Miller expression. The effectiveness and validity of the proposed approach is demonstrated through numerical a 3-D example.

### 1 Introduction

For optimal design or inverse analysis, it is frequently necessary to compute design sensitivity with respect to the design variable. One of such methods is the finite difference scheme, in which two values of the optimal function are needed in a sufficiently small difference. Such two computations of the design function may lead to a larger amount of computational time in analysis, and another approach should be explored for a smaller amount of computational time. At this end, the present paper proposes a new design sensitivity analysis based on the boundary integral equation formulation excluding the so-called fictitious eigenfrequency issue in acoustic problems.

It is well known, e.g. in Refs.[1] and [2], that the solution of the external acoustic problem including in it another empty domain is disturbed near the eigenfrequencies of the inner domain. This trouble is called the fictitious eigenfrequency issue, and there is available a remedy for this trouble; This is called the Burton-Miller method[3]. The authors recently proposed an alternative to this approach to reduce computational time; In case of discretization by higher-order BE, we use at a smaller number of nodal points the Burton-Miller integral expression, while at the other nodal points we employ the normal derivative boundary integral equation multiplied with the same combination parameter as above[4, 5]. The two methods work well, and the present paper is concerned with sensitivity analysis along this direction. The boundary integral formulation is in detail presented for sensitivity analysis, and the effectiveness of the proposed method is demonstrated through comparison of the numerical results with other methods.

### 2 Theoretical Background

The boundary integral equation formulation proposed by the authors[4, 5] for avoiding the fictitious eigenvalue issue is briefly explained, to present the related boundary integral equation expressions.

#### 2.1 Alternative Boundary Integral Formulation

Under the assumption of steady-state vibration with an infinitesimal amplitude, the acoustic fields are governed by the Helmholtz equation[6, 7]:

$$\nabla^2 p(x) + k^2 p(x) + f(x) = 0 \quad (1)$$

where  $p(x)$  denotes the sound pressure,  $\omega$  the angular velocity and  $f(x)$  the source term. If we denote by  $k$  the wave number and by  $c$  the sound speed, we have the wave number  $k = \omega/c$ .

According to the boundary integral equation formulation, the above Helmholtz equation (1) is transformed to the following boundary integral equation:

$$\begin{aligned} & \int_{\Gamma} \{q^*(x, y) - Q^*(x, y)\} p(x) d\Gamma(x) + \int_{\Gamma} Q^*(x, y) \{p(x) - p(y)\} d\Gamma(x) \\ & = -i\omega\rho \int_{\Gamma} p^*(x, y) v(x) d\Gamma(x) + Ip^*(x^s, y) \end{aligned} \quad (2)$$

under the assumption that the source term  $f(x)$  in Eq.(1) is the point source, in which  $I$  is the source intensity and  $x^s$  the application point. In Eq.(2),  $p^*(x, y)$  is the fundamental solution for Helmholtz equation,  $q^*(x, y)$  its normal derivative and  $Q^*(x, y)$  the normal derivative of the fundamental solution for Laplace equation.

It is interesting to note that the above integral expression has been normalized by considering the uniform distribution of potential  $p$ [2, 4, 5]. This is the standard BIE formulation, and let us call Eq.(2) the ordinary boundary integral equation (OBIE).

On the other hand, we may derive the normal derivative boundary integral equation (NDBIE), which can be obtained as the directional derivative of Eq. (2) with respect to  $n(y)$ . Taking into account the uniform gradient condition[5], we obtain

$$\begin{aligned} & \int_{\Gamma} \{\tilde{q}^*(x, y) - \tilde{Q}^*(x, y)\} p(x) d\Gamma(x) + \int_{\Gamma} \tilde{Q}^*(x, y) \{p(x) - p(y) - r_m(x, y) p_{,m}(y)\} d\Gamma(x) \\ & = -i\omega\rho \left[ \int_{\Gamma} \{\tilde{p}^*(x, y) - \tilde{u}^*(x, y)\} v(x) d\Gamma(x) + \int_{\Gamma} \tilde{u}^*(x, y) \{v(x) - n_m(x) p_{,m}(y)\} d\Gamma(x) \right] \\ & \quad + I\tilde{p}^*(x^s, y) \end{aligned} \quad (3)$$

where  $i$  is the imaginary unit and  $\tilde{() } = \partial()/\partial n(y)$ . This boundary integral equation should be called NDBIE.

The asterisked functions, related to the fundamental solutions for Helmholtz and Laplace equations, are given as follows:

$$p^*(x, y) = \frac{1}{4\pi r} \exp(-ikr) \quad (4)$$

$$q^*(x, y) = -\frac{1}{4\pi r^2} (1 + ikr) \exp(-ikr) \frac{\partial r}{\partial n}(x) \quad (5)$$

$$Q^*(x, y) = -\frac{1}{4\pi r^2} \frac{\partial r}{\partial n}(x) \quad (6)$$

$$\tilde{u}^*(x, y) = -\frac{1}{4\pi r^2} \frac{\partial r}{\partial n}(y) \quad (7)$$

$$\tilde{Q}^*(x, y) = \frac{1}{4\pi r^3} \left\{ 3 \frac{\partial r}{\partial n}(x) \frac{\partial r}{\partial n}(y) + n_j(x) n_j(y) \right\} \quad (8)$$

$$\tilde{p}^*(x, y) = -\frac{1}{4\pi r^2} (1 + ikr) \exp(-ikr) \frac{\partial r}{\partial n}(y) \quad (9)$$

$$\begin{aligned} \tilde{q}^*(x, y) = & \frac{1}{4\pi r^3} \left[ \{3(1 + ikr) - k^2 r^2\} \frac{\partial r}{\partial n}(x) \frac{\partial r}{\partial n}(y) \right. \\ & \left. + (1 + ikr) n_j(x) n_j(y) \right] \exp(-ikr) \end{aligned} \quad (10)$$

Both Eqs. (2), OBIE, and (3), NDBIE, will fail to yield a unique solution, if the frequency coincides with any eigenfrequency of sub-domains. This is because the integral equations do not satisfy the condition of  $p = 0$  in sub-domain.

Burton and Miller[3] proposed a combined boundary integral equation, and proved that the combined boundary integral equation always has the trivial solution  $p = 0$  in sub-domain unless the imaginary coupling parameter  $\alpha$  which multiplies the NDBIE does not become  $\text{Im}(\alpha) \neq 0$ . The new alternative method recently proposed by the authors[4, 5], however, does not always employ the Burton-Miller combined boundary integral equation. If the source point is located on the middle nodal points of a boundary element with quadratic interpolation functions, the Burton-Miller combined integral equation is used, while if the source point is located on the extreme nodes of the element, Eq. (3) multiplied with the same coupling parameter as above is employed, and vice versa.

### 3 Sensitivity Analysis by Means of BIEM

Differentiation of the boundary integral equations with respect to the design variable may provide the necessary boundary integral expressions for sensitivity analysis. It is once again mentioned that the Burton-Miller approach uses only the combined integral expression (OBIE+ $\alpha$ NDBIE) for all the nodal points, while the present approach employs this combined integral expression at the middle nodal points, whereas at the other nodal points employs only the integral expression  $\alpha$ NDBIE. The smaller the number of nodal points using the Burton-Miller expression is, the smaller the computation task in coefficient matrices is.

The system of equations obtained from the present formulation, which connects the nodal values on the boundary can be expressed in the matrix form as

$$[H] \{p\} = [G] \{v\} + \{f\} \quad (11)$$

From this equation the nodal unknowns  $\{X\}$  can be determined by

$$[A] \{X\} = [B] \{Y\} + \{f\} \quad (12)$$

The above process can determine all the unknown nodal values on the boundary. Once all the nodal values are known, we can obtain the nodal values differentiated with respect to the design variable. The system of equations can be expressed in the matrix form as follows:

$$[H'] \{\dot{p}\} = [G'] \{\dot{v}\} + [h'] \{p\} + [g'] \{v\} + \{f'\} \quad (13)$$

The above system of equations can determine the nodal values of the unknown design sensitivities. It is noted that  $[H']$  and  $[G']$  are the coefficient matrices of the sensitivities for the sound pressure  $\dot{p}$  and the particle velocity  $\dot{v}$ , respectively. Coefficient matrices are identical so that  $[H'] = [H]$  and  $[G'] = [G]$ , if the same discretization scheme is adopted for computation of the nodal values on  $p$  and  $v$  as for their sensitivities. If the boundary nodes in which the sound pressure  $p$  or the particle velocity  $v$  is given by the boundary condition, their sensitivities are also known at that node. Keeping in mind this fact, we finally obtain the following system of equations for nodal unknowns  $\{\dot{X}\}$  in sensitivities:

$$[A] \{\dot{X}\} = [B] \{\dot{Y}\} + [h'] \{p\} + [g'] \{v\} + \{f'\} \quad (14)$$

It is interesting to note that we can use the  $LU$  decomposition of the matrix  $[A]$  to reduce computational time of sensitivities, when we first solve the system of equations for nodal unknowns  $\{\dot{X}\}$  in Eq.(12).

### 4 Numerical Results and Discussion

Let us consider an ellipsoidal cavity in the 3-D infinite domain, the outside surface of which vibrates and its inside surface does not vibrate. It is assumed that  $\rho = 1.2$  [kg/m<sup>3</sup>],  $c = 340$  [m/s], and that the principal axis lengths of the ellipsoid are as  $2a = 0.4$  [m] and  $2b = 0.2$  [m]. The outside boundary of the cavity is assumed to vibrate uniformly with the particle velocity  $v = 1.0$  [m/s]. Let us consider the external domain of the acoustic field.

A quadrilateral boundary element with quadratic interpolation functions is employed in discretization. The present discretization scheme is performed in the following way: The Burton-Miller integral expression, OBIE+ $\alpha$ NDBIE, is used when the source point is located at the middle nodal points, whereas the integral expression  $\alpha$ NDBIE is employed when the source point is at the corner nodes. According to Cunefare-Koopman[9], the coupling parameter  $\alpha$  is taken as a pure imaginary number  $\alpha=i/k$ , where  $i$  is the imaginary unit. The numerical results obtained by the present method are compared with those only by the usual boundary integral equation, OBIE, and those only by the Burton-Miller integral expression, OBIE+ $\alpha$ NDBIE. In this numerical computation, the frequency range between 1 [Hz] and 1 [kHz] is computed with the interval 1 [Hz].

In Fig. 1 are shown the present analysis model and the discretization of the part 1/8 of the full model. Even if computation is carried out under the other finer boundary element meshes, similar results were obtained, which may indicate that the present discretization gives a sufficient accuracy. In the present computation, a singular integration is evaluated by the sub-element method[8].

In Fig. 2 comparison is made between the sensitivities obtained by OBIE and the present method. It is noted again that the Burton-Miller method gives similar results to the present combined method. At the frequencies  $ka = 4.4$  and  $ka = 7$  the numerical results by the OBIE are so much disturbed and these frequencies coincide with the eigenfrequencies of the elliptic sub-domain.

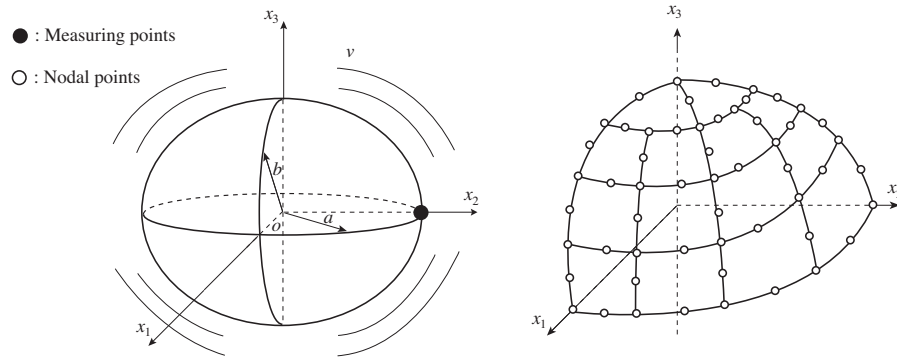


Figure 1 Analysis model and its boundary element discretization

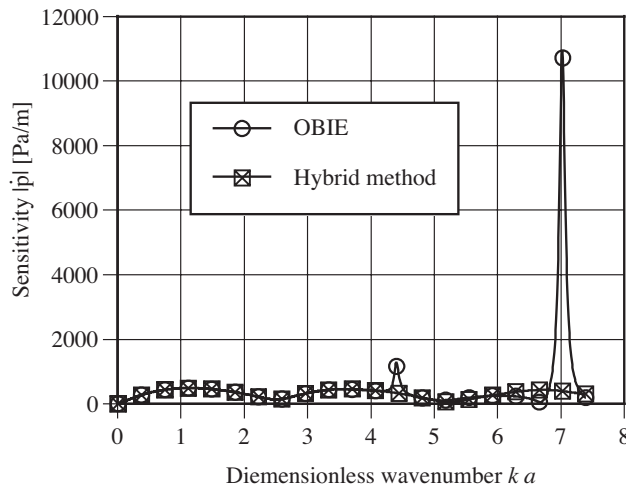


Figure 2 Comparison of numerical results obtained by OBIE and present hybrid method

Figure 3 shows the variation of the sound pressure level for the range between  $ka = 4.2$  and  $4.7$ , and Fig. 4 illustrates the sensitivity of the sound pressure with respect to the length of longitudinal axis  $2a$ , when the pressure is measured at the point  $(x_1, x_2, x_3)=(0, a, 0)$ . The present hybrid method can always give the correct numerical results in the sound pressure and its sensitivity as the Burton-Miller method, while the OBIE is troubled near the fictitious eigenfrequencies for computation of the sound pressure and also its sensitivity.

Similarly, the numerical results obtained for the range between  $ka = 6.5$  and  $7.4$  are shown in Figs. 5 and 6. It is shown that the present method is not disturbed by the fictitious eigenfrequency issue, and always gives the correct numerical results as the Burton-Miller method.

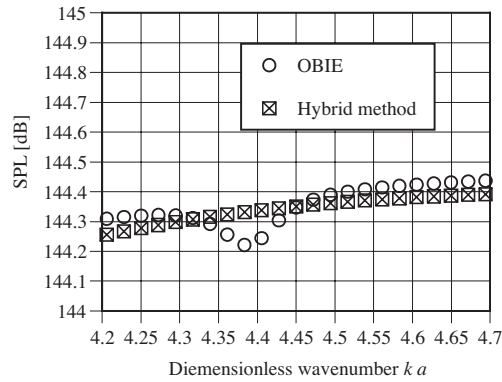


Figure 3 Comparison of SPL obtained by present hybrid method and only by OBIE for range between  $ka = 4.2$  and  $4.7$

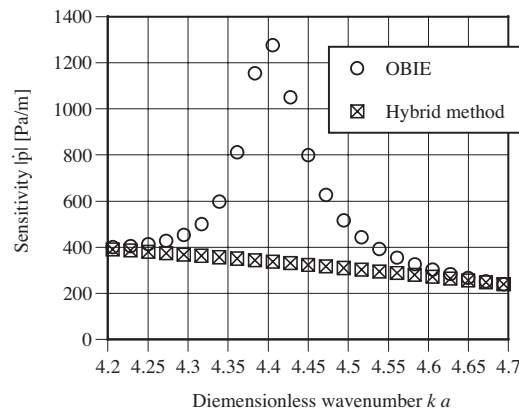


Figure 4 Comparison of sensitivities obtained by present hybrid method and only by OBIE for range between  $ka = 4.2$  and  $4.7$

### 5 Concluding Remarks

This paper has presented a new boundary element analysis of sensitivities with respect to the design variable for the acoustic problems with and without the fictitious eigenvalue issue. The proposed method can give the correct numerical results as the Burton-Miller method does. It is important that the present method can do the same under a smaller amount of computation task. The effectiveness of the proposed method was demonstrated by numerical computation for a 3-D simple example.

As future research work along this line, we may recommend extension of this method to optimal shape design of the acoustic fields.

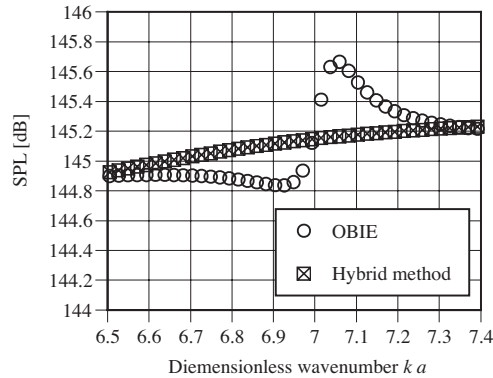


Figure 5 Comparison of SPL obtained by present hybrid method and only by OBIE for range between  $ka = 6.5$  and  $7.4$

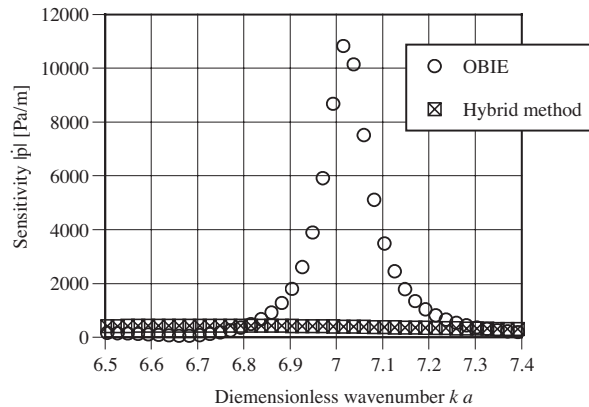


Figure 6 Comparison of sensitivities obtained by present hybrid method and only by OBIE for range between  $ka = 6.5$  and  $7.4$

## References

- [1] Kobayashi S (ed): *Wave Analysis and Boundary Element Method*. Kyoto University Press Online, (2000).
- [2] Tanaka M, Matsumoto T, Nakamura M: *Boundary Element Method*. Baifukan/Tokyo, (1991).
- [3] Burton AJ, Miller GF: The application of integral equation methods to the numerical solution of some exterior boundary-value problems. *Proc. Roy. Soc. London, Ser. A*, **323** (1971), pp.201–210.
- [4] Tanaka M, Matsumoto T, Arai Y: A boundary element analysis for avoiding the fictitious eigenfrequency problem in acoustic fields (2nd report). *Transactions of JSME, Ser.C*, **72-719** (2006), pp.2088–2063.
- [5] Arai Y, Tanaka M, Matsumoto T: A new BEM analysis of 2-D acoustic fields for avoiding fictitious eigenfrequency problem. *Systems Modelling and Simulation, Theory and Applications*, Asia Simulation Conference 2006, Springer, (2006). pp.44–47.
- [6] Norton MP *Fundamentals of Noise and Vibration Analysis for Engineers*. Cambridge Univ Press, (1989).
- [7] Beranek LL, Ver IL (eds): *Noise and Vibration Control Engineering - Principles and Applications*- John Wiley & Sons, (1992).
- [8] Yuuki R, Kisu H: *Boundary Element Methods for Elastic Analysis*. Baifukan/Tokyo, (1987).
- [9] Cunefare KA, Koopman G: A boundary element method for acoustic radiation valid for all wavenumbers. *J. Acoust. Soc. Am.*, **85** (1989), pp.39–48.

## Development of a time-domain fast multipole BEM based on the operational quadrature method in a wave propagation problem

Takahiro SAITOH<sup>1</sup>, Sohichi HIROSE<sup>2</sup>, Takuo FUKUI<sup>3</sup> and Takayuki ISHIDA<sup>4</sup>

<sup>1</sup>University of Fukui, 3-9-1, Bunkyo, Fukui-shi, Fukui, Japan, tsaito@taku.anc-d.fukui-u.ac.jp

<sup>2</sup>Tokyo Institute of Technology, 2-12-1, O-okayama, Meguro-ku, Tokyo, Japan, shirose@cv.titech.ac.jp

<sup>3</sup>University of Fukui, 3-9-1, Bunkyo, Fukui-shi, Fukui, Japan, tak@taku.anc-d.fukui-u.ac.jp

<sup>4</sup>University of Fukui, 3-9-1, Bunkyo, Fukui-shi, Fukui, Japan, stone@taku.anc-d.fukui-u.ac.jp

**Keywords:** Operational Quadrature Method (OQM), Fast Multipole Method (FMM)

**Abstract.** This paper presents a new time-domain Fast Multipole Boundary Element Method in a wave propagation problem. In general, the use of direct time-domain BEM sometimes causes the instability of time-stepping solutions and needs much computational time and memory. To overcome these difficulties, in this paper, the Operational Quadrature Method (OQM) developed by Lubich is applied to establish the stability behavior of the time-stepping scheme and the convolution integral is numerically approximated by quadrature formulas, whose weights are computed by using the Laplace transform of the fundamental solutions. Moreover, the Fast Multipole Method is adapted to improve the computational efficiency for large scale problems. As numerical examples, scalar wave scattering problems are implemented by the proposed method and, the accuracy and computational efficiency are shown to validate this method.

## INTRODUCTION

Since the Boundary Element Method (BEM) is known as a suitable numerical approach for wave analysis, time-domain transient problems have been solved by many researchers using the BEM by Mansur and Brebbia[1], and Hirose[2]. In general, transient problems can usually be solved for unknown time-dependent quantities by a direct time-domain BEM with a time-stepping scheme. However, the use of direct time-domain BEM sometimes causes two problems. The one is the instability problem of time-stepping procedure and the other is computational efficiency problem for a large size problem. Recently, to overcome the former problem, the Operational Quadrature Method (OQM), proposed by Lubich[3-5], has been used for the BEM formulation for some engineering problems such as 2-D scalar wave problem[6], poroelastic problem[7] and 2-D anisotropic problem[8]. In the formulation of BEM using the OQM (OQ-BEM), the convolution integral is numerically approximated by a quadrature formula whose weights are determined by the Laplace transform of the fundamental solution and a linear multistep method. The computational complexity becomes  $O(LM^2N)$  for the problem with  $M$  elements,  $N$  time steps, and  $L$  expansion terms. On the other hand, the latter problem still can be remained and it is difficult to solve a large scale problem with the large number of  $M$  by using the (OQ-BEM).

In this paper, the Fast Multipole Method (FMM), proposed by Greengard and Rokhlin[9], is applied to the OQ-BEM to improve the computational efficiency problem. After the description of basic concept and formulation of the OQ-BEM accelerated by the FMM is presented for wave propagation problems, scattering problems by scatterers are solved by the proposed method and transient wave behaviors around the scatterers are demonstrated. Finally, the computational efficiency of the proposed method is confirmed.

### OPERATIONAL QUADRATURE METHOD

In this section, the operational quadrature method (OQM) is briefly described. The Operational Quadrature Method (OQM), first proposed by Lubich, approximates the convolution  $f * g(t)$  by a discrete convolution using the Laplace transform of the time dependent function  $f(t - \tau)$ . In general, the convolution integral is defined as follows:

$$f * g(t) = \int_0^t f(t - \tau)g(\tau)d\tau \quad , \quad t \geq 0 \quad (1)$$

where  $*$  denotes the convolution. The convolution integral defined by eq(1) is approximated by OQM as follows:

$$f * g(n\Delta t) \simeq \sum_j \omega_{n-j}(\Delta t)g(j\Delta t) \quad (2)$$

where the time  $t$  was divided into  $N$  equal steps  $\Delta t$ . Moreover,  $\omega_j(\Delta t)$  denotes the quadrature weights which are determined by the coefficients of the following power series with complex variable  $z$ , namely

$$F\left(\frac{\delta(\zeta)}{\Delta t}\right) = \sum_{n=0}^{\infty} \omega_n(\Delta t)z^n. \quad (3)$$

In eq(3),  $F$  is the Laplace transform of time dependent function  $f$ . The power series defined in eq(3) can be calculated by Cauchy's integral formula. Considering a polar coordinate transformation, the Cauchy's integral is approximated by a trapezoidal rule with  $L$  equal steps  $2\pi/L$  as follows:

$$\omega_n(\Delta t) = \frac{1}{2\pi i} \int_{|\zeta|=\rho} F\left(\frac{\delta(\zeta)}{\Delta t}\right) \zeta^{-n-1} d\zeta \simeq \frac{\rho^{-n}}{L} \sum_{l=0}^{L-1} F\left(\frac{\delta(\zeta_l)}{\Delta t}\right) e^{\frac{-2\pi i n l}{L}}. \quad (4)$$

where  $\delta(\zeta)$  is the quotient of the generating polynomials of a linear multistep method and  $\zeta_l$  is given by  $\zeta_l = \rho e^{2\pi i l/L}$ . In addition,  $\rho$  is the radius of a circle in the domain of analyticity of  $F$ .

### TIME-DOMAIN BEM FORMULATION FOR 2-D WAVE PROPAGATION PROBLEM

We consider the 2-D scattering problem of scalar waves in an exterior domain  $D$ . When the incident wave  $u_{in}$  hits the boundary surface  $S$  of a scatterer  $\bar{D}$ , scattered waves are generated by the interaction with the scatterer  $\bar{D}$ . Assuming the zero initial conditions, i.e.,  $u(\mathbf{x}, t = 0) = 0$  and  $\partial u(\mathbf{x}, t = 0)/\partial t = 0$ , the governing equation and boundary conditions are written as follows:

$$\nabla^2 u = \frac{1}{c^2} \frac{\partial^2 u}{\partial t^2} \quad \text{in } D \quad (5)$$

$$u = \hat{u} \quad \text{on } S_1, \quad q = \frac{\partial u}{\partial n} = \hat{q} \quad \text{on } S_2, \quad S_2 = S \setminus S_1 \quad (6)$$

where  $c$  is the velocity of scalar waves and  $\partial/\partial n$  shows the differentiation for outer normal direction on surface  $S$ . In eq(6),  $\hat{u}$  and  $\hat{q}$  are given boundary values. The time-domain boundary integral equation for scalar wave can be expressed by

$$C(\mathbf{x})u(\mathbf{x}, t) = u_{in}(\mathbf{x}, t) + \int_S G(\mathbf{x}, \mathbf{y}, t) * q(\mathbf{y}, t) dS_y - \int_S H(\mathbf{x}, \mathbf{y}, t) * u(\mathbf{y}, t) dS_y. \quad (7)$$

In eq(7),  $G(\mathbf{x}, \mathbf{y}, t)$  and  $H(\mathbf{x}, \mathbf{y}, t)$  denote the time-domain fundamental solution and its double layer kernel for 2-D scalar wave problem, respectively, defined as follows:

$$G(\mathbf{x}, \mathbf{y}, t) = \frac{1}{2\pi\sqrt{t^2 - r^2/c^2}} H\left(t - \frac{r}{c}\right), \quad H(\mathbf{x}, \mathbf{y}, t) = \frac{\partial}{\partial n} G(\mathbf{x}, \mathbf{y}, t) \quad (8)$$

where  $r$  is given by  $r = |\mathbf{x} - \mathbf{y}|$ ,  $\delta(\cdot)$  is the Dirac delta function and  $C$  is the free term[10]. Normally, eq(7) is discretized by using the appropriate interpolation functions for the unknown values and solved by a time-stepping algorithm. However, there are mainly two disadvantages for the conventional time-domain BEM. One is an instability problem encountered in the time-stepping procedure. The other is the difficulty in solving large scale problems.

#### TIME-DOMAIN FAST MULTIPOLE BEM FORMULATION BASED ON THE OQM

To overcome the disadvantages of the conventional time-domain BEM, the Operational Quadrature Method (OQM) and the Fast Multipole Method are introduced.

#### BEM FORMULATION BASED ON THE OQM

In solving the system of the boundary integral equation (7) numerically, the unknown displacement  $u$  and the normal derivative  $q$  are represented by using the approximation functions  $\phi_i$  as follows:

$$u(\mathbf{x}, t) = \sum_i \phi_i(\mathbf{x}) u_i(t), \quad q(\mathbf{x}, t) = \sum_i \phi_i(\mathbf{x}) q_i(t) \quad (9)$$

where  $u_i(t)$  and  $q_i(t)$  are time dependent boundary values for the  $i$ -th basis. Substituting eq(9) into the convolution boundary integral equation (7) and taking the limit of  $\mathbf{x} \in D \rightarrow \mathbf{x} \in S$  yields the equations

$$\frac{1}{2} \sum_i \phi_i(\mathbf{x}) u_i(n\Delta t) = u_{in}(\mathbf{x}, n\Delta t) + \sum_i \sum_{k=1}^n \left[ A_i^{n-k}(\mathbf{x}) q_i(k\Delta t) - B_i^{n-k}(\mathbf{x}) u_i(k\Delta t) \right]. \quad (10)$$

Applying eq(2) and eq(4) in the OQM to the convolution integrals in eq(7), the influence functions  $A_i^m$  and  $B_i^m$  can be obtained as follows:

$$A_i^m(\mathbf{x}) = \frac{\rho^{-m}}{L} \sum_{l=0}^{L-1} \int_S \hat{G}(\mathbf{x}, \mathbf{y}, s_l) \phi_i(\mathbf{y}) e^{-\frac{2\pi i m l}{L}} dS_y \quad (11)$$

$$B_i^m(\mathbf{x}) = \frac{\rho^{-m}}{L} \sum_{l=0}^{L-1} \int_S \hat{H}(\mathbf{x}, \mathbf{y}, s_l) \phi_i(\mathbf{y}) e^{-\frac{2\pi i m l}{L}} dS_y \quad (12)$$

where  $s_l$  is given by  $s_l = \delta(\zeta_l)/(c\Delta t)$ . In addition, the parameter  $\rho$  has to be  $\rho < 1$  and is taken as  $\rho^L = \sqrt{\epsilon}$  where  $\epsilon$  shows the assumed error in the computation of eq(11) and eq(12). To determine  $\delta(\zeta_l)$ , we use the backward differential formula (BDF) of order two as follows:

$$\delta(\zeta) = (1 - \zeta) + \frac{(1 - \zeta^2)}{2}. \quad (13)$$

Note that eq(11) and eq(12) are identical to the discrete Fourier transform. Therefore, the calculations of eq(4) can be evaluated by means of the FFT algorithm. Applying the Laplace transforms

$$F(s) = \int_0^{\infty} f(t)e^{-st} dt \quad (14)$$

to the time-domain fundamental solutions  $G(\mathbf{x}, \mathbf{y}, t)$  and  $H(\mathbf{x}, \mathbf{y}, t)$  yields the Laplace domain fundamental solutions  $\hat{G}(\mathbf{x}, \mathbf{y}, s)$  and  $\hat{H}(\mathbf{x}, \mathbf{y}, s)$  as follows:

$$\hat{G}(\mathbf{x}, \mathbf{y}, s) = \frac{1}{2\pi} K_0(sr), \hat{H}(\mathbf{x}, \mathbf{y}, s) = -\frac{s}{2\pi} \frac{\partial r}{\partial n_y} K_1(sr) \quad (15)$$

where  $s$  is the Laplace parameter. Moreover,  $K_n$  is the modified Bessel function of the second kind in eq(15).

It is difficult to apply the time-domain BEM based on the OQM to a large scale problem with the large number of  $N$  because the required computational complexity and memory become  $O(LM^2N)$  and  $O(M^2L)$  in eq(10), respectively. Therefore, the time-domain OQ-BEM is accelerated by the Fast Multipole Method (FMM) in this research.

#### TIME-DOMAIN FAST MULTIPOLE BEM FORMULATION BASED ON THE OQM

The FMM proposed by Greengard and Rokhlin is a technique to reduce the computational time and memory for a large scale problem. In recent years, Fast Multipole BEM, which is the coupling method of BEM and FMM, has been developed to improve the computational efficiency for various large scale problems in many engineering fields, e.g., the 2-D Helmholtz problem[11] and the 3-D sound and environmental vibration problems[12]. Since FMBEM algorithm has been described in detail in other published papers (for example, see the paper of Nishimura[13]), we will summarize only the essential formulas here.

We consider a point  $\mathbf{o}$  near the source point  $\mathbf{y}$ . Locations of field point  $\mathbf{x}$  and source point  $\mathbf{y}$  are expressed as  $(r, \theta)$  and  $(\rho, \phi)$ , respectively in polar coordinate system originated at the point  $\mathbf{o}$ . Using the Graf's addition theorem, we obtain the following multipole expansion of the fundamental solution

$$\hat{G}(\mathbf{x}, \mathbf{y}, s) = \frac{1}{2\pi} \sum_{n=-\infty}^{\infty} M_n K_n(sr) e^{in\theta} \quad (16)$$

where the coefficient  $M_n$  is called the multipole moment, which is given by

$$M_n^G = I_n(s\rho) e^{-in\phi}. \quad (17)$$

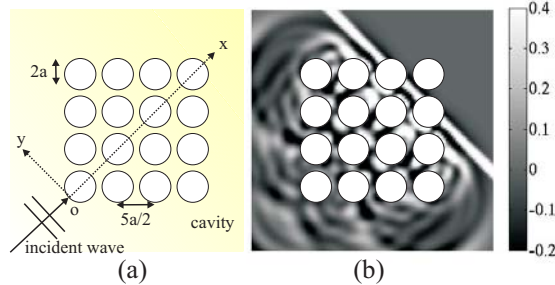


Figure 1 A Scattering problem by cavities. (a): scattering model (b): total displacement field at  $t = 5.25T_0$ .

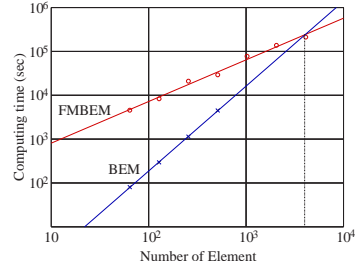


Figure 2 Comparison of CPU time between conventional BEM and FMBEM based on the OQM.

Similarly, the multipole moment  $M_n^H$  for  $H(\mathbf{x}, \mathbf{y})$  is obtained from eq(15) as follows: Once the multipole moments are obtained, we can quickly evaluate the matrix-vector products of the discretized integral equation (10) using the fast multipole algorithm[9]. The translation formulas (M2M, M2L and L2L) are also derived from the Graf's addition theorem of the fundamental solutions defined in eq(15).

The modified bessel function  $I_n(z)$  tends exponentially to infinity for large argument  $z$ . This fact sometimes causes the instability of the translation formulas when the cell size is large. To overcome the problem, we introduced the scaling of the multipole and local expansion coefficients.

**NUMERICAL EXAMPLES**

The fast multipole BEM based on the operational quadrature method is applied to analyze the transient behaviours of scatterers with radius  $a$  as shown in Fig. 1-(a). The boundary conditions of each scatterer are supposed to be  $\partial u / \partial n = 0$  on the boundary. The number of element is 1024. The parameters  $N$  and  $L$  are given by  $N = L = 128$  in eq(10)-(12). The displacement of the incident plane wave is given by

$$u_{in}(\mathbf{x}, t) = 1 - \cos 2\pi \langle (t - \frac{x+a}{c}) / T_0 \rangle, \begin{cases} \langle \alpha \rangle = \alpha & \text{for } 0 \leq \alpha \leq 1 \\ \langle \alpha \rangle = 0 & \text{otherwise} \end{cases} \quad (18)$$

Fig. 1-(b) shows the total wave fields at time  $t = 5.25T_0$ . We can see that scattered waves are generated by the interaction of incident wave and each cavity. Fig. 2 shows the CPU time needed in order to solve a scattering problem by the single scatterer using conventional time-domain BEM or time-domain FMBEM based on the OQM when the number of element is 64, 128, 256, 512, 1024, 2048 and 4096. Because of the restriction of the memory, it was not possible to solve the case that the number of element is 1024 or more with conventional BEM. We can see that the FMBEM based on the OQM is faster than the conventional BEM when the number of element is 3000 or more as shown in Fig. 2.

Thus, time-domain FMBEM based on the OQM is very effective in aspect of the computational time for a large scale problem.

## CONCLUSIONS

In this paper, the time-domain fast multipole BEM formulation using OQM was developed for 2-D scalar wave propagation problem. The convolution integrals were discretized based on the OQM in time coordinate and fundamental solutions in Laplace domain were used for the calculations of influence functions. The fast multipole method was applied to accelerate the calculations of matrix-vector products. As numerical examples, scattering problems by scatterers were demonstrated and the computational efficiency of the proposed method was confirmed. In near future, we will develop the time-domain FMBEM based on the OQM for 3-D Helmholtz problem and 2-D elastodynamics.

## Acknowledgement

This work is supported by the Japan Society of the Promotion of Science.

## References

- [1] W. J. Mansur and C. A. Brebbia *Transient elastodynamics using a time-stepping technique*, In: *Boundary Elements*, C. A. Brebbia, T. Futagami and M. Tanaka (Eds), 677-698 (1983).
- [2] S. Hirose *Boundary Integral equation method for transient analysis of 3-D cavities and inclusions*, *Engineering analysis with Boundary Elements*, vol.8, No.3, 146-153 (1991).
- [3] C. Lubich *Convolution quadrature and discretized operational calculus I*, *Numer. Math.*, **52**, 129-145 (1988).
- [4] C. Lubich *Convolution quadrature and discretized operational calculus II*, *Numer. Math.*, **52**, 413-425 (1988).
- [5] C. Lubich *On the multistep time discretization of linear initial boundary value problems and their boundary integral equations*, *Numer. Math.*, **67**, 365-389 (1994).
- [6] A. I. Abreu, J. A. M. Carrer and W. J. Mansur *Scalar wave propagation in 2D: a BEM formulation based on the operational quadrature method*, *Engineering analysis with Boundary Elements*, 27, 101-105 (2003).
- [7] M. Schanz and V. Struckmeier *Wave propagation in a simplified modelled poroelastic continuum: Fundamental solutions and a time domain boundary element formulation*, *Numer. Math.*, **64**, 1816-1839 (2005).
- [8] Ch. Zhang *Transient elastodynamic antiplane crack analysis of anisotropic solids*, *Int. J. Solids and Structures*, vol. 37, 6107-6130 (2006).
- [9] L. Greengard and V. Rokhlin *A fast algorithm for particle simulations*, *Journal of Computational Physics*, **73**, 325-348 (1987).
- [10] S. Kobayashi *Wave Analysis and Boundary Element Methods*, Kyoto University Press (in Japanese), (2000).
- [11] T. Fukui and J. Katsumoto *Fast multipole algorithm for two dimensional Helmholtz equation and its application to boundary element method*. *Proc of the 14th Japan National Symposium on Boundary Element Methods (in Japanese)*, 81-86 (1997).
- [12] T. Saitoh *A study on effective 3-D numerical analysis of environmental vibration and noise induced by a moving train*, doctoral thesis in Tokyo Institute of Technology, (2006).
- [13] N. Nishimura, *Fast multipole accelerated boundary integral equation methods*, *Appl. Mech. Rev.*, **55**, 299-324 (2002).

## Postbuckling Analysis of Shear Deformable Shallow Shells by BEM

P.M. Baiz and M.H. Aliabadi

Department of Aeronautical Engineering, Imperial College London  
South Kensington campus, London SW7 2AZ

**Keywords:** Postbuckling, Shear Deformable, Shallow Shell Theory.

**Abstract.** In this paper the post buckling behaviour of shallow shells with a boundary element formulation is studied. Nonlinear boundary integral equations are solved using an incremental approach, where loads and prescribed boundary conditions are applied in small but finite increments. The resulting system of equations are solved using a purely incremental technique and the Newton Raphson technique. In the case of snap buckling a special numerical technique known as the Arc length method is also implemented in order to handle difficulties at limit points. Results from the proposed BEM formulation are compared with other numerical and analytical solutions, and good agreement is obtained.

**Introduction.** Large deflection and postbuckling analysis of shells by BEM using classical (Kirchhoff) theory has been investigated by Kamiya and Sawaki [5], Tosaka and Miyake [11] and Zhang and Atluri [12]. This last one, presenting the first comprehensive work dealing with snap through in thin shallow shells using the arc length method. Lin and Long [6] also presented several snap through examples in shallow shell, based on displacements rather than stress functions. In terms of large deflection of shear deformable theory, the only work available has been presented recently by Dirgantara and Aliabadi [4] while to the best knowledge of the authors no work on postbuckling analysis of shear deformable shallow shells by BEM has been presented. In this work, the BEM formulation presented by the authors in [2] is extended for the postbuckling analysis of shear deformable shallow shells.

**Governing Equations.** Consider an isotropic linear elastic shallow shell of uniform thickness  $h$ , Young's modulus  $E$ , Poisson's ratio  $\nu$ , and a quadratic middle surface with principal curvatures given by  $k_{11} = 1/R_1$  and  $k_{22} = 1/R_2$  ( $k_{12} = k_{21} = 0$ ). The generalized displacements are denoted as  $w_i$  and  $u_\alpha$ , where  $w_\alpha$  denotes the change of the slope of the normal to the middle surface,  $w_3$  denotes the out-of-plane displacement normal to the middle surface and  $u_\alpha$  denotes in-plane displacements of the middle surface. Generalized tractions are denoted as  $p_i$  (out-of-plane tractions) and  $t_\alpha$  (in-plane tractions).

Strains for geometrically nonlinear shallow shell theory can be obtained by considering the geometrical changes of a differential element. The membrane strain resultant tensor can be expressed as follows:

$$\varepsilon_{\alpha\beta} = \frac{1}{2}(u_{\alpha,\beta} + u_{\beta,\alpha}) + w_3 k_{\alpha\beta} + \left[ \frac{1}{2} w_{3,\alpha} w_{3,\beta} \right] \quad (1)$$

while transversal and flexural strain tensors are given as:

$$\gamma_{\alpha 3} = w_\alpha + w_{3,\alpha} \quad (2)$$

$$\kappa_{\alpha\beta} = 2\chi_{\alpha\beta} = w_{\alpha,\beta} + w_{\beta,\alpha} \quad (3)$$

Equilibrium equations for geometrically nonlinear shallow shell analysis are given as follows:

$$M_{\alpha\beta,\beta} - Q_\alpha = 0 \quad (4)$$

$$Q_{\alpha,\alpha} - k_{\alpha\beta} N_{\alpha\beta} + \left[ (N_{\alpha\beta} w_{3,\beta})_{,\alpha} \right] + q_3 = 0 \quad (5)$$

$$N_{\alpha\beta,\beta} + q_\alpha = 0 \quad (6)$$

where  $M_{\alpha\beta}$ ,  $Q_\alpha$  and  $N_{\alpha\beta}$  are the bending, shear and normal stress resultants respectively,  $q_i$  are the body forces. Nonlinear terms in the equilibrium (4-6) and kinematic (1-3) equations are given by the terms in square brackets.

Stress-Strain relations are based on Reissner's variational theorem [9] and can be written in terms of displacement as follows:

$$M_{\alpha\beta} = D \frac{1-\nu}{2} \left( w_{\alpha,\beta} + w_{\beta,\alpha} + \frac{2\nu}{1-\nu} w_{\gamma,\gamma} \delta_{\alpha\beta} \right); \quad (7)$$

$$Q_\alpha = C(w_\alpha + w_{3,\alpha}); \quad (8)$$

and

$$N_{\alpha\beta} = N_{\alpha\beta}^{(i)} + N_{\alpha\beta}^{(ii)} + N_{\alpha\beta}^{(n)} \quad (9)$$

in order to make the representation more convenient, the term  $N_{\alpha\beta}$  is separated into the linear  $N_{\alpha\beta}^{(i)}$  ( $= N_{\alpha\beta}^{(i)} + N_{\alpha\beta}^{(ii)}$ ) and nonlinear parts  $N_{\alpha\beta}^{(n)}$ :

$$\begin{aligned} N_{\alpha\beta}^{(i)} &= B \frac{1-\nu}{2} \left( u_{\alpha,\beta} + u_{\beta,\alpha} + \frac{2\nu}{1-\nu} u_{\gamma,\gamma} \delta_{\alpha\beta} \right); & N_{\alpha\beta}^{(ii)} &= B [(1-\nu)k_{\alpha\beta} + \nu\delta_{\alpha\beta}k_{\phi\phi}] w_3; \\ N_{\alpha\beta}^{(n)} &= \left[ B \frac{1-\nu}{2} \left( w_{3,\alpha} w_{3,\beta} + \frac{\nu}{1-\nu} w_{3,\gamma} w_{3,\gamma} \delta_{\alpha\beta} \right) \right] \end{aligned}$$

where  $D(= Eh^3 / [12(1-\nu^2)])$  is bending stiffness of the shell;  $C(= [D(1-\nu)\lambda^2] / 2)$  is shear stiffness;  $B(= Eh / (1-\nu^2))$  is tension stiffness;  $\lambda = \sqrt{10}/h$  is called the shear factor.

**Boundary Integral Formulation.** The boundary integral equations for bending and transverse shear stress resultants of a boundary source point are derived by using the weighted residual method as shown in Dirgantara [4]:

$$c_{ij} w_j + \int_{\Gamma} P_{ij}^* w_j d\Gamma = \int_{\Gamma} W_{ij}^* p_j d\Gamma + \int_{\Omega} W_{i3}^* f_3^b d\Omega \quad (10)$$

The body force term  $f_3^b$  in equation (10) is given by:

$$f_3^b = q_3 - k_{\alpha\beta} N_{\alpha\beta} + \left[ (N_{\alpha\beta} w_{3,\beta})_{,\alpha} \right] \quad (11)$$

This body force term (11) includes the geometrically nonlinear effect (term in square brackets), in the same way as the nonlinear equilibrium equation (5). After introducing  $f_3^b$  from equation (11) in equation (10), and using the expression for membrane stresses given by equation (9), the following integral equation can be obtained:

$$\begin{aligned} c_{ij} w_j + \int_{\Gamma} P_{ij}^* w_j d\Gamma &= \int_{\Gamma} W_{ij}^* p_j d\Gamma - \int_{\Omega} W_{i3}^* k_{\alpha\beta} B \frac{1-\nu}{2} \left[ u_{\alpha,\beta} + u_{\beta,\alpha} + \frac{2\nu}{1-\nu} u_{\phi,\phi} \delta_{\alpha\beta} \right] d\Omega + \int_{\Omega} W_{i3}^* q_3 d\Omega \\ &- \int_{\Omega} W_{i3}^* k_{\alpha\beta} B ((1-\nu)k_{\alpha\beta} + \nu\delta_{\alpha\beta}k_{\phi\phi}) w_3 d\Omega - \int_{\Omega} W_{i3}^* k_{\alpha\beta} N_{\alpha\beta}^{(n)} d\Omega + \int_{\Omega} W_{i3}^* (N_{\alpha\beta} w_{3,\beta})_{,\alpha} d\Omega \end{aligned} \quad (12)$$

In the same way, the boundary integral equation related to the governing equations for membrane stress resultants of a boundary source point can be written as [4]:

$$c_{\theta\alpha} u_\alpha + \int_{\Gamma} T_{\theta\alpha}^* u_\alpha d\Gamma = \int_{\Gamma} U_{\theta\alpha}^* t_\alpha^{(i)} d\Gamma + \int_{\Omega} U_{\theta\alpha}^* f_\alpha^m d\Omega \quad (13)$$

where  $f_\alpha^m$  and  $t_\alpha^{(i)}$  are given as:

$$f_\alpha^m = N_{\alpha\beta,\beta}^{(ii)} + \left[ N_{\alpha\beta,\beta}^{(n)} \right] + q_\alpha; \quad t_\alpha^{(i)} = t_\alpha - t_\alpha^{(ii)} - t_\alpha^{(n)} = N_{\alpha\beta} n_\beta - N_{\alpha\beta}^{(ii)} n_\beta - N_{\alpha\beta}^{(n)} n_\beta \quad (14)$$

using equations (14), equation (13) can be rewritten as follows:

$$c_{\theta\alpha}u_\alpha + \int_\Gamma T_{\theta\alpha}^{*(i)}u_\alpha d\Gamma + \int_\Gamma U_{\theta\alpha}^*B[k_{\alpha\beta}(1-\nu) + \nu\delta_{\alpha\beta}k_{\phi\phi}]w_{3,\beta}d\Gamma - \int_\Omega U_{\theta\alpha}^*B[k_{\alpha\beta}(1-\nu) + \nu\delta_{\alpha\beta}k_{\phi\phi}]w_{3,\beta}d\Omega - \int_\Omega U_{\theta\alpha}^*N_{\alpha\beta}^{(n)}d\Omega + \int_\Gamma U_{\theta\alpha}^*N_{\alpha\beta}^{(n)}n_\beta d\Gamma = \int_\Gamma U_{\theta\alpha}^*t_\alpha d\Gamma + \int_\Omega U_{\theta\alpha}^*q_\alpha d\Omega \quad (15)$$

where  $W_{ij}^*$ ,  $P_{ij}^*$  and  $U_{\theta\alpha}^*$ ,  $T_{\theta\alpha}^{*(i)}$  are fundamental solutions [1]. Equations (12) and (15) represent a set of five boundary integral equations. Equations in (12) are for rotations and out-of-plane displacement while equations in (15) are for in-plane displacements.

**Domain Nonlinear Terms.** Nonlinear terms in equations (12) and (15) include primarily derivatives of the out-of-plane displacement  $w_{3,\beta}$  and total membrane stress resultants  $N_{\alpha\beta}$  at domain points. These nonlinear terms are needed in order to solve the nonlinear system of equations. These terms can be derived from the displacement integral equations (12) and (15) as follows:

$$w_{3,\theta} + \int_\Gamma P_{3j,\theta}^*w_j d\Gamma = \int_\Gamma W_{3j,\theta}^*p_j d\Gamma - \int_\Omega W_{33,\theta}^*k_{\alpha\beta}B\frac{1-\nu}{2}\left[u_{\alpha,\beta} + u_{\beta,\alpha} + \frac{2\nu}{1-\nu}u_{\phi,\phi}\delta_{\alpha\beta}\right]d\Omega - \int_\Omega W_{33,\theta}^*k_{\alpha\beta}B((1-\nu)k_{\alpha\beta} + \nu\delta_{\alpha\beta}k_{\phi\phi})w_{3,\beta}d\Omega - \int_\Omega W_{33,\theta}^*k_{\alpha\beta}N_{\alpha\beta}^{(n)}d\Omega + \int_\Omega W_{33,\theta}^*(N_{\alpha\beta}w_{3,\beta})_{,\alpha}d\Omega + \int_\Omega W_{33,\theta}^*q_3 d\Omega \quad (16)$$

In the same way, linear membrane stresses  $N_{\alpha\beta}^{(l)}$  can be obtained after the derivative of equation (15) with respect to the source point, is introduced in equation (9), resulting in the following integral equation:

$$N_{\alpha\beta}^{(l)} + \int_\Gamma T_{\alpha\beta\gamma}^{(i)*}u_\gamma d\Gamma = \int_\Gamma U_{\alpha\beta\gamma}^*t_\gamma d\Gamma - \int_\Gamma U_{\alpha\beta\gamma}^*B[k_{\gamma\theta}(1-\nu) + \nu\delta_{\gamma\theta}k_{\phi\phi}]w_{3,\theta}d\Gamma + \int_\Omega U_{\alpha\beta\gamma}^*B[k_{\gamma\theta}(1-\nu) + \nu\delta_{\gamma\theta}k_{\phi\phi}]w_{3,\theta}d\Omega - \int_\Gamma U_{\alpha\beta\gamma}^*N_{\gamma\theta}^{(n)}n_\theta d\Gamma + \int_\Omega U_{\alpha\beta\gamma}^*N_{\gamma\theta}^{(n)}d\Omega + \int_\Omega U_{\alpha\beta\gamma}^*q_\gamma d\Omega + B[(1-\nu)k_{\alpha\beta} + \nu\delta_{\alpha\beta}k_{\phi\phi}]w_3 \quad (17)$$

Due to the way in which the nonlinear integral equations are solved in the present work (incremental solution strategy), equations (16) and (17) will add 5 extra degrees of freedom (3 linear membrane stresses  $N_{\alpha\beta}^{(l)}$  and 2 out-of-plane derivatives  $w_{3,\beta}$ ) at every domain point. Therefore, in order to reduce this large system of equations,  $N_{\alpha\beta}$  and  $w_{3,\beta}$  are also expressed in terms of basic displacements fields ( $u_\alpha$  and  $w_3$ ) by using radial basis functions.

Using radial basis functions [8], derivatives of the out-of-plane displacement and membrane stresses can be represented as:

$$w_{3,\beta} = \mathbf{f}(r)_{,\beta}\mathbf{F}^{-1}w_3 \quad (18)$$

and,

$$N_{\alpha\beta}^{(i)} = B\frac{1-\nu}{2}\left[\mathbf{f}(r)_{,\beta}\mathbf{F}^{-1}u_\alpha + \mathbf{f}(r)_{,\alpha}\mathbf{F}^{-1}u_\beta + \frac{2\nu}{1-\nu}\mathbf{f}(r)_{,\gamma}\mathbf{F}^{-1}u_\gamma\delta_{\alpha\beta}\right] \quad (19)$$

$$N_{\alpha\beta}^{(ii)} = B[(1-\nu)k_{\alpha\beta} + \nu\delta_{\alpha\beta}k_{\phi\phi}]w_3 \quad (20)$$

$$N_{\alpha\beta}^{(n)} = B\frac{1-\nu}{2}\left[\mathbf{f}(r)_{,\alpha}\mathbf{F}^{-1}w_3\mathbf{f}(r)_{,\beta}\mathbf{F}^{-1}w_3 + \frac{\nu}{1-\nu}\mathbf{f}(r)_{,\gamma}\mathbf{F}^{-1}w_3\mathbf{f}(r)_{,\gamma}\mathbf{F}^{-1}w_3\delta_{\alpha\beta}\right] \quad (21)$$

**Solution Strategy.** Before nonlinear equations (12), (15), (16) and (17) are discretized, all variables should be expressed in terms of incremental quantities. In this incremental solution strategy, loads and prescribed displacements are applied in small but finite increments as follows,

$$w_i^{k+1} = w_i^k + \Delta w_i; \quad u_\alpha^{k+1} = u_\alpha^k + \Delta u_\alpha; \quad etc. \quad (22)$$

where increments are denoted by  $\Delta$ , and known values of the  $k$ th step are denoted by the superscript ' $k$ '.

The bending and out-of-plane displacement integral equation (12) can be written in an incremental form as follows:

$$\begin{aligned} c_{ij} (w_j^k + \Delta w_j) + \int_{\Gamma} P_{ij}^* (w_j^k + \Delta w_j) d\Gamma = \int_{\Gamma} W_{ij}^* (p_j^{*k} + \Delta p_j^*) d\Gamma - \int_{\Gamma} W_{i3}^* k_{\alpha\beta} B \frac{1-\nu}{2} \\ \left[ (u_\alpha^k + \Delta u_\alpha)_{,\beta} + (u_\beta^k + \Delta u_\beta)_{,\alpha} + \frac{2\nu}{1-\nu} (u_\gamma^k + \Delta u_\gamma)_{,\gamma} \delta_{\alpha\beta} \right] d\Omega \\ - \int_{\Omega} W_{i3}^* k_{\alpha\beta} (N_{\alpha\beta}^{(n)k} + \Delta N_{\alpha\beta}^{(n)}) d\Omega - \int_{\Omega} W_{i3}^* k_{\alpha\beta} B [(1-\nu)k_{\alpha\beta} + \nu\delta_{\alpha\beta}k_{\gamma\gamma}] (w_3^k + \Delta w_3) d\Omega \\ - \int_{\Omega} W_{i3}^* \left( (N_{\alpha\beta}^k + \Delta N_{\alpha\beta}) (w_3^k + \Delta w_3)_{,\beta} \right)_{,\alpha} d\Omega + \int_{\Omega} W_{i3}^* (q_3^k + \Delta q_3) d\Omega \end{aligned} \quad (23)$$

Membrane stresses can be expanded as follows:

$$\begin{aligned} N_{\alpha\beta}^k &= N_{\alpha\beta}^{(i)k} + N_{\alpha\beta}^{(ii)k} + N_{\alpha\beta}^{(n)k}; & \Delta N_{\alpha\beta} &= \Delta N_{\alpha\beta}^{(i)} + \Delta N_{\alpha\beta}^{(ii)} + \Delta N_{\alpha\beta}^{(n)}; \\ N_{\alpha\beta}^{(l)k} &= N_{\alpha\beta}^{(i)k} + N_{\alpha\beta}^{(ii)k}; & \Delta N_{\alpha\beta}^{(l)} &= \Delta N_{\alpha\beta}^{(i)} + \Delta N_{\alpha\beta}^{(ii)}; \\ N_{\alpha\beta}^{(i)k} &= B \frac{1-\nu}{2} \left( u_{\alpha,\beta}^k + u_{\beta,\alpha}^k + \frac{2\nu}{1-\nu} u_{\gamma,\gamma}^k \delta_{\alpha\beta} \right); & N_{\alpha\beta}^{(ii)k} &= B [(1-\nu)k_{\alpha\beta} + \nu\delta_{\alpha\beta}k_{\phi\phi}] w_3^k; \\ \Delta N_{\alpha\beta}^{(i)} &= B \frac{1-\nu}{2} \left( \Delta u_{\alpha,\beta} + \Delta u_{\beta,\alpha} + \frac{2\nu}{1-\nu} \Delta u_{\gamma,\gamma} \delta_{\alpha\beta} \right); & \Delta N_{\alpha\beta}^{(ii)} &= B [(1-\nu)k_{\alpha\beta} + \nu\delta_{\alpha\beta}k_{\phi\phi}] \Delta w_3; \\ \Delta N_{\alpha\beta}^{(n)} &= B \frac{1-\nu}{2} \left( w_{3,\alpha}^k \Delta w_{3,\beta} + \Delta w_{3,\alpha} w_{3,\beta}^k + \frac{2\nu}{1-\nu} w_{3,\gamma}^k \Delta w_{3,\gamma} \delta_{\alpha\beta} + \text{higher order} \right); \\ N_{\alpha\beta}^{(n)k} &= B \frac{1-\nu}{2} \left( w_{3,\alpha}^k w_{3,\beta}^k + \frac{\nu}{1-\nu} w_{3,\gamma}^k w_{3,\gamma}^k \delta_{\alpha\beta} \right) \end{aligned} \quad (24)$$

Due to the fact that loads and prescribed displacements are applied in small increments and higher order terms of the incremental quantities ( $\Delta N_{\alpha\beta} \Delta w_{3,\beta}$ ;  $\Delta w_{3,\alpha} \Delta w_{3,\beta}$ ; *etc*) are ignored, a purely incremental solution strategy in which increments are obtained and added to the  $k$ th state without the need of an iterative process can be used.

The arc length method, also known as Riks method, is a numerical technique which solves simultaneously for loads and displacements using a load parameter as an additional unknown. The basic idea is to use a scalar "arc length"  $\Delta l$  along the static equilibrium path in the load-displacement space to control the progress of the solution, thus, unloading is automatically accommodated in tracing the equilibrium path. This means that solutions can be provided regardless of whether the response is stable or unstable. In the present work, the modified Riks method [3] and the standard "displacement control" algorithm were implemented in order to deal with unstable equilibrium paths.

**Numerical Example.** This example presents a hinged free point loaded cylindrical panel shown in Figure 1. The results by Palazotto and Dennis [7] and Sabir and Lock [10] are used for comparison. General shell dimension are also given in Figure 1 and material properties are given by,  $E$  and Poisson ratio  $\nu = 0.3$ . The boundary conditions are hinge ( $w_3 = u_\alpha = 0$ ) for the flat sides of the panel and totally free ( $w_i \neq 0$  and  $u_\alpha \neq 0$ ) for the curved sides. The mesh used by Sabir and Lock [10] contains 4x4 quadratic quadrilateral isoparametric elements for just one quarter of the geometry and the mesh

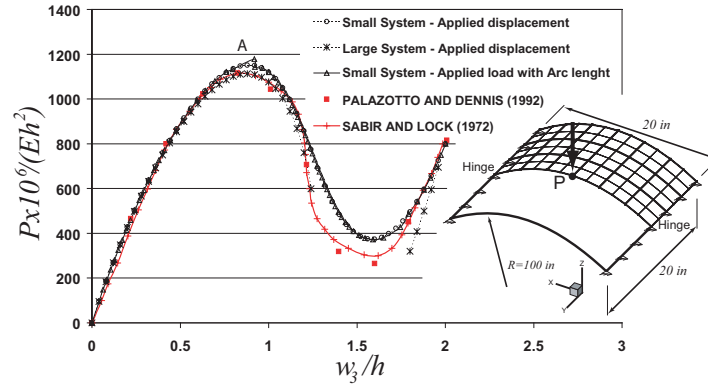


Figure 1: Point loaded hinge-free cylindrical shallow shell.

used in [7] contains 4x6 quadratic quadrilateral isoparametric elements also for just one quarter of the shallow shell. The BEM mesh use 18 domain cells and 18 boundary elements to model half of the geometry. In Figure 1, Large System refers to the nonlinear system that uses equations (16) and (17) while Small System uses equations (19)-(21).

Because of expected snap through (limit points in the load displacement response, point A in Figure 1), not only applied concentrated force is considered in the analysis, but also a central displacement incrementation. Figure 1 shows how BEM solutions with applied purely incremental displacement can overcome this numerical difficulty. Also in Figure 1 the arc length technique is used with applied incremental load, in fact it is clear how this solution overlaps the nonlinear response obtained with the purely incremental displacement technique; with the important difference that the CPU time in the arc length solution was more than 50 times larger than the purely incremental one.

**Conclusion.** In this work, boundary element formulations for the postbuckling analysis of shear deformable shallow shells was presented. Two different sets of nonlinear boundary integral equations were studied. The difference between sets is based on the determination of nonlinear domain terms: one with five extra boundary integral equations (16) and (17), and the other which uses radial basis functions, equations (19)-(21). Both nonlinear systems of equations were solved using an incremental solution strategy, where loads and displacements are applied in small but finite increments. Higher order terms were ignored, resulting in linearized system of equations. Because of this linearization a purely incremental solution algorithm was also used. Due to the presence of limit points in some nonlinear responses (unstable post-buckling), the arc length method was implemented with the full Newton Raphson technique. The purely incremental solution algorithm was more time efficient than the iterative approach.

**Acknowledgement.** This work was supported by the Department of Aeronautical Engineering, Imperial College London.

## References

- [1] Aliabadi, M.H., *The Boundary Element Method, vol II: application to solids and structures*, Chichester, Wiley (2001).
- [2] Baiz, P.M., Aliabadi, M. H., *Large Deflection Analysis of Shear Deformable Shallow Shells by the Field Boundary Element Method*, *Boundary Element Technique* (2005).

- [3] Crisfield, M.A., A Fast incremental iterative solution procedure that handles "Snap-Through", *Computers & Structures*, **13**, 55-62 (1981).
- [4] Dirgantara, T., Aliabadi, M. H., A boundary element formulation for geometrically nonlinear analysis of shear deformable shells, *Computer Methods in Applied Mechanics and Engineering*, **195**, 4635-4654 (2006).
- [5] Kamiya, N., Sawaki, Y., Boundary element method applied to finite deflections of shallow elastic shells, *Methodes Numeriques de l'Ingenieur, Comptes Rendus du Troisieme Congres International*, 63-76 (1983).
- [6] Lin, J., Long S., Geometrically nonlinear analysis of the shallow shell by the displacement-based boundary element formulation, *Engineering Analysis with Boundary Elements*, **18**, 63-70, (1996).
- [7] Palazotto, A., Dennis, S., *Nonlinear Analysis of Shells Structures*, AIAA Education Series, Inc. Washington, D.C. (1992).
- [8] Purbolaksono, J., Aliabadi, M.H., Large deformation of shear deformable plates by the boundary-element method, *Journal of Engineering Mathematics*, **51**, 211-230, (2005).
- [9] Reissner, E., On a Variational Theorem in Elasticity, *Journal of Mathematics and Physics*, **29**, 90-95 (1950).
- [10] Sabir, A.B., and Lock, A.C., The Application of Finite Elements to the Large Deflection Geometrically Nonlinear Behaviour of Cylindrical Shells, *Variational Methods in Engineering*, (C.A. Brebbia and H. Tottenham, eds.), Southampton Press, UK (1972).
- [11] Tosaka, N., Miyake, S., Nonlinear analysis of elastic shallow shells by boundary element method, *Boundary Elements VII*, C. A. Brebbia (Ed.), Springer-Verlag, Berlin, 4-43/4-52 (1985).
- [12] Zhang, J.D., Atluri, S.N., Post-buckling analysis of shallow shells by the field-boundary element method, *International Journal for Numerical Methods in Engineering*, **26**, 571-587 (1988).

## Determination of Weight Functions for the Elastic $T$ -stress in Two-Dimensional Anisotropy using BEM.

P.D. Shah<sup>1</sup>, C.L. Tan<sup>1\*</sup>, X. Wang<sup>1</sup>

<sup>1</sup>Department of Mechanical and Aerospace Engineering, Carleton University, Ottawa, K2S 5B6, Canada.

\*Email: ctan@mae.carleton.ca

**Keywords:**  $T$ -stress, weight functions, anisotropic elasticity, mutual or  $M$ -contour integral, BEM.

**Abstract.** The  $T$ -stress is increasingly being recognized as an important second parameter in fracture mechanics analysis together with the stress intensity factor. In this paper, a weight function approach to obtain this quantity is presented. It has previously been successfully developed for isotropic elasticity and is based on simple reference  $T$ -stress solutions. These reference solutions are obtained using the  $M$ -contour integral with the boundary element method (BEM). The veracity of the approach is demonstrated by several example problems where the numerical  $T$ -stress results calculated from the weight function approach are compared with those directly obtained using the  $M$ -integral method.

### 1. Introduction

The study of cracks in anisotropic solids is important because of their increasing use in engineering industry. In fracture assessments using conventional linear elastic fracture mechanics analysis, the severity of the stresses in the vicinity of the crack tip under mixed mode conditions in two-dimensions is characterized by the stress intensity factors (SIF's),  $K_I$  and  $K_{II}$ . Numerous studies have, however, established the importance of including another parameter for such assessments. This second parameter is the  $T$ -stress and is the leading non-singular term in the Williams series eigenfunction expansion. It provides a measure of the degree of stress constraint at the crack tip.

Various analytical and numerical schemes have been developed over the past several years to evaluate directly the  $T$ -stress in isotropic cracked bodies. Similar developments for cracked anisotropic bodies have, hitherto, remained relatively limited indeed. The weight function method is one of several approaches which have been developed to extract  $T$ -stress in isotropic bodies. It is very efficient for treating crack problems involving complex stress fields. Initially introduced by Bueckner [1] for obtaining the SIF based on the principle of superposition, it provides a relatively simple means of evaluating the  $T$ -stress for any loading condition once the weight functions have been obtained for a particular cracked geometry [2]. As expressed in eq. (1) and illustrated in Fig. 1, the  $T$ -stress for a cracked body under loading by a remote stress field  $Q$  can be expressed as the sum of two  $T$ -stress values. The first one is the  $T$ -stress for the cracked specimen due to a crack face loading, Fig 1(b); this crack face load corresponds to the stress  $\sigma(x)$  produced by the field  $Q$  in the same specimen in the absence of the crack. The  $T$ -stress for this case can be obtained by integrating the product of the stress distribution  $\sigma(x)$  and the weight function  $t(x)$  over the crack face which must first be determined. The second component in the superposition is the equivalent  $T$ -stress in an uncracked geometry under given field  $Q$ , Fig. 1(c). Thus,

$$T = T_{crack\ pressure} + T_{uncracked} \quad (1)$$

where

$$T_{crack\ pressure} = \int_0^a \sigma(x)t(x)dx \quad (2)$$

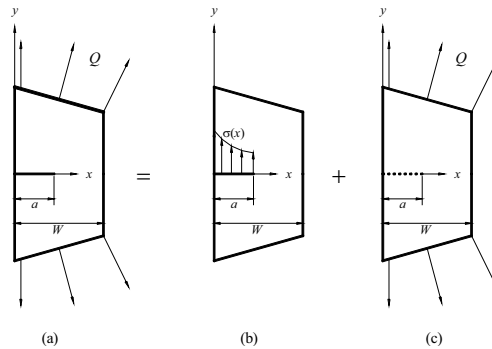


Fig. 1. The superposition principle for  $T$ -stress evaluation.

For isotropic bodies, Sham [3], Fett [4], Fett and Rizzi [5] have obtained weight functions for  $T$ -stresses in a number of cracked geometries; Wang [6, 7] has also developed an efficient methodology to extract the weight functions from reference  $T$ -stress solutions. The corresponding weight function expressions for the evaluation of  $T$ -stress in cracked anisotropic media are, however, extremely scarce indeed. In this paper, Wang's [7] approach of developing weight functions using reference solutions is extended to general anisotropic cracked bodies under mixed mode loading.

## 2. Weight functions for mixed mode loading in anisotropy

For mixed-mode loading, the first term in eq. (2) can be further expanded as,

$$T_{crack\ pressure} = \int_0^a \sigma_{yy}(x) m(x) dx + \int_0^a \tau_{xy}(x) n(x) dx \quad (3)$$

where,  $\sigma_{yy}(x)$  and  $\tau_{xy}(x)$  are the normal and shear stresses, respectively, along the prospective crack plane in an uncracked body under stress field  $Q$ ; and  $m(x)$  and  $n(x)$  are the weight functions for mode I and mode II loadings, respectively. The form for the weight functions  $m(x)$  and  $n(x)$  can be approximated by two-term expressions as follows,

$$m(x) = \frac{2}{\pi a} \left[ D_1 \left(1 - \frac{x}{a}\right)^{\frac{1}{2}} + D_2 \left(1 - \frac{x}{a}\right)^{\frac{3}{2}} \right] \text{ and } n(x) = \frac{2}{\pi a} \left[ D_3 \left(1 - \frac{x}{a}\right)^{\frac{1}{2}} + D_4 \left(1 - \frac{x}{a}\right)^{\frac{3}{2}} \right] \quad (4)$$

where the coefficients  $D_i$  are determined using four reference  $T$ -stress solutions as will be discussed below.

In eq. (2), the  $T$ -stress for an uncracked isotropic body can be expressed as the difference between the direct stresses at the prospective crack-tip position in the uncracked body as, Chen [2],

$$T_{uncracked} = \sigma_{xx} - \sigma_{yy} \Big|_{x=a} \quad (5)$$

Unlike the case of isotropy, the  $T$ -stress for anisotropy also depends on the material properties. Consider the near crack tip stress field in an anisotropic cracked body. Along the crack plane, i.e.  $\theta = 0$ , they are [8],

$$\sigma_{xx} = \frac{K_I}{\sqrt{2\pi r}} \operatorname{Re} \left[ \frac{\mu_1 \mu_2}{\mu_1 - \mu_2} (\mu_2 - \mu_1) \right] + \frac{K_{II}}{\sqrt{2\pi r}} \operatorname{Re} \left[ \frac{1}{\mu_1 - \mu_2} \{ (\mu_2)^2 - (\mu_1)^2 \} \right] + T, \quad (6.a)$$

$$\sigma_{yy} = \frac{K_I}{\sqrt{2\pi r}} \operatorname{Re} \left[ \frac{1}{\mu_1 - \mu_2} (\mu_1 - \mu_2) \right], \quad (6.b)$$

$$\tau_{xy} = \frac{K_{II}}{\sqrt{2\pi r}} \mathbf{Re} \left[ \frac{1}{\mu_1 - \mu_2} (\mu_1 - \mu_2) \right] \tag{6.c}$$

where the quantities,  $\mu_1$  and  $\mu_2$  are the roots of the characteristic equation for a plane anisotropic elastic body in stable equilibrium [9]. They are either complex or purely imaginary mathematical quantities for anisotropic materials. From eqns. (6), the  $T_{uncracked}$  at point  $a$  (the crack tip position in the case of a cracked geometry) can be represented in terms of the stress field as follows,

$$T_{uncracked} = \left[ \sigma_{xx} + \mathbf{Re}(\mu_1\mu_2)\sigma_{yy} + \mathbf{Re}(\mu_1 + \mu_2)\tau_{xy} \right]_{|x=a} \tag{7}$$

**2.1 Reference  $T$ -stress solutions**

It has been noted above that the weight function for a particular crack geometry and material can be derived from a set of four reference  $T$ -stress solutions. To this end, the reference  $T$ -stress solutions can be conveniently chosen to be from those load conditions on the cracked geometry for which there are no contributions to  $T_{uncracked}$ . Thus, two reference solutions can be obtained for the cases when the cracked geometry is subjected to normal crack face loading, and two other solutions can be obtained when it is under shear loads on the crack faces; these correspond to the cracked geometry being under mode I and mode II loading, respectively. In the present work, the following stress distributions are considered for  $\sigma_{yy}(x)$  and  $\tau_{xy}(x)$  applied along the crack faces:

$$\sigma_{yy}(x) = \sigma_o \left( 1 - \frac{x}{a} \right)^n \quad \text{and} \quad \tau_{xy}(x) = \tau_o \left( 1 - \frac{x}{a} \right)^n \tag{8}$$

where  $n = 0$  and  $1$ , which corresponds to uniform and linearly varying loads, respectively. The distance  $x$  in eq. (8) may be defined as shown in Fig. 2, for the single edge cracked plate (SECP), centre cracked plate (CCP) and double edge cracked plate (DECP).

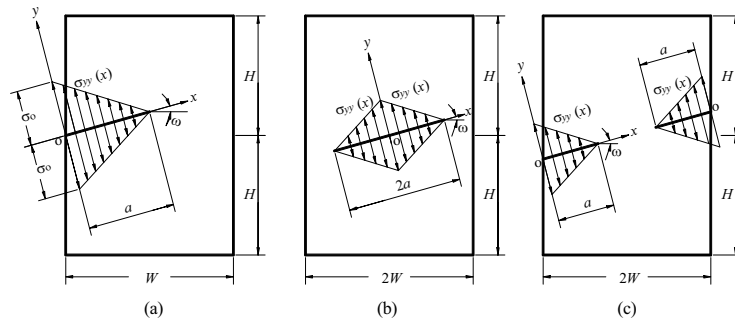


Fig. 2. Normal crack face loading,  $\sigma_{yy}(x)$ , ( $n = 1$ ) for (a) SECP (b) CCP and (c) DECP reference  $T$ -stress solutions.

From eqs. (1), (3), (4) and (8), a set of four of simultaneous equations are obtained which when further processed give the solutions to  $D_i$  terms to evaluate the weight functions  $m(x)$  and  $n(x)$  as follows:

$$\begin{aligned} D_1 &= \left( -\frac{105}{16} \right) \pi T_2 + \left( \frac{75}{16} \right) \pi T_1, & D_2 &= \left( -\frac{105}{16} \right) \pi T_1 + \left( \frac{175}{16} \right) \pi T_2 \\ D_3 &= \left( -\frac{105}{16} \right) \pi T_4 + \left( \frac{75}{16} \right) \pi T_3, & D_4 &= \left( -\frac{105}{16} \right) \pi T_3 + \left( \frac{175}{16} \right) \pi T_4 \end{aligned} \tag{9}$$

In eqs. (9),  $T_1$  and  $T_2$  are the reference  $T$ -stress solutions for normal crack face loading  $\sigma_{yy}(x)$  with  $n = 0$  and 1, respectively; similarly,  $T_3$  and  $T_4$  are the corresponding reference  $T$ -stress solutions for shear crack face loading  $\tau_{xy}(x)$ . For the determination of these reference  $T$ -stress solutions, the conservation  $M$ -contour integral approach in conjunction with the boundary element method (BEM) as developed in [10] for cracked anisotropic bodies, is employed. This will be briefly discussed next.

## 2.2 $M$ -integral method for $T$ -stress in two-dimensional anisotropy

The path independent  $M$ -integral, which is based on the  $J$ -integrals for two independent equilibrium states ( $A$ ) and ( $B$ ), the first being the boundary value problem to be analysed and the second being an auxiliary field solution. The boundary value problem ( $A$ ) corresponds to the analysis conducted using the BEM analysis of the cracked specimen. The auxiliary field ( $B$ ) is chosen to be the solution for a semi-infinite crack loaded by a point force  $f$  at the crack tip in the direction parallel to the crack plane. The solution for state ( $B$ ) is given in [10]. The  $M$ -integral (denoted by  $M$ ), in terms of stress  $\sigma_{ij}$  and displacement derivatives  $\varepsilon_{ij}$  along a contour  $\Gamma_0$  (Fig. 3.a) is given as,

$$M = \int_{\Gamma_0} \left[ (\sigma_{ij}^A \varepsilon_{ij}^B n_1 - \sigma_{ij}^A n_j u_{i,1}^B - \sigma_{ij}^B n_j u_{i,1}^A) \right] d\Gamma \quad (10)$$

Using the fact that  $M$  is bounded, it can be shown [10] that the following relation between the  $T$ -stress and the  $M$ -integral exists:

$$T = M \left( \frac{1}{a_{11}} f \right) \quad (11)$$

In eqn. (11),  $M$  and the first element of the compliance matrix,  $a_{11}$ , are both in the local coordinate system shown in Fig. 3(b).

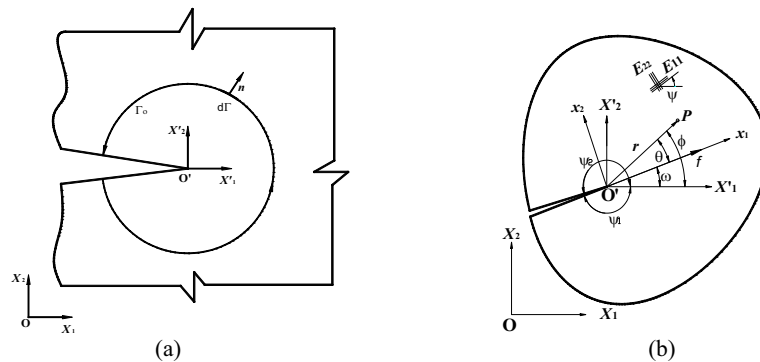


Fig. 3. (a) Contour  $\Gamma_0$  around the crack tip for  $M$ -integral; (b) auxiliary field: a semi-infinite crack subjected to a point force  $f$  at the crack tip.

## 3. Numerical Examples

Two sets of problems are treated here. The first set consists of the single edge-cracked plate (SECP), centre-cracked plate (CCP) and double edge-cracked plate (DECP) specimens subjected to remote tension under plane stress. They are as shown in Fig. 4 with  $H/W = 4$ ,  $a/W = 0.1, 0.2, 0.3, 0.4$  and  $0.5$ . The second problem consists of a crack emanating from a rivet hole in an anisotropic plate subjected to remote tension under plane stress. The anisotropic material for the plates is arbitrarily chosen to be a graphite-epoxy composite with the material properties in the principal directions [11] as  $E_{11} = 144.8$  GPa,  $E_{22} = 11.7$  GPa,  $G_{12} = 9.66$  GPa and  $\nu_{12} = 0.21$ .

For the first set of problems, several angles of inclination of the cracks,  $\omega$ , and the angles of orientation of the material principal axes,  $\psi$ , with respect to the global Cartesian axes were considered. For the sake of brevity, only the results for  $\omega = 45^\circ$  and  $\psi = 0^\circ, 30^\circ$  and  $60^\circ$  are presented here. As can be seen in Fig. 5, the normalised  $T$ -stress solutions obtained using the weight function method are in good agreement with those obtained directly using the  $M$ -integral [10], with the discrepancies being generally less than 2%.

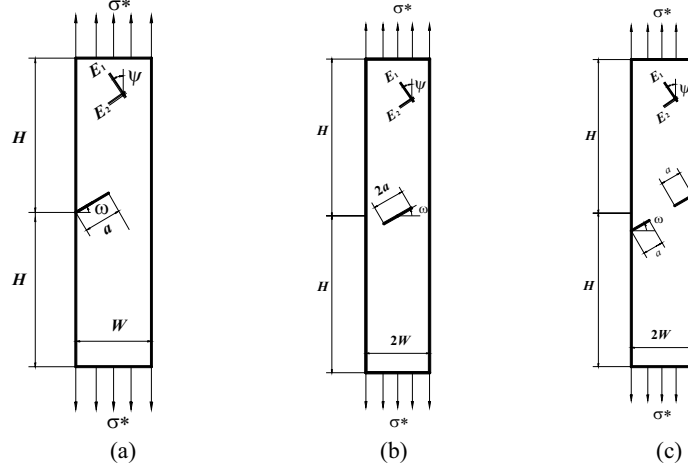


Fig. 4. (a) SECP, (b) CCP, and (c) DECP specimens, and the orientation of principal material axes;  $\omega = 45^\circ$  and  $H/W = 4$  (not to scale)

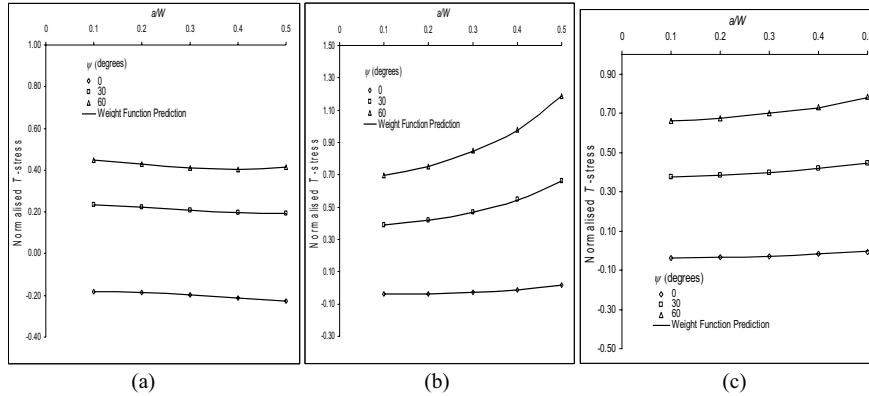


Fig. 5. Variations of normalized  $T$ -stress,  $T/\sigma^*$ , with  $a/W$  for (a) CCP (b) SECP and (c) DECP under remote tension: comparison of weight function solutions with those from direct method for  $\omega = 45^\circ$ .

The second problem considered consists of a stress concentration due to the circular hole as given in Fig. 6(a). The relative crack size,  $a/r$ , is gradually varied from 0.1 to 1.0, within the region where the effect of the stress concentration is pronounced. The radius of the circular hole is taken to be 0.1 times the width of the plate and  $H/W$  is chosen to be 2. Figure 6(b) shows again the good agreement of the normalised  $T$ -stress values obtained using the weight function method with those obtained by the direct method [12], the difference being generally less than 3%.

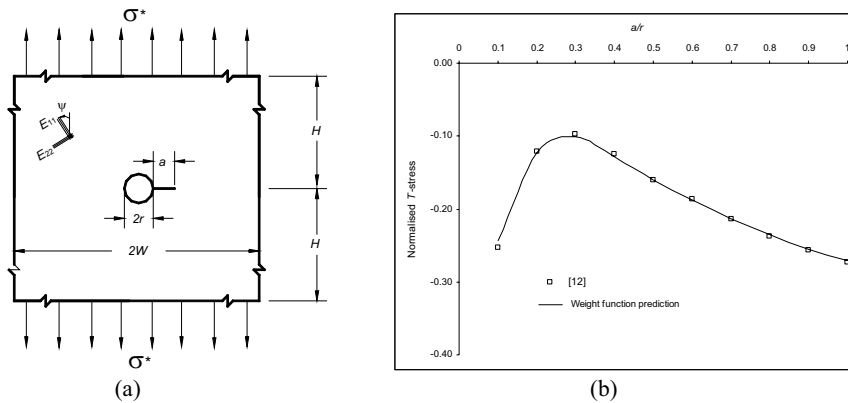


Fig. 6. (a) Plate with a circular hole under remote tension; (b) Variation of normalised  $T$ -stress,  $T/\sigma^*$ , with  $a/r$  for  $\psi = 30^\circ$ .

#### 4. Conclusions

A weight function method based on simple reference solutions for evaluating  $T$ -stress in plane, isotropic, cracked elastic bodies has been successfully extended to the general anisotropic case. The present approach circumvents the need to develop and evaluate relatively complex formulations to obtain the weight functions for two-dimensional anisotropic elasticity. The reference solutions from which the weight functions are derived have been obtained using the  $M$ -contour integral using the BEM. The veracity of the numerical weight functions obtained has been validated by examples. They are the standard CCP, SECP and DECP geometries under remote tension, as well as a case of a plate with a crack emanating from a stress concentration. Comparison of  $T$ -stress results obtained using the weight function approach with those obtained directly using the  $M$ -contour integral with BEM showed excellent agreement indeed.

#### References

- [1] H.F. Bueckner *Zeitschrift für Angewandte Mathematik und Mechanik*, 50, 529-546 (1970).
- [2] Y.Z. Chen *International Journal of Solids and Structures*, 37, 1629-1637 (2000).
- [3] T.L. Sham *International Journal of Fracture*, 48, 81-102 (1991).
- [4] T.A. Fett *Engineering Fracture Mechanics*, 57, 365-373 (1997).
- [5] T.A. Fett and G. Rizzi *International Journal of Fracture*, 132, L9-L16 (2005).
- [6] X. Wang *Engineering Fracture Mechanics*, 69, 1339-1352 (2002).
- [7] X. Wang *Fatigue & Fracture of Engineering Materials & Structures*, 25, 965-973 (2002).
- [8] G.C. Sih, P.C. Paris, G.R. Irwin *International Journal of Fracture Mechanics*, 1, 189-203 (1965).
- [9] S.G. Lekhnitskii *Theory of Elasticity of an Anisotropic Elastic Body*, Holden-Day, San Francisco (1968).
- [10] P.D. Shah, C.L. Tan and X. Wang *Fatigue & Fracture of Engineering Materials & Structures*, 29, 343-356 (2006).
- [11] C.L. Tan and Y.L. Gao *Composite Structures*, 20, 17-28 (1992).
- [12] P.D. Shah, Ch. Song, C.L. Tan and X. Wang. *Structural Durability & Health Monitoring*, 2 (4), 225-237 (2006).

## Simulation of CNT composites using Fast Multipole BEM

Zhenhan Yao<sup>1</sup>, Jundong Xu<sup>1</sup>, Haitao Wang<sup>2</sup> and Xiaoping Zheng<sup>1</sup>

<sup>1</sup>Department of Engineering Mechanics, <sup>2</sup>Institute of Nuclear & New Energy Technology, Tsinghua University, Beijing, 100084 China, Email: demyzh@tsinghua.edu.cn

**Keywords:** Fast multipole BEM; CNT composites; elastic property; thermal property; electric property

**Abstract.** This paper addresses some applications of the fast multipole boundary element method on simulation of the CNT composites, including the simulation of elastic, thermal and electric properties. The carbon nanotubes are treated as effective elastic fibers for the simulation of elastic property, and treated as straight fibers with high thermal conductivity and high electric conductivity for the simulation of thermal and electric properties respectively. The numerical examples are compared with experimental data published in literature. The numerical tests clearly demonstrate the potential of the FM-BEM for large scale simulation of CNT composites.

### Introduction

In recent years, the fast multipole boundary element method (FM-BEM) has attracted the interest of many researchers. It is proved that FM-BEM can solve some very large scale problems, which are difficult to solve by FEM and other methods. One of the urgent affairs is to find such practical problems in engineering and sciences. In the same time, CNT composites have attracted considerable interest in various industrial applications because of their unusual physical properties of the carbon nanotubes, e.g., unusually high elastic modulus, thermal and electric conductivity. The simulation of CNT composites is perhaps one of the valuable practical applications of FM-BEM.

Based on the previous investigation on large scale simulation of particle- and fiber-reinforced composite materials using FM-BEM [1-3], the carbon nanotubes are treated as effective elastic fibers for the simulation of elastic property, and treated as straight fibers with high thermal conductivity and high electric conductivity for the simulation of thermal and electric properties respectively. To enhance the efficiency, the repeated identical sub-domain approach is applied, and for large scale simulation the parallel FM-BEM computation is performed.

Some typical numerical examples are given to verify the applicability of the presented approach. The numerical results of effective properties obtained are compared with the corresponding numerical and experimental data published in literature [4-8].

### BEM with repeated identical sub-domain approach for simulating elastic property of CNT composites

For the RVE shown in Fig. 1, the boundary integral equations of the matrix and the  $k$ -th CNT fiber are expressed respectively as

$$C_{ij}(x)u_j(x) + \int_{S_0 + \sum S_k} T_{ij}^0(x, y)u_j(y)dS(y) = \int_{S_0 + \sum S_k} U_{ij}^0(x, y)t_j(y)dS(y) \quad (1)$$

$$C_{ij}(x)u_j(x) + \int_{S_k} T_{ij}^k(x, y)u_j(y)dS(y) = \int_{S_k} U_{ij}^k(x, y)t_j(y)dS(y) \quad (2)$$

where  $V_0$  is the sub-domain of the matrix,  $V_1, V_2, \dots, V_k, \dots, V_n$  are the sub-domains of CNTs,  $S_0$  is the outer boundary of the matrix, and  $S_k$  is the CNT-matrix interface of the  $k$ -th CNT. In addition,  $S_0^U$  and  $S_0^T$  are outer boundary parts of the matrix with given displacement and given traction, respectively. CNTs

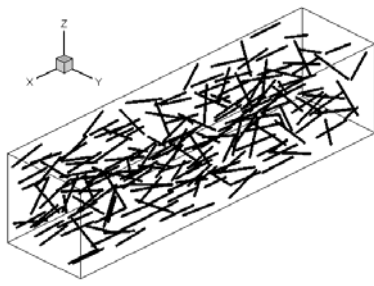


Fig. 1 RVE containing 200 randomly oriented CNTs

are randomly placed in the cuboid matrix, without connection between each two CNTs and without intersection with the surface of the matrix.

After discretization, Eqs. (1) and (2) can be written into matrix forms as follows,

$$\begin{bmatrix} A_{11}^0 & A_{12}^0 & A_{13}^0 & \cdots & A_{13}^k & \cdots & A_{13}^n \\ A_{21}^0 & A_{22}^0 & A_{23}^0 & \cdots & A_{23}^k & \cdots & A_{23}^n \\ A_{31}^0 & A_{32}^0 & A_{33}^0 & \cdots & A_{33}^k & \cdots & A_{33}^n \\ \vdots & \vdots & \vdots & \ddots & \vdots & \ddots & \vdots \\ A_{31}^k & A_{32}^k & A_{33}^k & \cdots & A_{33}^{k1} & \cdots & A_{33}^{kn} \\ \vdots & \vdots & \vdots & \ddots & \vdots & \ddots & \vdots \\ A_{31}^n & A_{32}^n & A_{33}^n & \cdots & A_{33}^{n1} & \cdots & A_{33}^{nn} \end{bmatrix} \begin{Bmatrix} U_0 \\ T_0 \\ U_1^0 \\ \vdots \\ U_k^0 \\ \vdots \\ U_n^0 \end{Bmatrix} - \begin{bmatrix} B_{13}^1 & \cdots & B_{13}^k & \cdots & B_{13}^n \\ B_{23}^1 & \cdots & B_{23}^k & \cdots & B_{23}^n \\ B_{33}^{11} & \cdots & B_{33}^{1k} & \cdots & B_{33}^{1n} \\ \vdots & \vdots & \vdots & \ddots & \vdots \\ B_{33}^{k1} & \cdots & B_{33}^{kk} & \cdots & B_{33}^{kn} \\ \vdots & \vdots & \vdots & \ddots & \vdots \\ B_{33}^{n1} & \cdots & B_{33}^{nk} & \cdots & B_{33}^{nn} \end{bmatrix} \begin{Bmatrix} T_1^0 \\ \vdots \\ T_k^0 \\ \vdots \\ T_n^0 \end{Bmatrix} = \begin{bmatrix} B_{11}^0 & B_{12}^0 \\ B_{21}^0 & B_{22}^0 \\ B_{31}^1 & B_{32}^1 \\ \vdots & \vdots \\ B_{31}^k & B_{32}^k \\ \vdots & \vdots \\ B_{31}^n & B_{32}^n \end{bmatrix} \begin{Bmatrix} \bar{T}_0 \\ \bar{U}_0 \end{Bmatrix} \quad (3)$$

$$H^k U_k^k = G^k T_k^k \quad (4)$$

where  $U_0$  and  $\bar{T}_0$  stand for the unknown nodal displacements and given nodal tractions on  $S_0^T$ , respectively,  $T_0$  and  $\bar{U}_0$  the unknown nodal tractions and given nodal displacements on  $S_0^U$ , respectively,  $U_k^0$  and  $U_k^k$  stand for the unknown nodal displacements on  $S_k$  for the matrix and the  $k$ -th CNT fiber, respectively.  $T_k^0$  and  $T_k^k$  the unknown nodal tractions on  $S_k$  for the matrix and the  $k$ -th CNT fiber, respectively. Sub-matrices  $A$ ,  $B$  in Eq. (3) consist of entries for the matrix material sub-domain,  $H^k, G^k$  in Eq. (4) for the  $k$ -th CNT material sub-domain.

Introducing the CNT-matrix interface conditions, the interface tractions can be computed by interface displacements using incidence matrix  $D^k$  and transform matrix  $M^k$  between the local and global coordinates of the interface boundary,

$$T_k^0 = -M^k D^k (M^k)^{-1} U_k^0 \quad (5)$$

where the incidence matrix  $D^k$  presents the relation between the interface tractions and displacements of  $k$ th CNT fiber in the local coordinate system, and it needs to be calculated only once for all the identical fibers. Based on Eqs. (3) and (5), all boundary node values of the unknown variables can be solved using FM-BEM.

The CNT composites can be simplified as transversely isotropic material. The average direction of CNT fibers is taken as  $x_1$ , which is also the direction of longer side of the RVE, and the RVE is stretched along this direction under uniform traction. The equivalent homogenized strains and stresses can be defined as:

$$\bar{\varepsilon}_{ij} = \frac{1}{V} \int_V \varepsilon_{ij} dV = \frac{1}{2V} \int_{S_0} (u_i n_j + u_j n_i) dS \quad \bar{\sigma}_{ij} = \frac{1}{V} \int_V \sigma_{ij} dV = \frac{1}{V} \int_{S_0} \sigma_{ik} x_j n_k dS \quad (6)$$

where  $V, S_0$  are the volume and the surface of the RVE respectively. For the case of computation, it is taken that  $\bar{\varepsilon}_{22} = \bar{\varepsilon}_{33} = 0$ ; therefore the most interested Young's modulus can be identified as

$$\bar{E}_{11} = \bar{\sigma}_{11} / \bar{\varepsilon}_{11} \quad (7)$$

### BEM for simulating thermal and electric properties of CNT composites

Instead of Eqs. (1) and (2), the boundary integral equations for steady heat and electric conduction are expressed for the matrix and the  $k$ -th CNT fiber, respectively,

$$C(x)t(x) + \int_{S_0 + \sum S_k} F^0(x, y)t(y)dS(y) = \int_{S_0 + \sum S_k} T^0(x, y)f(y)dS(y) \quad (8)$$

$$C(x)t(x) + \int_{S_k} F^k(x, y)t(y)dS(y) = \int_{S_k} T^k(x, y)f(y)dS(y) \quad (9)$$

where  $t$  denotes the boundary temperature or electric potential,  $f$  denotes the normal heat flux or normal electric current, respectively for heat or electric conduction problem,  $T(x, y)$  and  $F(x, y)$  are the fundamental solutions of potential problem.

Based on the FM-BEM for simulating elastic property of CNT composites, the simulation of their thermal and electric properties can be performed correspondingly.

### Numerical results and discussions

**Simulation of elastic property.** The effect of the CNT volume fractions on the effective elastic modulus of the CNT composites for aligned oriented case has been investigated. The results obtained have been compared with the numerical results in Ref. [4] and other reported data in Ref. [5], which are obtained based on MD combined with an equivalent-continuum model.

The length of the CNT fibers is fixed at 50nm, and the radius of the CNT is 0.7nm. The volume of the CNT is considered to be 37% of the effective fiber volume. For the matrix material, the NASA LaRC-SI polymer (mentioned in Refs. [4, 5]) is used, with a Young's modulus of 3.8GPa and Poisson's ratio of 0.4. All the above parameters are adopted from Ref. [4] for the comparison. The Poisson's ratio of CNT is taken as 0.4, and the Young's modulus of CNT is 380GPa, which is 100 times of the matrix modulus. The matrix is formed as the method mentioned above according to the number and the actual volume of CNT. For saving the computational resource, up to 200 CNTs are considered. The global model of this example is shown in Fig. 2.

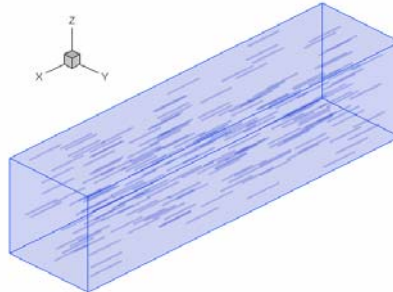


Fig. 2 A RVE containing 200 aligned CNTs

The estimated effective longitudinal Young's moduli of the CNT composites versus the CNT volume fractions are shown in Fig. 3 (left) in comparison with the data in Ref. [5] (Fig. 7 in that reference with CNT length of 50 nm) and Ref. [4]. The satisfied agreement could be observed.

The difference between the results obtained and those by Liu [4] may be caused by the following factors: First, in Liu's work, CNT is considered as rigid-inclusion, but elastic in our model; second, the RVE in Liu's work is embedded in the infinite domain of matrix material, and what they solved is an exterior problem. In this work the model with symmetrical boundary conditions is applied, and this is more realistic but has to spend more computational resources. In addition the difference of loading mode will also bring slight difference to the results. Finally, the largest model of Liu's contains 16000 CNT rigid fibers, and the computation run on a super computer, but the above mentioned model contains only 200 CNT fibers and run on a PC cluster.

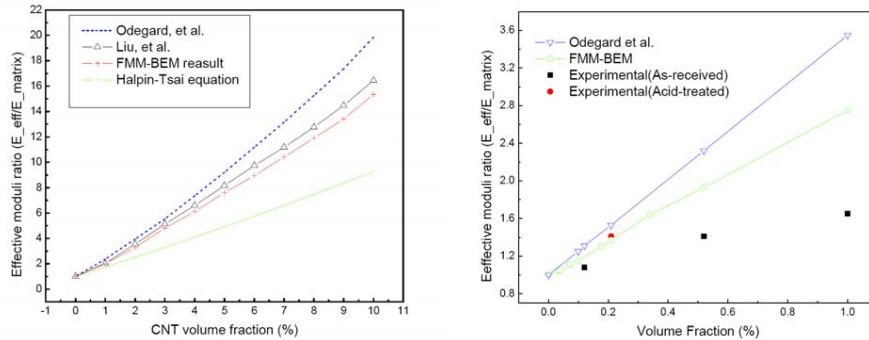


Fig. 3 Young's modulus of CNT reinforced LaRC-CP2 composite vs. CNT volume fraction

The comparison with corresponding experimental data for the composites prepared with both the as-received and acid-treated CNTs is shown in Fig. 3 (right). The properties of the composites with randomly oriented CNTs have been calculated for the aspect ratio of 60, using FM-BEM.

Although good agreement between the numerical results and the experimental data for acid-treated CNT composites has been observed, the predicted values of modulus are larger than the measured values for the as-received material, especially for values of CNT volume fraction greater than about 0.5%. The difference between the experiments and the model is most likely caused by the following factors: First, the model assumes that the effective fibers are perfectly dispersed in the polymer matrix, but a significant amount of CNTs may remain in bundles in the composite material. Second, the ideal interfacial condition is considered in the model, the stiffness may be decreased by the transfer layer between CNT and matrix. In addition, the CNT is considered as isotropic elastic fiber, but CNT is more close to being transversely isotropic material. Furthermore, the long CNTs will not all remain straight in the matrix. The closer agreement between the model and the acid-treated values indicates that the CNT are more dispersed in the acid-treated material than in the as-received material.

All these computations are run on a PC cluster THPCC in Tsinghua National Laboratory for Information Science and Technology, with 1.3GHz and 4GB memories per CPU. The example of largest scale has a total DOF of 1,589,148, costs about 7.6h using 12 CPUs.

**Simulation of thermal and electric properties.** Considering the limitation of computational resource on one PC, a RVE containing up to 300 CNTs is adopted. One global model of examples is shown in Fig. 4, with fiber aspect ratio and volume fraction equal to 20.0 and 0.15%, respectively. There are 640 triangular constant elements for one CNT in the mesh, which yields 640 DOF per CNT fiber. This mesh was found to be sufficient for obtaining converged results for the estimated effective conductivity.

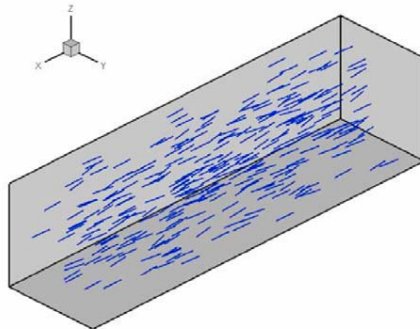


Fig. 4 A RVE containing 300 aligned CNTs

Fig. 5 is an overall plot of four cases studied in this paper: the directions of CNTs are aligned or randomly oriented, the aspect ratios of CNTs equals 50 or 20. In all these cases, the effective thermal conductivity increases significantly when the volume fractions increase, with the fastest increase in the case that CNTs are aligned oriented and the aspect ratio is taken as 50. The plot shows that an enlargement of aspect ratio can obtain a significant thermal conductivity enhancement and aligned orientation of CNTs is also propitious for thermal conductivity enhancements.

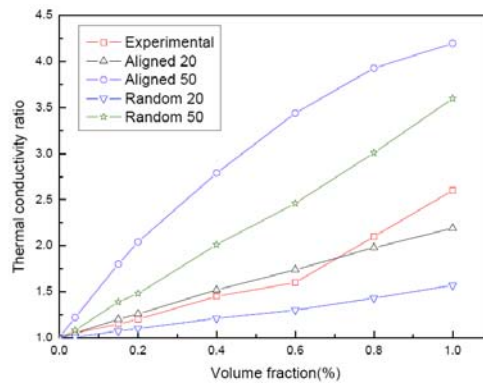


Fig. 5 Overall result view of thermal conductivities estimation in comparison with experimental data

The difference between the experiments data [6] and the numerical results obtained is most likely caused by the following factors: On the one hand, the thermal contact between the CNTs has not been considered in the computation, which will increase the thermal conductivity; on the other hand, in practical case the thermal contact condition of CNT-matrix interfaces should be imperfect rather than ideal condition considered in the numerical model adopted in this investigation, which will decrease the conductivity.

For the numerical estimation of electric property, it is shown from Fig. 6 that, there is a maximum of approximately 400% increase in the effective electric conductivity of aligned CNT composites with CNT aspect ratio of 50.0 in the range of CNT volume fraction up to 1.0%. Increase of CNT aspect ratio results in an increase of effective electric conductivity. In addition, randomly oriented CNTs result in a decrease of effective electric conductivity.

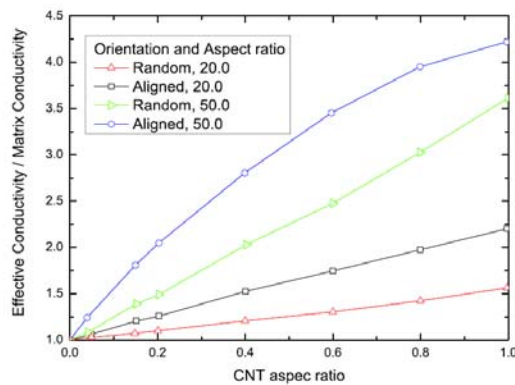


Fig. 6 Predicted effective conductivity of CNT-reinforced Composites

While for experimental results [7, 8] shown in Fig. 7, it is observed that significant changes occur in a small scope of CNT concentration. The effective electric conductivity reaches to a value several orders higher than that of matrix with a very small CNT volume/weight fraction. The difference between the

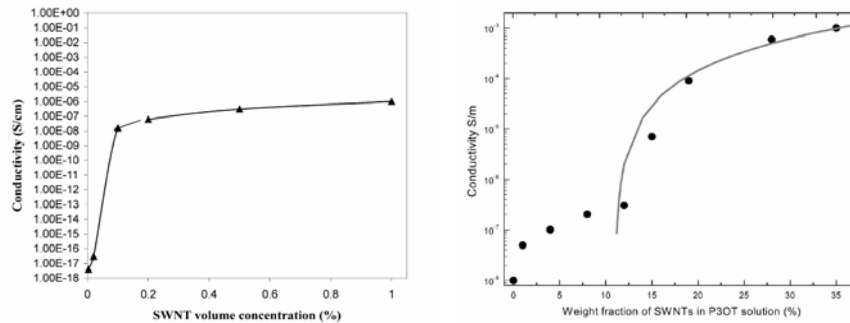


Fig. 7 Experimental data published in Ref [7] (left) and [8] (right)

experiments and the model is mostly caused by the following factors: while the model assumes that CNTs are well separated from each other and will not cross the surface of matrix sub-domain, in practice a significant amount of CNTs remain in bundles in the matrix, contact each other or cross the boundary of matrix sub-domain, which greatly enhance the effective electric conductivity. The phenomena observed in real CNT composites should be reflected in further developed models.

#### Concluding remarks

The numerical tests clearly demonstrate potential of the FM BEM for large scale solutions of CNT composites. Using this method, the effective elastic, thermal and electric properties can be simulated, but the difference between the numerical and experimental results have been observed. That means the numerical models have to be improved to consider more practical micro-structural factors, including the imperfect CNT-matrix interface conditions and thermal and electric contact between CNTs. Based on the present work, future investigations will be carried out in the development of new models.

**Acknowledgements** Financial supports for the project from the National Natural Science Foundation of China, under grant No. 10472051, and for a project from Schlumberger Technologies (Beijing) Ltd., are gratefully acknowledged.

#### References

- [1] H.T. Wang, Z.H. Yao. *Acta Mechanica Sinica*, **20**: 613-622 (2004)
- [2] H.T. Wang, Z.H. Yao. *Computer Modeling in Engineering & Sciences*, **7**: 85-96 (2005)
- [3] T. Lei, Z.H. Yao, H.T. Wang et al. *Acta Mechanica Sinica*, **22**: 225-232 (2006)
- [3] Y. J. Liu, N. Nishimura, Y. Otani. *Journal of Applied Mechanics*, **72**: 115-128 (2005)
- [4] G.M. Odegard, T.S. Gates, K.E. Wise et al. *Composite Science and Technology*, **63**: 1671-1687 (2003)
- [5] S.U.S. Choi, Z.G. Zhang et al. *Applied Physics Letters*, **79**: 2252-2254 (2001)
- [7] Z. Ounaies, C. Parkb, K.E. Wiseb et al. *Composites Science and Technology*, **63**: 1637-1646 (2003)
- [8] E. Kymakis, I. Alexandou, G.A.J. Amaratunga. *Synthetic Metals*. **127**: 59-62 (2002)

## Shape Optimization for Sound Scattering Problems Using a BE-Based Level Set Method

Kazuhisa Abe<sup>1</sup>, Shunsuke Kazama<sup>2</sup> and Kazuhiro Koro<sup>3</sup>

<sup>1</sup> Department of Civil Engineering and Architecture, Niigata University  
8050 Igarashi 2-Nocho, Niigata 950-2181, JAPAN, abe@eng.niigata-u.ac.jp

<sup>2</sup> Graduate School of Science and Technology, Niigata University  
8050 Igarashi 2-Nocho, Niigata 950-2181, JAPAN

<sup>3</sup> Department of Civil Engineering and Architecture, Niigata University  
8050 Igarashi 2-Nocho, Niigata 950-2181, JAPAN

**Keywords:** BEM, Shape optimization, Level set method, Sound insulation

**Abstract:** A shape optimization method is developed for sound scattering problems. In order to realize complicated shapes, each boundary element junction is used as the design variables which describe the boundary contour of body. Moreover, to allow the occurrence of topological change such as fusion and fission of boundaries during the optimization process, the shape is updated based on the level set method. Through numerical examples, the feasibility of the method is validated.

### Introduction

The urban area is harassed by noise of various kinds such as industrial and traffic noises. Hence the sound or noise reduction is a very important issue. Tanaka *et al.*[1] developed a shape optimization method for the sound-insulating wall using the cellular automata, and found that the optimal shape can be a very complicated one. Even by their method, however, the layout is to be searched within the finite number of cells.

The authors[2] have developed a BE-based topology optimization approach using the level set method. Since in the method co-ordinates of element junctions are used as the design variables, any shape and topology can be realized. Therefore, it can be expected that the method will serve to find complex shapes for sound scattering bodies.

In this study the optimization method developed in [2] is applied to the shape optimization of sound insulating structures. Since in the acoustic scattering problem holes in a body do not affect the result, the consideration of topological change will not be essential. However, the fusion or fission of sub-boundaries may occur during the shape optimization process. Therefore it will be desirable to cope with the topological change, especially for a sound scattering body because of its complex boundary contour. The developed method is applied to numerical examples, and the validity of the method is discussed.

### Design Sensitivity Analysis with Boundary Element Method

**Boundary Element Equation for Sound Scattering Problems.** Let us consider a two-dimensional sound scattering field as illustrated in Fig.1. A scattering body is embedded in a half-plane. One source point and a few observation points are allocated at opposite side of the obstacle to each other. The boundary integral equation is given by

$$c(\mathbf{x})p(\mathbf{x}) + \int_{\Gamma} p(\mathbf{y}) \frac{\partial p^*}{\partial n_y} d\Gamma_y = p^*(\mathbf{x}, \mathbf{x}_0), \quad (\mathbf{x} \text{ on } \Gamma), \quad (1)$$

where  $p$  is the sound pressure,  $p^*$  is the fundamental solution for a half-plane,  $\mathbf{x}_0$  is the location of point noise,  $c$  is the free term,  $\Gamma$  is the boundary of the body, and  $n_y$  stands for the outward normal. Note that the Neumann condition is imposed on the boundary. Since in this study the Green's function of Helmholtz equation in a half-plane is used for the boundary integral equation, the element discretization is needed only on the scattering body.

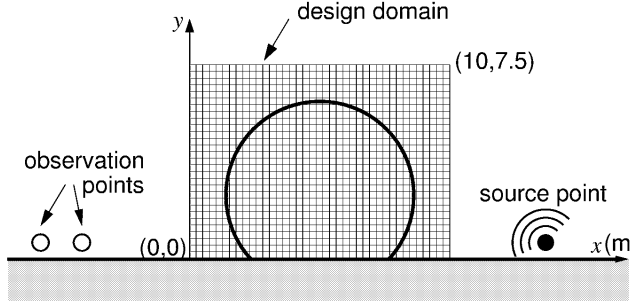


Fig.1 Sound scattering problem.

From eq(1) the boundary element equation is expressed by

$$[\hat{\mathbf{H}}]\{\mathbf{P}\} = \{\hat{\mathbf{P}}^*\}, \quad (2)$$

where  $[\hat{\mathbf{H}}]$  is the coefficient matrix,  $\{\mathbf{P}\}$  is a vector of nodal pressure and  $\{\hat{\mathbf{P}}^*\}$  is a vector given by the point noise.

In order to avoid the fictitious eigenfrequencies, besides eq(2), the identity condition at external points locating inside the body is employed[1], i.e.,

$$0 = - \int_{\Gamma} p(y) \frac{\partial p^*}{\partial n_y} d\Gamma_y + p^*(\mathbf{x}, \mathbf{x}_0), \quad (3)$$

where  $\mathbf{x}$  is an observation point. The discretization of eq(3) results in

$$[\bar{\mathbf{H}}]\{\mathbf{P}\} = \{\bar{\mathbf{P}}^*\}, \quad (4)$$

where  $[\bar{\mathbf{H}}]$  is a matrix associated with the integral representation, and  $\{\bar{\mathbf{P}}^*\}$  is a vector of pressure evaluated at the external points for the noise source.

Combining eqs(2) and (4), we obtain the solving equation by virtue of the least square method,

$$[\mathbf{H}]^T \{\mathbf{HP} - \mathbf{P}^*\} = 0, \quad [\mathbf{H}]^T = \begin{bmatrix} \hat{\mathbf{H}} \\ \bar{\mathbf{H}} \end{bmatrix}, \quad \{\mathbf{P}^*\} = \begin{Bmatrix} \hat{\mathbf{P}}^* \\ \bar{\mathbf{P}}^* \end{Bmatrix}. \quad (5)$$

**Design Sensitivity Analysis.** The shape optimization problem for sound scattering bodies is defined by

$$\begin{aligned} \min_{\mathbf{X}_b} J(\mathbf{P}; \mathbf{X}_b) &:= F(\mathbf{P}; \mathbf{X}_b) + [\boldsymbol{\lambda}]^T [\mathbf{H}]^T \{\mathbf{HP} - \mathbf{P}^*\} + \lambda_+(V - V_{max}), \\ \text{subject to} \quad &[\boldsymbol{\lambda}]^T [\mathbf{H}] \{\mathbf{HP} - \mathbf{P}^*\} = 0 \quad \text{for } \forall \{\boldsymbol{\lambda}\}, \\ &\lambda_+(V - V_{max}) = 0, \quad \lambda_+ \geq 0, \end{aligned} \quad (6)$$

where  $J$  is the objective function,  $F$  is a cost function estimating the sound pressure. The second term of the right-hand side stands for the condition associated with the boundary element equation, and  $\{\boldsymbol{\lambda}\}$  is a vector of Lagrange multiplier. The third term is the volume restriction.  $V$  is the volume of scattering body,  $V_{max}$  is an allowable limit and  $\lambda_+$  is a Lagrange multiplier. In eq(6) the co-ordinates of element junctions  $\{\mathbf{X}_b\}$  are used as the design variables.

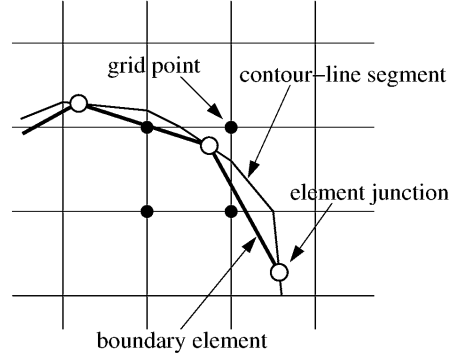


Fig.2 Boundary element discretization with level set function.

The variation of  $J$  due to the geometrical change  $\{\Delta \mathbf{X}_b\}$  is given by

$$\begin{aligned} \Delta J = & \left[ \frac{\partial F}{\partial \mathbf{P}} \right]^T \{\Delta \mathbf{P}\} + \left[ \frac{\partial F}{\partial \mathbf{X}_b} \right]^T \{\Delta \mathbf{X}_b\} + [\lambda]^T \left[ \frac{\partial \mathbf{H}^T}{\partial \mathbf{X}_b} \cdot \Delta \mathbf{X}_b \right] \{\mathbf{H}\mathbf{P} - \mathbf{P}^*\} \\ & + [\lambda]^T [\mathbf{H}]^T \left\{ \left[ \frac{\partial \mathbf{H}}{\partial \mathbf{X}_b} \cdot \Delta \mathbf{X}_b \right] \{\mathbf{P}\} + [\mathbf{H}] \{\Delta \mathbf{P}\} - \left\{ \frac{\partial \mathbf{P}^*}{\partial \mathbf{X}_b} \cdot \Delta \mathbf{X}_b \right\} \right\} \\ & + \lambda_+ \left[ \frac{\partial V}{\partial \mathbf{X}_b} \right]^T \{\Delta \mathbf{X}_b\}, \end{aligned} \quad (7)$$

where  $\{\Delta \mathbf{P}\}$  is the change of pressure resulted from the shape change  $\{\Delta \mathbf{X}_b\}$ .

As mentioned above, in this study every element junction is used to describe the boundary shape. Therefore the number of design variables is comparable to the degrees of freedom in the boundary element equation. In order to reduce the computational cost, an adjoint equation is introduced, i.e.,

$$[\mathbf{H}^T \mathbf{H}] \{\lambda\} = - \left\{ \frac{\partial F}{\partial \mathbf{P}} \right\}. \quad (8)$$

Since at this stage the boundary element equation (5) has already been solved,  $\{\lambda\}$  satisfying eq(8) can be obtained economically in conjunction with the LU factorization method. Substituting the solution  $\{\lambda\}$  of eq(8) into eq(7), we can obtain the following expression

$$\Delta J = [Re(\beta) + \lambda_+ \frac{\partial V}{\partial \mathbf{X}_b}]^T \{\Delta \mathbf{X}_b\}, \quad (9)$$

where  $\{\beta\}$  is a vector given by

$$\{\beta\} = \left\{ \frac{\partial F}{\partial \mathbf{X}_b} \right\} + [\lambda]^T \left[ \frac{\partial \mathbf{H}^T}{\partial \mathbf{X}_b} \{\mathbf{H}\mathbf{P} - \mathbf{P}^*\} + \mathbf{H}^T \left\{ \frac{\partial \mathbf{H}}{\partial \mathbf{X}_b} \mathbf{P} - \frac{\partial \mathbf{P}^*}{\partial \mathbf{X}_b} \right\} \right]. \quad (10)$$

The velocity which leads to an optimal shape is given by

$$\{\mathbf{V}\} = - \left\{ Re(\beta) + \lambda_+ \frac{\partial V}{\partial \mathbf{X}_b} \right\}. \quad (11)$$

In this paper the nodal velocity  $\{\mathbf{V}\}$  is directed to the outward normal at each boundary element junction.

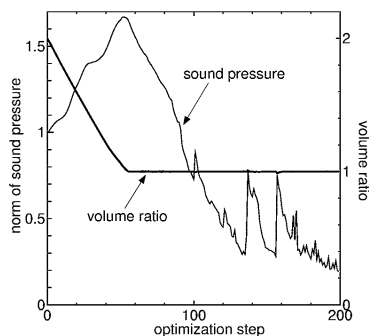


Fig.3 Time histories of cost function and volume ratio; element length=0.5m,  $V_{max} = 0.5V_0$ .

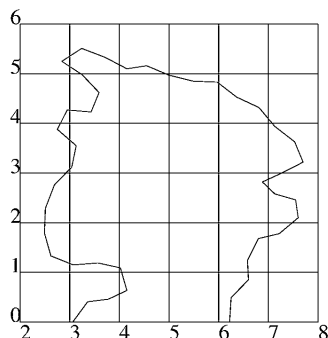


Fig.4 Optimal shape at the 200th step; element length=0.5m,  $V_{max} = 0.5V_0$ .

Once the volume  $V$  reaches the allowable limit, it should be kept at  $V_{max}$ . The Lagrange multiplier  $\lambda_+$  which meets this condition is given by

$$\lambda_+ = -\frac{\left[\frac{\partial V}{\partial \mathbf{X}_b}\right]^T \{Re(\beta)\}}{\left[\frac{\partial V}{\partial \mathbf{X}_b}\right]^T \left\{\frac{\partial V}{\partial \mathbf{X}_b}\right\}}. \quad (12)$$

### Shape Updating Process with Level Set Method

**Development of Boundary Element Discretization.** In general, the BE-based shape optimization is achieved within the framework of the Lagrange description[3]. In this paper, however, to cope with the topological change which may occur during the shape optimization process, the shape is updated based on the Eulerian frame. The topological change is captured with the aid of the level set method[4]. The authors[2] have developed a BE-based topology optimization using the level set method. In this section the outline of the method is described.

In order to define the level set function, a grid is introduced into a design domain as shown in Fig.1. The level set function is assigned at each fixed grid point(Fig.2). The boundary is implicitly defined by the zero contour of the level set function. Once the contour line is drawn on the background grid, the element junctions are equidistantly distributed along the contour. The boundary element discretization is then achieved by connecting the element junctions with each other.

**Shape Updating Process.** Since the level set function is used to represent the zero level set, it is sufficient to assign the nodal values only in the neighborhood of the contour. These nodal values are given by a signed distance function from the contour.

The change of the shape and topology arises from the advection of the level set function governed by the Hamilton-Jacobi equation

$$\frac{\partial \psi}{\partial t} = -\mathbf{v} \cdot \nabla \psi, \quad (13)$$

where  $\psi$  is the level set function,  $\mathbf{v}$  denotes a convective velocity.

In order to update  $\psi$ , the velocity field should be assigned to the grid points locating near the boundary. However, the velocity obtained from eq(11) is distributed only on the boundary. The velocity at each grid point is produced by the projection of normal velocity of its nearest contour segment.

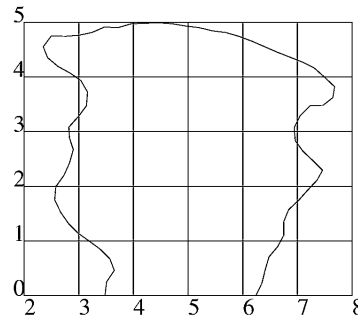
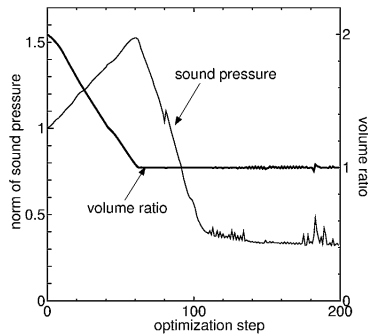


Fig.5 Time histories of cost function and volume ratio; element length=0.25m,  $V_{max} = 0.5V_0$ .

Fig.6 Optimal shape at the 200th step; element length=0.25m,  $V_{max} = 0.5V_0$ .

Since the level set function  $\psi$  is defined by a distance function,  $|\nabla\psi|=1$  holds for eq(13). Consequently, the level set function at the  $n + 1$ th step can be updated by

$$\psi_i^{n+1} = \psi_i^n + v_{Gi}\Delta t, \tag{14}$$

where  $\psi_i^{n+1}$  and  $v_{Gi}$  are the level set function and the velocity at the  $i$ th grid point, respectively.  $\Delta t$  is time increment, and is determined adaptively at each time step so that the numerical stability can be assured.

**Numerical Examples**

**Analytical Conditions.** The developed method is applied to a two-dimensional sound scattering problem shown in Fig.1. A unit source is located at (15, 0.5). The sound pressure is measured at two points of (-5, 0.5) and (-10, 0.5). The rectangular region of  $[0 \leq x \leq 10] \times [0 \leq y \leq 7.5]$  is set as the design domain. The background grid with the size of 0.25m is embedded in the design domain. The initial shape of the scattering body is given by a circular form as shown in the figure. The sound pressure is estimated by a norm defined as

$$F := \sum_i^n |P_i|, \tag{15}$$

where  $n$  is the number of observation points and  $P_i$  is the pressure at the  $i$ th point.

**Numerical Results.** A numerical result for the frequency of 100Hz is shown in Fig.3. Here the boundary of sound-insulating body is discretized by piece-wise constant elements of about 0.5m length.  $V_{max}$  is set to  $0.5V_0$ , where  $V_0$  is the initial volume. In the figure the norm of sound pressure is normalized as  $F/F_0$ , where  $F_0$  is the pressure norm for the initial shape. From the figure we can see that the volume converges quickly. The sound pressure begins to decrease after the convergence of volume. Fig.4 shows the shape at the 200th step. It is found that the optimal shape has an intricate contour. While the branch locating at the top-left corner grows with progress of optimization step, cutting of the branch may happen when it becomes thinner than the mesh size due to the limit of resolution. The fluctuations of pressure in Fig.3 are caused by this breakage. Despite of this topological change, the present method attains the pressure reduction effectively.

Figs.5 and 6 are showing the result for the element size of about 0.25m. The same analytical conditions with the prior example are used except the element size. From Fig.5 it can be seen that the mesh refinement avoids breaking branches.

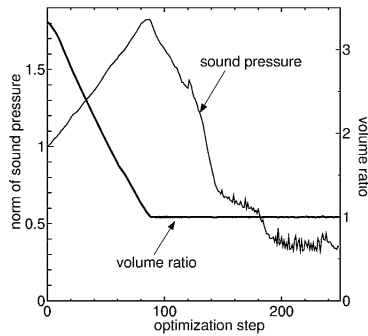


Fig.7 Time histories of cost function and volume ratio; element length=0.25m,  $V_{max} = 0.3V_0$ .

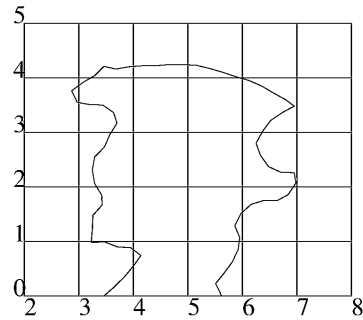


Fig.8 Optimal shape at the 250th step; element length=0.25m,  $V_{max} = 0.3V_0$ .

Figs.7 and 8 are showing the result for  $V_{max} = 0.3V_0$ . The boundary is discretized with the size of about 0.25m. Due to the reduction of volume limit, the height and width of the body become smaller than the case for  $V_{max} = 0.5V_0$ , while these optimal shapes are similar to each other. In general, frequencies of 500Hz or higher will be important in the noise pollution problems. Though in this paper results for frequencies higher than 100Hz are not shown, it was found that the optimal shape has less complexity with increasing frequency. It may be caused by the fact that the wave diffraction is reduced for higher frequencies. In this case the shape will be less important than the height of obstacle.

### Conclusions

In this paper a BE-based shape optimization method is developed for sound insulating structures. To cope with the topological change which may occur during the optimization process, the level set method is utilized. Although the developed method is applied to sound scattering problems with a rather low frequency, intricate shapes were obtained. Since, in the design process, the body shape is defined using every element junction, any shape is realizable.

### References

- [1] M.Tanaka, T.Matsumoto and Y.Arai *Trans. JASCOME, J. Bound. Elem. Meth.*, **19**, 69-74 (2002).
- [2] K.Abe, S.Kazama and K.Koro *Commun. Numer. Meth. Engng.*, (in press).
- [3] E.A.Divo, A.J.Kassab and M.S.Ingber *Eng. Anal. Bound. Elem.*, **27**, 695-703 (2003).
- [4] G.Allaire, F.Jouve and A-M.Toader *Compt. Rend. de l'Academie des Sci., I*, **334**, 1125-1130 (2002).

## Stress Analysis of Elastic Inclusions Functionally Graded Interface by 2D Field Boundary Element Method

E. Ruocco<sup>1</sup>, V. Minutolo<sup>2</sup>

<sup>1</sup> Dep. of Civil Engineering, Second University of Napoli, via Roma 9, 81031 Aversa, Ce, Italy, [eugenio.ruocco@unina2.it](mailto:eugenio.ruocco@unina2.it)

<sup>2</sup> Dep. of Civil Engineering, Second University of Napoli, via Roma 9, 81031 Aversa, Ce, Italy, [vincenzo.minutolo@unina2.it](mailto:vincenzo.minutolo@unina2.it)

**Keywords:** Functionally Graded Materials, FGM, Field Boundary Element Method, FBEM, Interface, Multiregion, Bimaterial

**Abstract.** The work concerns Functionally Graded Interface in bimaterial; the Field Boundary Element Method is used in order to deal with any possible variation of the components, the method require domain discretization on the graded interface only and pure boundary elements to model homogeneous regions. Since the graded region is a small part of the whole body, only few domain unknowns have to be considered with respect to the total number of variables describing the problem.

**Introduction.** Novel materials, like Functionally Graded Materials (FGM), are tailored to fulfil compound requirements by combining different materials into one. The main feature of FGM with respect to traditional composites is that component properties are combined to get intermediate behaviour between that of the constituents. When the FGM is used at the interface between two materials, it yields to continuous transition from one material to the other that reduces jump discontinuity of the response at the interface level usually present when layered bi-material is used [1-3].

Numerical analysis of FGM structure is founded on elasticity theory applied to heterogeneous materials, it consists of the solution of heterogeneous equations where the constitutive parameters are not constant within the domain that describes the structure. The mathematical formulation produces Partial Differential Equations with variable coefficients whose solution involves cumbersome calculations. This difficulty is encountered when one is aimed to calculate the Green function of the stated problem as well [4-7]. Only particular variation has been solved, namely isotropic material with scalar variation of the properties, such isotropic FGM can be described by a constant elasticity tensor multiplied by a scalar field, defined on the domain, that describes the variation of the material. More complicated description of variable material arise for anisotropic elasticity, when material symmetry directions governing the constitutive law can vary as well and multiple parameters equation are required to describe entirely the elasticity tensor.

The present work is aimed to apply Field Boundary Element Method to heterogeneous material, in the case of simple scalar variability, in order to model the graded bi-material interface. The formulation enriches multi region Boundary Element Method with the Field terms that allows to consider the material elasticity variation [8-10].

**Formulation.** In the paper we consider an elastic structure made of two different materials joined by a graded interface, the structure is described by three regions, the first made of constant material of one kind, the third region is made of constant material of a second kind, the interface between two material regions is made of continuously varying material ranging from the first to the second one.

Consider that the variable material constitutive law is of scalar type:

$$c_{ijk}^{[n]}(x) = \gamma^{[n]}(x) \bar{c}_{ijk}^{[n]} \quad (1)$$

where  $c_{ijk}^{[n]}(x)$  is the variable elastic tensor,  $\gamma^{[n]}(x)$  is the scalar field describing material variability and  $\bar{c}_{ijk}^{[n]}$  is the elastic tensor of a reference constant material.

The equation governing the FBEM is obtained by the application of the reciprocal Betti's theorem between the region with variable elasticity and the unbounded space of reference constant material.

The equation contains field variable and requires domain integration. Multi region formulation is applied in order to describe by means of ordinary pure Boundary Element Method the part of the structure where

elasticity does not vary; hence the domain description is required only on the heterogeneous part of the structure described by eq (1).

The resulting equation on the boundary of interface is

$$s_{hl}(y)\gamma(y)u_l(y) = \int_{\partial\Omega_1^{[n]}} G_{lh}(x,y)t_h(x) dS(x) - \int_{\partial\Omega_1^{[n]}} \gamma(x)F_{lh}(x,y)u_h(x) dS(x) + \int_{\Omega_1^{[n]}} T_{hjl}(x,y)u_h(x)\gamma_{,j}(x) dV(x) \quad (2)$$

The equation governing the equilibrium of homogeneous regions is:

$$s_{hl}(y)u_l(y) = \int_{\partial\Omega_1^{[n]}} G_{lh}(x,y)t_h(x) dS(x) - \int_{\partial\Omega_1^{[n]}} F_{lh}(x,y)u_h(x) dS(x) \quad (3)$$

Eq (2) and eq (3) have been derived assuming vanishing body forces; symbols  $G_{lh}$  and  $F_{lh}$  stand for displacement and traction of the fundamental solution for constant reference material and  $T_{hjl}$  for stress of the fundamental solution;  $x$  and  $y$  are field and source points respectively and  $s_{hl}$  is the free term of Cauchy Principal Value integration of singular kernel  $F_{lh}$  at the boundary.

Numerical transformation of eq (2) and (3) follows ordinary BEM and FBEM formulations; consider that rigid body technique has to be applied to calculate diagonal coefficients of the matrix that multiplies the unknown displacement  $u$ .

By applying the external and interface conditions and splitting the terms associated to boundary  $\partial\Omega_1^{[n]}$ , where displacements are known and  $\partial\Omega_2^{[n]}$  where the tractions are known, we can assemble eq (2) and eq (3), written for each sub-region, into a single system:

Finally, the matrix representation of the equations is

$$\begin{bmatrix} \hat{\mathbf{F}}_{\partial\Omega_2,j} & \hat{\mathbf{T}}_{\Omega} & \hat{\mathbf{G}}_{\partial\Omega_2,j} \\ \hat{\mathbf{F}}_{\partial\Omega_1} & \hat{\mathbf{G}}_{\partial\Omega_2} \end{bmatrix} \begin{bmatrix} \hat{\mathbf{u}}_{\partial\Omega_2,j} \\ \hat{\mathbf{u}}_{\Omega} \\ \hat{\mathbf{t}}_{\partial\Omega_2,j} \end{bmatrix} = \begin{bmatrix} \hat{\mathbf{F}}_{\partial\Omega_1} & \hat{\mathbf{G}}_{\partial\Omega_2} \end{bmatrix} \begin{bmatrix} \hat{\mathbf{u}}_{\partial\Omega_1} \\ \hat{\mathbf{t}}_{\partial\Omega_2} \end{bmatrix} \quad (4)$$

**Results.** In the present section, the solution of a square plate with circular inclusion is reported (Fig. 1); the ratio of Young modules of external and internal regions are:

$$\frac{E_{ext}}{E_{int}} = 5 \quad (5)$$

The plate is simply supported and subject to constant load  $\bar{q}$ . The interface between two regions is assumed to be graded, with Young modulus linearly variable. In Fig. a comparison between the proposed FBIE and FEM analysis is reported. It is known that for unbounded plate, the ratio between Young modulus of the external and internal materials and the response of the structure, in terms of maximum stress has the following asymptotic behaviour:

$$\text{no inclusion } \frac{E_{ext}}{E_{int}} \rightarrow 1 \Rightarrow \frac{\sigma_{max}}{\bar{q}} \rightarrow 1; \quad \text{void inclusion } \frac{E_{ext}}{E_{int}} \rightarrow \infty \Rightarrow \frac{\sigma_{max}}{\bar{q}} \rightarrow 3; \quad (6)$$

The results show that if the structure has graded interface the stress concentration reduces and its discontinuity vanishes. The gain in term of magnitude and in term of smoothness justify the use of graded material and the necessity of reliable modelling of its response [11].

**Conclusions.** A boundary element technique capable of defining the mechanical response of Multiregion Functional Graded Material via Field Boundary Element Method has been developed. The analytical function modeling the heterogeneity is general and fundamental solutions are not available in literature. Here, the elasto-static homogeneous solution is used as weight function. The procedure leads to a domain

integral on the heterogeneous region. The numerical results, obtained using the proposed method, indicate that it can provide accurate solutions in terms of stress and displacements. The results show that graded interfaces are able to cancel the jump discontinuity of the stress about the inclusion, moreover the presence of graded interface reduces the stress magnitude around the inclusion. The calculation performed by FBEM, due to the possibility of modelling continuous gradation, allows to evaluate with good agreement the actual distribution of stress near the inclusion giving important information about the design of graded interfaces in order to minimise the possibility that errors, caused by high stress localisation, occur during calculation and misunderstanding on interfacial stress arises due to jump approximation.

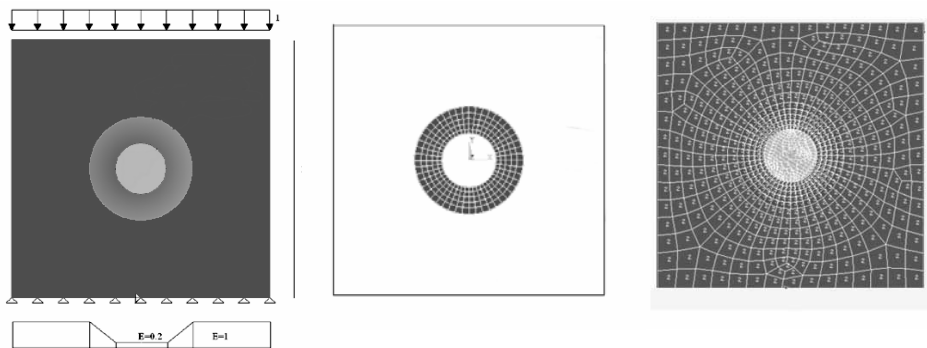


Fig. 1: Graded plate, Young modulus gradation, FBEM mesh, FEM mesh

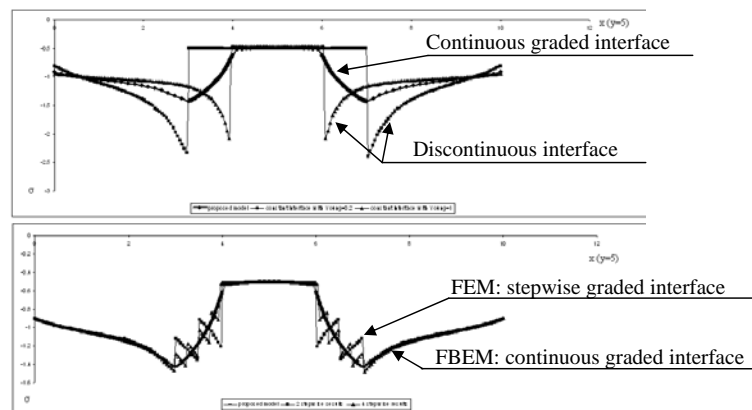


Fig. 2 Stress along the midline of inclusion

**References**

- [1]. Suresh S, Mortensen M. *Fundamentals of Functionally Graded Materials*. IOM Communications, London, (1998).
- [2]. Koizumi M. *Composites Part B*, **28B**, 1-4 (1998)
- [3]. Kim HK, Paulino GH. *Journal of Applied Mechanics*, **69**, 502-514 (2002).
- [4]. Praveen GN, Reddy JN. *International Journal of Solids and Structures* **35**, 4457-4476 (1998.)
- [5]. Xu SQ, Kamiya N.. *Engineering Analysis with Boundary Elements*, **23**, 391-397 (1999)
- [6]. Martin PA, Richardson JD, Gray LJ, Berger JR. *Proceedings of the Royal Society London*, **A458**, 1931-1947 (2002)
- [7]. Chan YS, Gray LJ, Kaplan T, Paulino GH. *Proceedings of the Royal Society London*, **A460**, 1689-1706 (2004)
- [8]. Mikhailov SE. *Engineering Analysis with Boundary Elements*, **26**: 681-690 (2002)
- [9]. Zhang X. *Engineering Analysis with Boundary Elements*, **28**: 997-1004 (2004)
- [10]. Minutolo V., Ruocco E. "Boundary element modelling and optimisation of structures made of functionally graded materials", in Selvadurai A.P.S., Tan C.L., Aliabadi M.H. Eds. *Advances in Boundary Element Techniques*, Montreal (2005.)
- [11]. Erdogan F, Wu BH, *Journal of Applied Mechanics*, **64**, 449-456 (1997)

## Parametric Analysis of SIF in FGM by Field Boundary Element Method

T. Colella<sup>1</sup>, V. Minutolo<sup>2</sup>

<sup>1</sup> Dep. of Civil Engineering, Second University of Napoli, via Roma 9, 81031 Aversa, Ce, Italy,  
tommaso.colella@unina2.it

<sup>2</sup> Dep. of Civil Engineering, Second University of Napoli, via Roma 9, 81031 Aversa, Ce, Italy,  
vincenzo.minutolo@unina2.it

**Keywords:** Functionally Graded Materials, FGM, Field Boundary Element Method, FBEM, Interface, Bimaterial, Stress intensity factor, SIF.

**Abstract.** In the paper the Field Boundary Element Method (FBEM) is applied to fracture analysis of Functionally Graded Material (FGM) and Mode I Stress Intensity Factor (SIF) is calculated. The material is considered to be transversely whose variation is described by a scalar function of the position that multiply a reference constant elastic modulus. Hence 2D plate made of a scalar heterogeneous isotropic material is considered. Parametric representation of structural response is presented depending on the variation of elastic properties of the plate.

**Introduction.** Functionally Graded Materials (FGM), are composite materials designed to satisfy multiphysics requests, by combining different materials into one, resulting in a continuous variable material. The main aspect of FGM with respect to traditional composites is that component properties are combined to get intermediate behaviour between that of the constituents. When the FGM is used at the interface between two materials, it yields to continuous transition from one to the other that cancels jump discontinuity of the response at the interface. Continuous transition greatly influences crack propagation and avoids or reduces debonding and slip of layers [1-4].

The present work is aimed to apply Field Boundary Element Method to heterogeneous material, in the case of simple scalar variability of properties, in order to model graded bi-material interface. The formulation enriches Boundary Element Method with the Field terms accounting for the material elasticity variation [5-8]. By means of the formulation, application of Elastic Fracture Mechanics (EFM) to calculate the Stress Intensity Factor under Mode I crack propagation is shown.

The calculation follows traditional formulation for EFM where it is supposed that around crack tip the elasticity of the material is constant within the small region of stress concentration.

**Formulation.** Elastic constitutive law of the material is governed by fourth order elastic tensor that, in Cartesian coordinate system, has the form:

$$\sigma_{ij}(x) = C_{ijhk}(x)\varepsilon_{hk}(x) \quad (1)$$

where  $\sigma_{ij}(x)$  is the Cauchy stress and  $\varepsilon_{hk} = (u_{h,k} + u_{k,h})/2$  is the infinitesimal strain. Constitutive tensor has the usual symmetries:

$$C_{ijhk}(x) = C_{hki j}(x) = C_{jihk}(x) = C_{ijhk}(x) \quad (2)$$

The structure, occupying the volume  $V$ , is subjected to body forces  $b_i(x)$ , traction  $p_i(x)$ , on the loaded boundary  $\partial V_f$ , and prescribed displacements on  $\partial V_u = \partial V / \partial V_f$ . Equilibrium equation of the structure, in term of displacement,  $u_i(x)$ , is:

$$(C_{ijhk}(x)u_{h,k}(x))_{,j} + b_i(x) = 0 \quad (3)$$

By means of weight residual application, using the Kelvin's solution  $u_{ii}^*$  as weight function, the following Field Boundary Integral Equation results [5, 6]:

$$\begin{aligned} J_{ii}(y)u_i(y) = & \int_V b_i(x)u_{ii}^*(x,y)dV + \int_{\partial V} t_i(x)u_{ii}^*(x,y)dS - \int_{\partial V} C_{ijhk}(x)\varepsilon_{ihk}^*(x,y)n_j(x)u_i(x)dS \\ & + \int_V C_{ijhk}(x)\varepsilon_{ihk,j}^*(x,y)u_i(x)dV + \int_V C_{ijhk,j}(x)\varepsilon_{ihk}^*(x,y)u_i(x)dV \end{aligned} \quad (4)$$

where  $J_{ii}(y)$  is a numerical coefficient depending on the boundary regularity at  $y$ .

Furthermore, eq (4) can be simplified by considering actual form of  $C_{ijk}^*(x)$  tensor. For scalar graded materials it depends on a function  $\gamma(x)$  and on a reference constant array  $C_{ijk}^0$ . Here we assume that Kelvin's solution material is described by the same tensor  $C_{ijk}^0$ , hence eq (4) becomes:

$$\begin{aligned} [J_{ii}(y) + \gamma(y)\delta_{ii}]u_i(y) &= \int_V b_i(x)u_i^*(x,y)dV + \int_{\partial V} t_i(x)u_i^*(x,y)dS - \int_{\partial V} \gamma(x)t_{ii}^*(x,y)u_i(x)dS \\ &+ \int_V \sigma_{ijk}^*(x,y)\gamma_{,j}(x)u_i(x)dV \end{aligned} \tag{5}$$

Numerical solution of eq (5) gives the displacement field of the structure, that is used to calculate the displacement at the crack tip. The proposed formulation has been applied to symmetrical plates where the crack has been modelled using single line, hence no dual equation is required neither hyper-singular integrals arise. The hyper-singular formulation of eq (5) should involve domain hyper-singular integrals and it will be the matter of further investigation. Alternative strategy for crack modelling would consist of multi region discretization that avoids hyper-singular integration as well.

The displacement at crack tip is extrapolated by means of radial expansion:

$$\frac{u_y(r)}{\sqrt{r}} = C_1 + C_2 r \tag{6}$$

where  $u_y(r)$  is the Mode I displacement and  $r$  is the distance from crack tip. Coefficients  $C_1$  and  $C_2$  have to be determined by minimising the difference between (6) and numerical solution given by (5). The numerical value of SIF is calculated assuming that, within a small neighbourhood of the crack tip, the elastic modulus of the material is  $E_t$  and can be assumed to be constant. By these considerations the SIF has the usual form [9-12]

$$K_I = \frac{\sqrt{2\pi}E_t}{4(1-\nu^2)} \lim_{r \rightarrow 0} \frac{u_y(r)}{\sqrt{r}} = \frac{\sqrt{2\pi}E_t}{4(1-\nu^2)} C_1 \tag{7}$$

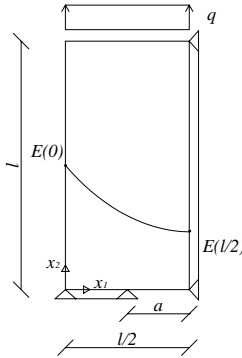


Figure 1: A quarter of the plate where solution is sought, geometry, load, and modulus variation

**Results.** The formulation has been applied to a rectangular plate, having length  $l$  and height  $h = 2l$ , with a crack at the centre and aligned to the short plate side. The crack length is  $2a$  and the elastic tensor vary accordingly to the following equation assuming scalar variation:

$$E = \gamma(x_1)E^0 \Leftrightarrow C_{ijk}^*(x) = \gamma(x_1)C_{ijk}^0 \tag{8}$$

where

$$\gamma(x_1) = \gamma(0) \exp\left[x_1 \ln\left(\gamma(l/2)/\gamma(0)\right)\right] \tag{9}$$

$E^0$  is the reference constant modulus and  $x_i$  is the horizontal coordinate defined in Fig. 1. In the example, only a quarter of the plate has been considered due to symmetry.

The numerical calculation has been performed assuming the following data value ranges:

$$\begin{aligned}
 E^0 &= 10^5, \nu = 0.3 \\
 2a/l &= 0.25, 0.5, 0.75 \\
 \gamma(l/2)/\gamma(0) &= 0.1; 0.3; 0.5; 0.7; 0.9
 \end{aligned}
 \tag{10}$$

The plate modulus is supposed to decrease from  $E^0 = E(0)$ , corresponding to the plate outer side, to  $E^1 = E(l/2)$  corresponding to the middle of the plate i.e. the centre of the crack.

$E^1/E^0$	$2a/l = 0.75$	$2a/l = 0.5$	$2a/l = 0.25$
0.10	4.84	2.23	0.75
0.30	6.42	3.11	1.34
0.50	6.99	3.54	1.68
0.70	7.34	3.84	1.92
0.90	7.37	4.06	2.12

Table 1: Stress Intensity Factors parametric analysis

In Table 1,  $K_I$  is listed as a function of  $a/l$  and  $E^1/E^0$ ; the results are also plotted in Figure 2, where the Stress Intensity Factor,  $K_I$ , is plotted versus the ratio between  $E^1/E^0$  for  $2a/l$  ranging within the values reported in eq (10). It can be seen that for increasing  $a/l$ , the SIF increases, and it increases at increasing  $E^1/E^0$  too. Conversely when  $E^1/E^0$  decreases, the crack tip stiffness decreases and so does the calculated SIF.

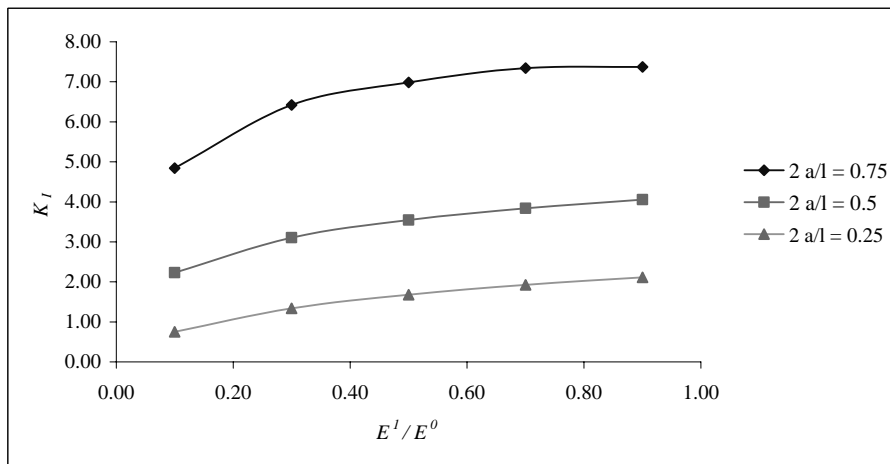


Figure 2 – Mode I Stress Intensity Factor,  $K_I$ , Vs Young modulus ratio for different crack length,  $a$ .

**Conclusions.** The numerical calculation shows the feasibility of the method that allows to apply Integral Equations to fracture mechanics even in the cases of heterogeneous materials; moreover it has been shown how the variability of the mechanical properties of the structure influences the SIF value. The here proposed procedure can be used to design composite structures where the variation of the constitutive parameters is prescribed to minimise the stress intensity around crack tip. The method could be used to evaluate the crack path propagation too, since it is very influenced by the material variability near the crack tip. It has to be considered that, although many authors suppose constant material behaviour around the crack tip, variability

influence can be investigated in detail by means of  $J$  integral formulation that can be accomplished by a slight modification of present FBEM. Finally, the formulation can be extended to anisotropic variable material, the application to anisotropic FGM will be the subject of further research activity.

#### References

- [1]. Ichikawa, K. (Ed) *Functionally graded materials in the 21st century*, Kluwer Academic Publishers: Norwell, Ma. (2001);
- [2]. Watanabe, K.; Ziegler, F. (Ed) *Dynamics of Advanced Materials and Smart Structures*, Proc. IUTAM Symposium 20-24 May 2002, Kluwer Academic Publishers: Dordrecht. (2003);
- [3]. Pan, W.; Gong, J.; Zhang, L.; Chen, L. (Ed) *Functionally Graded Materials VII*, Proc. VII int. Symposium (FGM2002), Beijing 15-18 October, 2002, Trans Tech Publication Ltd.: Enfield NH. (2003);
- [4]. Wang, B.L.; Tian, Z.H. *FE Analysis and Design*, **41** pp. 335-349 (2005).
- [5]. Minutolo V., Ruocco E. *Boundary element modelling and optimisation of structures made of functionally graded materials*, in Selvadurai A.P.S., Tan C.L., Aliabadi M.H. Eds. *Advances in Boundary Element Techniques*, Montreal (2005.)
- [6]. Minutolo, V.; Ruocco, E.; Colella, T. *CMES*, (submitted 2006).
- [7]. Sutradhar, A.; Paulino, G.H. *Computer Methods in Applied Mechanics and Engineering*, **193**, pp. 4511-4539 (2004).
- [8]. Kim, J.H.; Paulino, G.H. *Journal of Applied Mechanics*, **69**, pp. 502-511 (2002).
- [9]. Ravi Chandran K.S., Barsoum I. *International Journal of Fracture* **121**: 183-203, (2003)
- [10]. Kim, J.H.; Paulino, G.H. *International Journal of Numerical Methods in Engineering*, **53**, pp. 1903-1935 (2001)
- [11]. Sutradhar, A.; Paulino, G.H.; Gray, L.J. *International Journal of Numerical Methods in Engineering*, **62**, pp. 122-157, (2005).
- [12]. Zhang, CZ.; Sladek, J.; Sladek, V. *Computational Material Science*, **32** pp. 611-619, (2005).